A CHARACTERISATION OF LAVA TYPES AND A STORY OF PORE GROWTH AND COLLAPSE AT SANTIAGUITO VOLCANIC DOME COMPLEX, GUATEMALA.

Emma Rhodes

A thesis submitted in partial
fulfilment of the requirements for the
Degree of Master in Science in Geology
at the University of Canterbury

March 2014

Walking through the ash cloud from a partial dome and lava flow collapse, Nov 2012

ABSTRACT

Structures and textures of lava dome lavas reflect underlying magmatic and eruptive processes. The composition, temperature, degassing and outgassing histories of these lavas determine the eruption style and associated hazards. Santiaguito Lava Dome, Guatemala shows unique lava sequences that respond to repeated eruption cycles primarily controlled by changing effusion rates. Four domes have extruded sequentially along a linear trend since 1922. In this thesis I map and classify the lithologies and macro- and micro-scale lava textures at Santiaguito, and relate these to shallow conduit and post-eruptive processes. These observations are further constrained using the historical eruption record to determine temporal relationships and changes in effusion rates between flow units. Using this data I produce a conceptual model for the different lava types, eruption cycles and associated hazards at Santiaguito.

Four distinct lava morphologies are classified; "spines", "long blocky lava flows", "vesicular lava flows" and "summit blocky lava flows". These differ in both macro-scale lava features, and also in micro-scale porosity, permeability and pore textures. These textures indicate changing in-conduit and post-eruptive conditions. Spines are low volume and dense with deflated interconnected pores. Thinner vesicular zones periodically break up the dense zones with interconnected en-echelon sigmoidal pores. Spines occur at low effusion rates at the beginning and end of an eruption sequence, often initiating from a new vent at the start of a new sequence. Small gas explosions and near-continuous degassing accompany spine extrusion. Regular collapses generate small block and ash flows that reach the base of the dome, but spines have not been associated with larger block and ash flows at Santiaguito. Long blocky lava flows are high volume and have a wide porosity range. In general, more porous samples contain inflated interconnected pores which may be flattened or stretched, whereas denser samples contain deflated aligned tubular interconnected pores. Long blocky lava flows erupt at moderate to high effusion rates in the middle of eruption sequences. They are associated with associated with almost continuous degassing, small explosive eruptions and continuous small block and ash flows, as well as infrequent hazardous large block and ash flows. Vesicular lava flows are low volume and very porous with inflated interconnected pores. They are short-lived and erupt either at high effusion rates or when

the conduit is shorter at the start of an eruption sequence. They are sometimes extruded following removal of summit material by dome or flow collapses. Summit blocky lava flows extrude in combination with long blocky lava flows during periods of fast extrusion in both andesitic and dacitic magma. However they are the only lava type observed during intermediate extrusion rates of dactic magma, and during slow extrusion rates of andesitic magma. They are associated with almost continuous degassing, small explosive eruptions and continuous small block and ash flows.

Over its eruptive history, the dominant composition erupting from Santiaguito changed from dacite to andesite. However the microlite and phenocryst content of the magma does not vary by more than 5%. I interpret that spines form from higher viscosity dacitic magma at low effusion rates. Here, degassing, cooling and outgassing in the conduit prior to eruption increases the viscosity, while shear at the conduit edges generates vesicular cavitation bands, that easily fracture to form fault bounded spines. Long blocky lava flows and vesicular lava flows form from lower viscosity magmas. These are either andesites or dacites that erupt at higher effusion rates and so experience less degassing, outgassing and cooling prior to eruption. The high volume of the long lava flows allows the initially vesicular lava to retain heat and degass and outgass along discrete interconnected porous networks within the flows, while along-flow shear results in flattening and stretching of pore shapes down flow. Summit blocky lava flows are andesitic or dacitic and accompany long blocky lava flows at high extrusion rates as an overflow mechanism. Therefore they have the same properties as the longer lava flows, but do not flow as far due to their lower supply volume. At low extrusion rates, summit blocky lava flows are the only type of lava extruded if the magma is andesitic. This is due to the lower viscosity of the andesitic lava, and replaces the spine facies that is present for dacitic magmas at low extrusion rates.

Three distinct kinds of eruption cycles are identifiable; a new dome cycle, an old dome dacite cycle and an old dome andesite cycle. The new dome cycle is characterised by initial partly endogenous growth of a new dome where pre-existing outgassing pathways do not exist. The old dome andesite and dacite cycles initiate from domes where there are pre-existing degassing pathways and therefore begin exogenously. Within each cycle, effusion rate, degassing, outgassing and temperature appear to be the dominant controls on the viscosity

of the magma and hence the lava type extruded. This contrasts with other lava domes worldwide, where crystal content or composition have been implicated as primary controls on viscosity. The effects of degassing, outgassing and cooling can be seen within a single eruption cycle which begins with the slow extrusion of a degassed viscous spine, transitioning to lava flows of increasing length as extrusion rates increase. The end of an eruption cycle is marked by decreasing effusion rates, allowing degassed magma to again clog up the conduit and result in extrusion of spines. Ultimately, the eruption stops; and subsequent eruption cycles start from new vents. At any time a dome or lava collapse can modify the cycle and cause a vesicular lava flow to extrude.

The findings from this study explain the association of large hazardous block and ash flows with long blocky lava flows. Here, volatiles are still available in the less-degassed magma to drive fragmentation in the event of lava flow collapse. In contrast, more-degassed facies such as spines are not associated with large block and ash flow events. Additionally, periods of long blocky lava flow extrusion present a significant lahar hazard, since they extend into the headwaters of major drainages and provide abundant loose material from frequent small block and ash flows at their flow fronts. This understanding of block and ash and lahar hazards has important implications for hazard recognition at lava domes worldwide.

THESIS OUTLINE AND PROLOGUE

This thesis is presented in paper format and is set out accordingly. Chapter 1 is a concise introduction suitable for publication, which contains the geological setting and a literature review of dome extrusion at Santiaguito. Chapter 2 provides the methods, which are further explained in detail in Appendix 1. Results are presented in Chapter 3, and are discussed in Chapter 4. Conclusions and implications are summarized in Chapter 5. Raw data is provided in Appendix 2.

As the thesis written in paper format, the immense amount of data and detail that went into creating the figures is not apparent in the text. Appendix 2 represents not only the raw data but showcases the detail of the 15 months work, including 1 ½ months fieldwork in Guatemala. To create the timeline of extrusive activity at Santiaguito, Figure 18, 3 months worth of intensive literature review was required. As well as published literature and theses; SEAN reports, other maps, NASA Landsat images (I downloaded thousands and it killed me a little inside), random photos from the internet, INSIVUMEH brochures, OVSAN reports and email communication with as many volcanologists as possible who had visited Santiaguito in the past 50 years were all used and collated together to create a 60 page table from which the data was interpreted and meticulously constrained to create the timeline.

The maps also represent a significant amount of work. Previous units were mapped by Bill Rose and Rudiger Escobar-Wolf but I went through all the photos (aerial and field photos) that I could acquire, both from this field expedition, and other field expeditions (kindly supplied by Jeannie Scott and Rudiger Escobar-Wolf) to further constrain the timing, outline, interpretation and relationships of flow lobes, smaller lavas and spines. In addition the outline and progress of the new 2011-2012 lava flows was traced from scattered Landsat images and aided by infrequent reports. The results from these could then be placed in the timeline and especially aided the model presented in the discussion. Attention to the detail of cracks and the appearance of vesicular shear zones was especially taken to confine the lines in the zoomed in map. A high resolution map is provided in the Electronic Appendix.

It should also be noted that lots of time was consumed learning about image processing. In order to acquire microlite crystallinity and phenocryst crystallinity in particular, many hours were spent experimenting with different microscopes and cameras to separate out the different phases so the images were processed in Image J. Unfortunately there was no easy solution and for most of the samples the various crystal phases and pores had to be manually separated, taking at least 8 hours per photo, and more than one image needed to be processed in order to obtain a number statistically representative of the thin section. The tomography images were acquired from a combination of two trips to the Australian Synchrotron and also required extensive reconstruction, experimentation and processing.

Enjoy.

ACKNOWLEDGEMENTS

First and foremost I would like to thank Ben Kennedy for arranging this incredible project, it's seriously a better project than anything I could ever dream of. Your attitude towards study in the way that you always try and provide the coolest opportunities for your students so that they have the best time doing their thesis makes having you as a supervisor the best. Thanks for all the encouragement, support and crazy ideas throughout the past two years.

I would like acknowledge my partners in thesis-ship and crime: Sean (Moses) Freeman, Bec (I came in on a cannon-ball) Fitzgerald, Matt (Mantis) Hansen, Aaron (never to be trusted in your bed) Lister, Matt (Ninja) Edwards, Noel (full of surprises) Win, and Dan (Weatherman) Hill. For all your individual quirks, the laughter, the beer tasting sessions, pebble wars, outrageous office pranks and trouble throughout the year, you guys really made this 16 months awesome. With all our very different personalities put together we bonded in some weird but incredibly amazing way that will never again be repeated. "Bitch please." Nothing would have been possible near the end if I didn't have you all to pull together (as a small army) and help out.

Equally as much I acknowledge my field team, Adrian, Armando, Ben and Yan for making the field expedition as epic as it was, compensating for my lack of Spanish, and for always carrying the heavy crap because I was slow. Vamanos. And I have still never had a breakfast as horrible as that one that you made that day Adrian. If there is a day that I ever do, I will let you know. Secondly to our porters, led by Jeronimo who had to carry our rocks all the way back up Santa Maria at the end of each expedition. You are all legends.

To the technical staff on first floor, in particular Rob Spiers, Kerry Swanson, Sacha Baldwin-Cunningham, Cathy Higgins and Janet Brehaut for making all the sample processing happen. Also an acknowledgement to Matt Hughes who hugely helped with all the GIS setup at the start of the project.

I would like to thank Gustavo Chigna, head of volcanology at INSIVUMEH for allowing us to undertake work at Santiaguito and to Julio Cornejo at OVSAN for the hospitality and taking us out to the active lava flows on the other side of the dome and answering many questions.

Also to Rudiger Escobar-Wolf for answering many many questions about Santiaguito and helping with all things GIS and the acquisition of spatial data. The same to Jeannie Scott for answering just as many questions and helping with getting SEM images. And to Fabian, who tried to help with viscosity, but I'm not sure ever did anything more than confuse me and make me read horrible papers and do potentially unnecessary calculations. Nonetheless your attempt help was still appreciated.

This project wouldn't have been possible without funding through a University of Canterbury Masters scholarship, and a GSNZ Hastie Scholarship.

To all the other students and staff who contributed either in a little, or big way: James, Paul A, Siratovich, Jackie, Louise, Alison, Nick, Jo, Emily, Poofy Tom, Clem, Clemchog (R.I.P), Mitch, Narges, Maree, Jim, Mark, Heather, Sarah, Hamish, Flo, Caroline, Darren, and Kay. Churrr and if you ever need any help in return just holler. I am sure I will have a drink and many more laughs with you all in the near future.

To my friends outside of uni, always encouraging me not to go to uni and reminding me that there is a life outside of the office: Primarily Alice, Maezee, Libby, Paris, Paula, Musa, Chris and Rosie.

To the Wino Wednesday Writing Club (WWWC), which we never did any writing at, and where many solid friendships were forged. And to David Bell for the many, many wines and much encouragement.

To my flat: The Piko wine bar and bachelorette pad, open every night of the week (except for the last two weeks of my thesis). Thanks for putting up with me these last few weeks, and for doing all my washing and dishes. To a great year ahead! Louise you are next! To my old flat: Matt, Sam, Jack, Jemma and Pussmouse. I had a great year there too. Nothing will ever compare to our psychedelic hallway.

My final acknowledgement to my Mother Dearest, for whom nothing would ever be possible without. Also my sisters Hannah and Natalie for their support and much laughter. You both are seriously awesome.

TABLE OF CONTENTS

TABLE OF FIGURES

TABLE OF TABLES

1 INTRODUCTION

Dome volcanoes are renowned for collapsing and producing destructive block and ash flows, e.g. Santiaguito 1929 *(Rose 1972b)*, Unzen 1991 *(Yamamoto et al. 1993)* and Soufriere Hills 1997 *(Cole et al. 1998)*. Over the 21st century the formation and growth of lava domes has been monitored and described in a worldwide effort to minimise the increasing death and destruction. Classifying different extrusion products and recognising their associated hazards is one way of understanding the likely future hazards at a volcano.

Physical properties of lava such as crystal content, composition and pore textures can provide information about the magma properties and processes occurring during its ascent in the conduit, which ultimately controls the lava texture and morphology *(Cashman 1992; Anderson et al. 1995; Scott et al. 2012; Scott et al. 2013; Bull and Buurman 2013).* At other domes worldwide, lava morphology and surface textures have been shown to form in response to several emplacement variables, including variations in effusion rate *(Watts et al. 2002)*, emplacement stress regime *(Fink et al. 1990; Hale and Wadge 2008)*, changes in volatile content *(Anderson and Fink 1990)*, and crystallinity or composition *(Watts et al. 2002).* Bulk crystallinity is an important control on lava viscosity *(Lavallée et al. 2007; Mueller et al. 2009; Avard and Whittington 2012; Mader et al. 2013)*, and in addition, microlite crystallinity can provide information about microlite growth in the conduit and ascent rate *(Cashman 1992; Hammer and Rutherford 2002; Watts et al. 2002; Scott et al. 2012)*. The composition dictates the melt viscosity, controlling the melt rheology *(Giordano et al. 2008)*. Pore textures provide information about the degassing history, both prior to and after extrusion, and pore deformation indicates strain conditions *(Shea et al. 2010)*. In combination these tools can be used to decipher the controls on emplacement mechanisms and their implications for future hazards.

At Santiaguito, four domes have extruded sequentially along a linear trend since 1922 *(Fig. 1)*. Extrusion has occurred uninterrupted, with eight documented cycles of extrusion and a ninth occurring in 2011-present *(Fig. 2; Rose 1973a; Harris et al. 2003; Ebmeier et al. 2012)*. Santiaguito has experienced a range of activity during this time including both spine and lava flow extrusion and regular pyroclastic eruptions *(Fig. 1)*. Although El Caliente vent is still active, the three other inactive domes are accessible and the extrusive products have a

range of morphologies. In addition, descriptions of the dome growths have been documented in various sources over time *(Sapper 1926; Williams 1932; Stoiber and Rose 1969; Stoiber and Rose 1970; Rose et al. 1970; Rose 1972b; Rose 1973a; Rose 1973b; Rose et al. 1976; Smithsonian Institution 1980- present; Rose 1987a; Andres and Rose 1995; Anderson et al. 1995; Harris et al. 2002; Harris et al. 2003; Sahetapy-Engel 2004; Harris et al. 2004; Bluth and Rose 2004; Sahetapy-Engel and Harris 2008; Sahetapy-Engel et al. 2008; Forbes 2010; Sanderson et al. 2010; Brill 2011; Holland et al. 2011; Ebmeier et al. 2012).* For these reasons Santiaguito is an ideal location to undertake detailed textural and morphological analysis of lava dome emplacement. Extrusion cycles have been classified based on extrusion rate (low-high-low extrusion cycles) *(Rose 1973a; Harris et al. 2003)*, but as yet classification of lava types and where they fit into the eruption sequence has not been investigated.

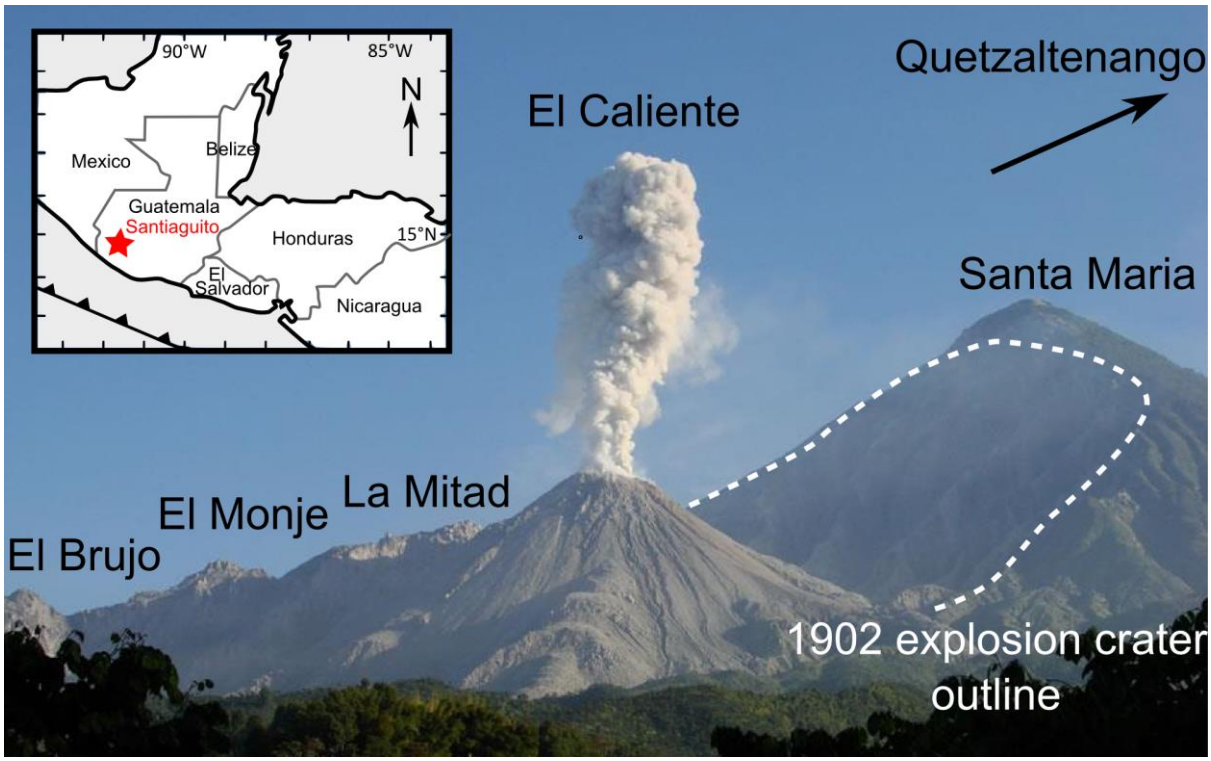

Figure 1 Photo of Santiaguito and Santa Maria from the south, showing a typical eruption from El Caliente. The four different domes are labelled. Quetzaltenango is Guatemala's second largest city and is located 10km north. Photo by Jessica Ball. Inset: Location map of Santiaguito. The subduction zone is shown to the south-east.

1.1 THESIS AIMS

In this study field mapping, remote mapping and sampling of dome structures was undertaken to; (1) characterise and map lava types; (2) use textures of the lava, timing of events and distribution of the different lava types to explain the controls behind the lava types; (3) constrain eruption cycles based on the timing and textures of the lava types; (4) to apply what is known about the degassing and outgassing history to explain the hazards associated with the different lava types.

1.2 GEOLOGICAL AND VOLCANOLOGICAL SETTING

Santiaguito lies in the 1902 explosion crater of parent volcano Santa Maria *(Figure 1; Williams and Self 1983)*. Santa Maria is located on the southern edge of the Xela Caldera – part of the Central American Volcanic Arc which extends from Mexico to El Salvador *(Duffield et al. 1993; Bennati et al. 2011)*. Subduction of the Cocos plate under the Caribbean plate to the SW is the origin of the volcanism *(Fig. 1, Bennati et al. 2011)*. Eruptive activity at Santa Maria began around 103 ka, and the edifice was constructed in four stages before a 25 ka year period of quiescence prior to 1902 *(Rose et al. 1977; Rose 1987b; Conway et al. 2013)*. As well as being in located in a centre of compression and uplift resulting from subduction, Santa Maria also lies on the eastern border of the strike-slip Zunil fault zone *(Bennati et al. 2011)*. Numerous faults cut through Santa Maria and Santiaguito edifices with a rough east to west orientation *(Escobar-Wolf et al. 2010).*

1.3 DOME EXTRUSION AT SANTIAGUITO

In 1902 Santa Maria had a devastating Plinian eruption, depositing 8.5 km^3 dense volume of dacite as fall deposits, and leaving an explosion/collapse crater on the south-west side of the edifice *(Fig. 1;* Rose 1972a; Williams and Self 1983). After no eruptive activity for 20 years, volcanic activity resumed at Santa Maria in 1922, and a dome complex grew in the crater - Santiaguito. Volcanic activity has occurred without interruption since then, and is still continuing today. Four domes have extruded – El Caliente, La Mitad, El Monje and El Brujo *(Fig. 1)*, with the growth of each new dome beginning after the cessation of activity at the previous dome, and moving progressively to the west *(Fig. 1, 2; Harris et al. 2003)*. El Caliente has been termed the main vent, as it experienced extensive hydrothermal activity

throughout growth of the lateral vents, and because it has been the only centre of activity since 1977 *(Rose 1972b; Rose 1987a)*. In December 2012 activity consisted of regular explosions (≤2/h, <1 km high) *(Harris et al. 2003; Holland et al. 2011)*, and simultaneous lava flow extrusion accompanied by frequent incandescent rock falls (1/min). During the annual rainy season remobilisation of the loose rockfall material causes lahars which impact the fluvial system up to 60 km downstream *(Harris et al. 2006)*. The recent observed behaviour is consistent with activity at Santiaguito throughout its growth, and the ash eruptions have been suggested to be a by-product of the lava extrusion *(Johnson 2004; Bluth and Rose 2004; Johnson et al. 2008; Holland et al. 2011)*. Infrequent larger eruptions and dome or lava flow collapse events have caused larger ash plumes (<6 km) and block and ash flows; the most notable of which occurred in 1929 when a collapse and explosion at El Caliente sent a pyroclastic density current 11 km downstream, killing up to 5000 people *(Rose et al. 1976; Simkin et al. 1994).*

The first Santiaguito lavas extruded in 1922 were chemically very similar to the 1902 eruption products - porphyritic lavas dominated by phenocrysts of plagioclase feldspar (~20-30%), pyroxene, titanomagnetite and amphibole (combined total ~5%) *(Rose 1972b; Singer et al. 2011; Scott et al. 2013).* Although the phenocryst assemblage hasn't changed over time, the bulk silica content has. Erupted magma has become progressively less evolved with a decrease in bulk SiO_2 from 65.9-62.0 wt.% SiO_2 *(Scott et al. 2013).* Samples from Harris et al. (2003) indicated that this decrease happened gradually post 1970, but more recent research by Scott et al. (2013) suggest that the depletion was even more gradual, beginning as early as the 1930's. The magma chamber is calculated to be located in the lower crust, 12-24 km deep, with no evidence of a shallow storage zone *(Scott et al. 2012)*. A stratified magma chamber model has been used to explain the depleting silica content, where there is a vertical gradient in composition from basalt to dacite *(Scott et al. 2012)*. As the supply of dacite at the top was exhausted, Santiaguito is now erupting the andesite from below *(Scott et al. 2012)*.

Growth at Santiaguito shows a cyclical pattern, with 3-6 year long episodes of high extrusion rate (0.5-2.1 $m^3 s^-$) followed by 3-11 year periods of low extrusion rate (≤0.2 $m^3 s^-$) *(Fig. 2; Harris et al. 2003)*. The time averaged growth rate, as estimated by detailed field mapping, is

0.46 m^3 s^- *(Harris et al. 2003)*. To date, 9 different cycles have occurred, with the latest emplacement of 2 lava flows >2 km length in 2011-2013 signifying the start of a new extrusion cycle *(Fig. 2; Harris et al., 2003; Ebmeier et al., 2012, this study).*

The style of dome growth at Santiaguito progressively transitioned over time. Activity prior to 1925 was endogenous, characterised by subsurface build-up of magma to make a dome. Between 1925-1958 a combination of endogenous and exogenous behaviour occurred, and post 1958 growth has been solely exogenous, where magma extrudes at the surface *(Rose 1987a; Harris et al. 2003)*. Harris et al. (2003) calculated that the transition initiated in 1925 when dome pressurisation reached a threshold that was significant enough to break the outer carapace, allowing exogenous units to extrude out, and that after 1958 increasingly favourable rheological conditions explain the solely exogenous growth. Harris et al. (2003) suggested that a continued decrease in extrusion rate, silica content and increase in duration between high flux periods could be a sign of magma source exhaustion. However, recent measured extrusion rate averages (2000-2009) are consistent with the time averaged growth rate, and the occurrence of the 2011-2013 spurt is not consistent with source exhaustion *(Harris et al. 2004; Ebmeier et al. 2012)*.

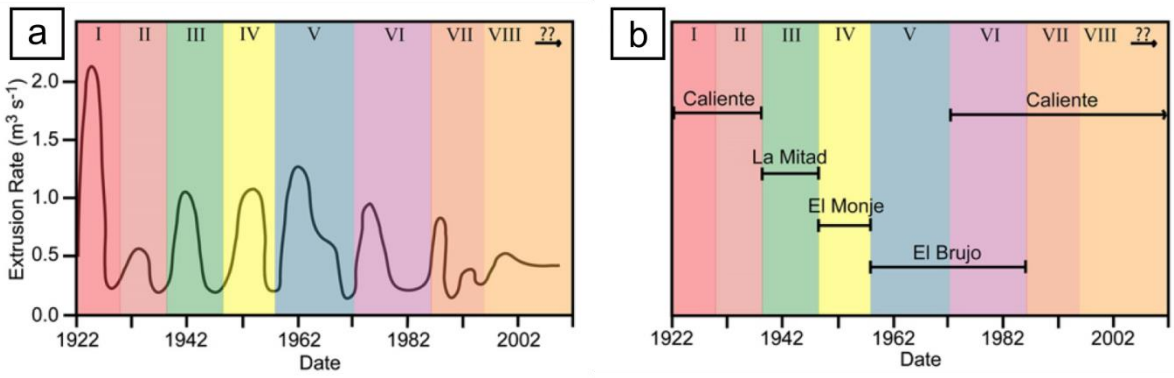

Figure 2. Cyclic extrusion patterns and active domes at Santiaguito. (a) Average extrusion rate and corresponding extrusion cycles (colours) at Santiaguito, data from (Harris et al. 2003; Ebmeier et al. 2012). (b) Active domes at Santiaguito. References: (Rose 1973a; Harris et al. 2003). Figure adapted from Scott et al. (2013). Most recent extrusion cycle not shown.

2 METHODS

Mapping at Santiaguito was carried out through field work in November-December 2012, and the outlines of units were based on high-resolution aerial orthophotos taken in 2006 by the Instituto Geographico Nacional (IGN) of Guatemala. Interpretation and timing was aided by historic aerial photos, as well as photos acquired in the field. Features such as the outline of the main lava flows were adapted (in consultation with the authors) from Escobar-Wolf et al. (2010) and Ball et al. (2013). My focus was on mapping summit features such as individual spines and lobes, their strikes and dips, and unique textural or structural features associated with them. Thirty-five samples were taken from a range of these features on the dome summits and the recent lava flows, ranging in age from 1940–2012.

Physical properties of these samples were quantified through porosity, microlite and phenocryst crystallinity measurements. Approximate volume measurements were made by measuring aerial widths and lengths of units in GIS software and an average height from the field. Porosity was calculated using the He-Ultrapycnometer 1000 at Massey University. Phenocryst crystallinity was calculated by repeated image processing of thin section photomicrographs. Microlite crystallinity was quantified by image processing of Scanning Electron Microscope (SEM) backscatter images taken at the University of Canterbury. Of particular note, the microlite crystallinity between samples published in Scott et al. (2012) and this study consistently differed by ~20%. However from discussion with Dr Scott, and without direct comparison of the same image on both SEM's, the difference as an image quality discrepancy cannot be discounted. In recognising that there is significant variation in microlite content within a unit, I report and discuss both the microlite content calculated in this study and by Scott et al. (2012). Composition was not measured in this study, as there is already a wide range of both whole rock and melt geochemistry data already published. However, the composition was reanalysed in light of the findings of this study.

Textural analysis of crystal orientation and size was achieved using standard thin sections. Pore shapes and orientation were analysed using a combination of techniques. Thin sections were impregnated with ultra-violet (UV) glue and the UV photomicrographs revealed 2D small scale pore texture detail such as pore shape and their relationship to phenocrysts. The

pores could then be analysed in 3D using tomography data acquired at the Australian Synchrotron. 3D tomography reconstructions aided with the interpretation of pore shapes from the UV thin sections and visually displayed their connectivity.

An extensive search of the literature, communication with locals, Smithsonian Institution Scientific Event Alert Network (SEAN) bulletins, Santiaguito Volcano Observatory (OVSAN) photographs, Instituto Nacional de Sismología, Vulcanología, Meteorología e Hidrología (INSIVUMEH) volcanic alert bulletins and NASA Landsat images aided with the construction of a volcanic activity timeline.

A full methodology is provided in Appendix A, raw data in Appendix B, and digital files in Appendix C.

1.0 RESULTS

Four lava-types were identified during field mapping, and later refined using textural analyses *(Table 1)*. The distribution can be seen in the geological map *(Fig. 3)*, and porosity, composition and crystallinity are compared in Figures 4, 5 and 6 respectively.

Table 1. Summary properties of the lava types at Santiaguito.

	Spine	**Summit Blocky Lava Flow**	**Long Blocky Lava Flow**	**Vesicular Summit Lava Flow**
Description	Sub-vertically extruded units	Short lava flow with a blocky top	The longest type of lava flow with a blocky top	Short very vesicular flow
Rough Volume	Low <400 000 m^3	Low ~200 000 m^3	High 400 000 – 1 600 000 m^3	Low <300 000 m^3
Dip	High 38°-90°	Low 10°-30° With shallow dipping flow fronts (approx. <50)	Low 5°-30° With shallow 32°[ɣ] to steep 70° dipping flow fronts	Low 5°-30° With steep dipping flow fronts (approx. >50°)
Porosity (range)	4-22.8%	11†-27.6%	3†-78.8%	23-69%
Porosity (average)	11.7%	19.0%	31.0%	47.5%
Bubble Textures	Deflated interconnected pores (primary) and inflated interconnected pores (minor)	-	Inflated interconnected pores, and deflated interconnected pores (both may be stretched)	Inflated interconnected pores
Crystallinity	27.2-34.0%	30(+-5)†%	34.1-35.2%	31.4-33.8%
Microlites (% of groundmass)	41-45%	-	40-43%	37-40%
Microlites (% of groundmass)*	21.4-26.8%	~23%	18.9-26.3%	-
Composition	64-65 wt.% SiO_2	62-65 wt.% SiO_2	61.9-65 wt.% SiO_2	62-65 wt.% SiO_2
Extrusion Rate	Low (≤0.2 $m^3 s^{-}$).	Low - Medium	Medium – High (0.5-2.1 $m^3 s^{-}$)	High (2.4 $m^3 s^{-}$)

* Scott et al. (2012) † Avard and Whittington (2012) ɣ Harris et al. (2006)

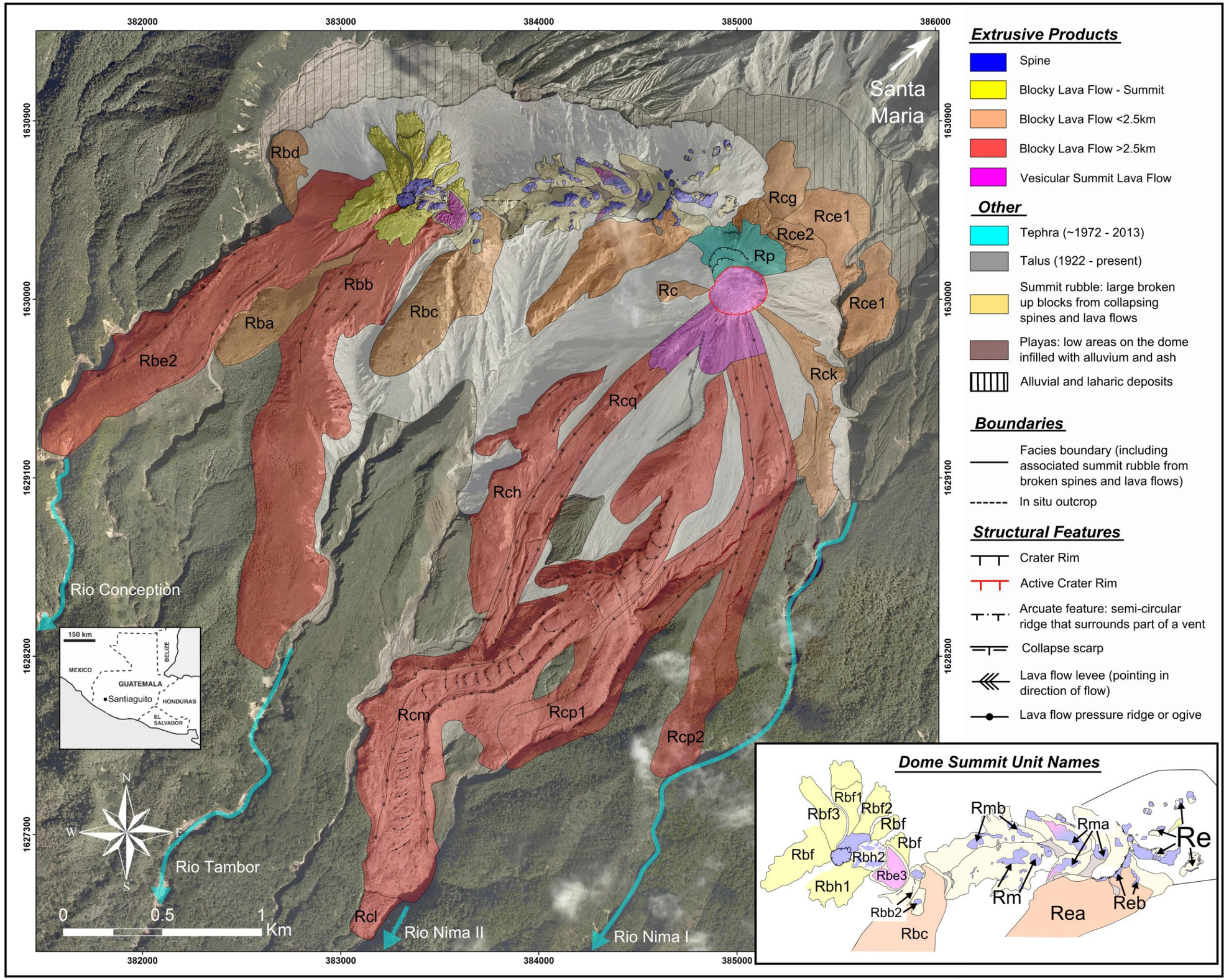

Figure 3. Lava type map of the Santiaguito lava dome complex Nov 2012. Units Rcq and Rcp are from the recent 2011-2013 high effusion rate sequence. This map is developed as a companion map to Escobar-Wolf et al. (2010) and Ball et al. (2013). Pre 2006 dome and lava flow features were mapped from aerial 0.5 m/pixel resolution aerial orthophotos 1860-II-14 and 1860- II-19 (acquired between November 2005 and April 2006 by the IGN) as well as by direct field mapping. Recent post 2006 collapses and lava flows were mapped from NASA ASTER images and field observations. Unit names are labelled following Rose (1976) and Escobar-Wolf (2010). "R" stands for Recent, and is followed by a prefix which denotes the dome. "c" = El Caliente, "e" = La Mitad, "m" = El Monje, and "b" = El Brujo. The third letter represents the age of the unit. Note some older units have been eroded or buried by subsequent units. The number at the end denotes the subunits, if any. A full high resolution map is provided in the appendix.

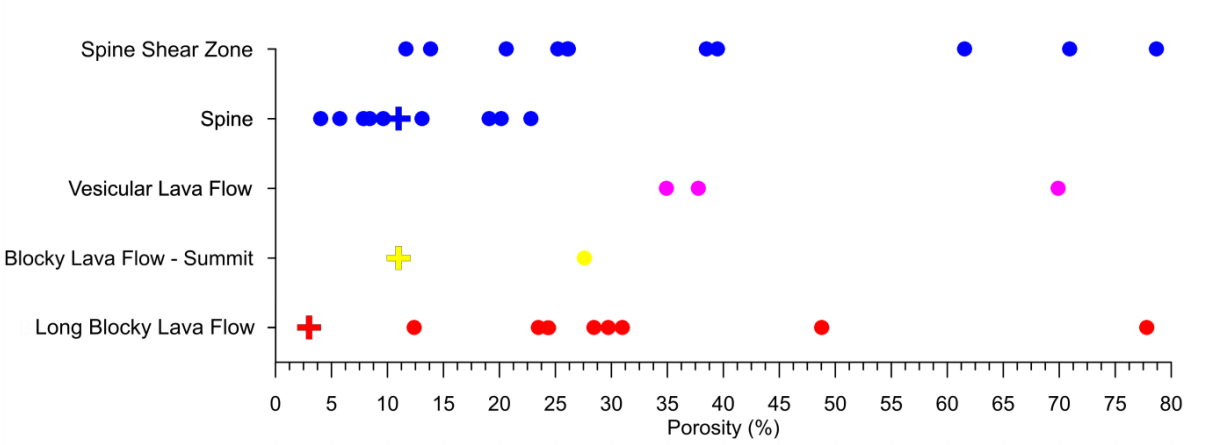

Figure 4. Total porosity of extrusive products at Santiaguito measured using a He-Ultrapycnometer 1000. Circles are data from this study, and crosses are values from Avard and Whittington (2012). Less than 1% of the porosity was isolated in all the samples used in this study, so only total porosity is shown, which is equivalent to the connected porosity.

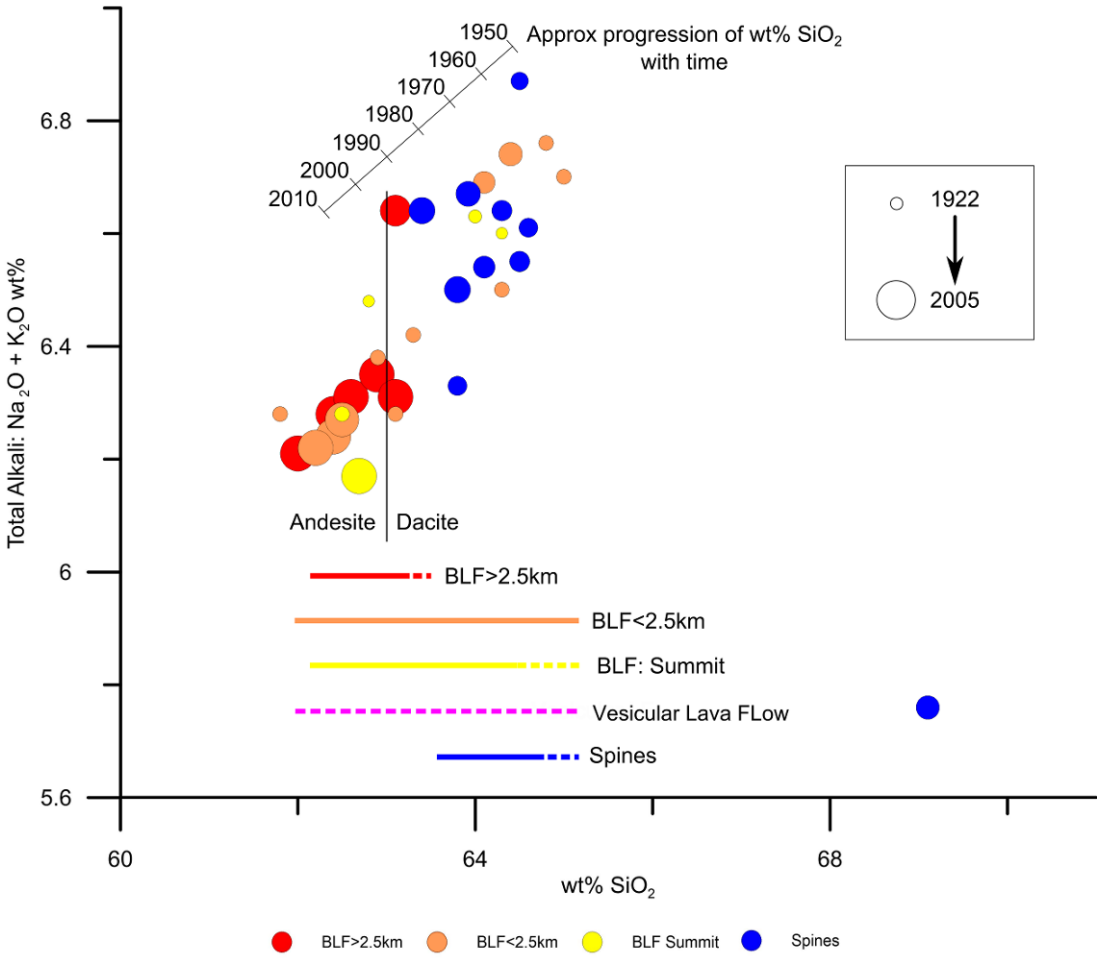

Figure 5. Composition of extrusive products at Santiaguito from published values. The black line with dates on is created from the trend of bulk SiO_2 over time, calculated from the same data set. Dates pre 1950 are not shown as the SiO_2 varied significantly before that date. The coloured lines show the compositional range of the different facies based on their SiO_2 content (plain line) and date of extrusion (dashed line). Data sourced from Rose (1972), Avard and Whittington (2012), and Scott et al. (2013).

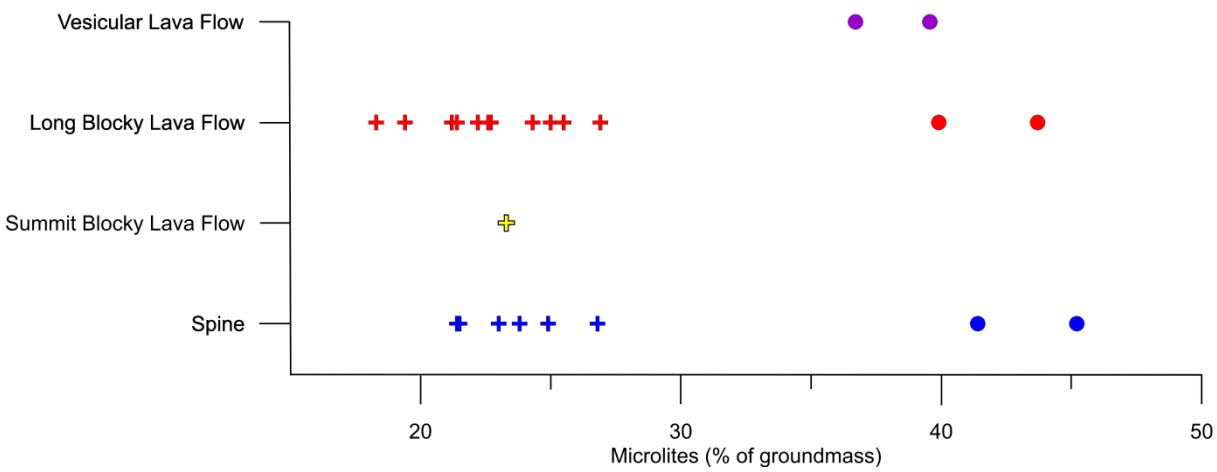

Figure 6. Microlite content (as a percentage of groundmass). Crosses are data published in Scott et al. (2012), and circles are data calculated as part of this study.

2.1 Blocky Lava Flows

A lava flow with a coherent interior, and a top surface composed of smooth sided, angular – subrounded blocks 10 cm - 2 m in size *(Fig. 7)*. These flows reach 70 m thick, 500 m wide and vary in length from 500 m – 4 km. Regular small block and ash flows and avalanches (>1/min) initiate from collapse of both the flow front and sides, reaching up to 400 m. Infrequent large collapse events from the lava flow fronts also occur, travelling up to 4 km from the flow toe *(Rose 1973b; Rose et al. 1976).*

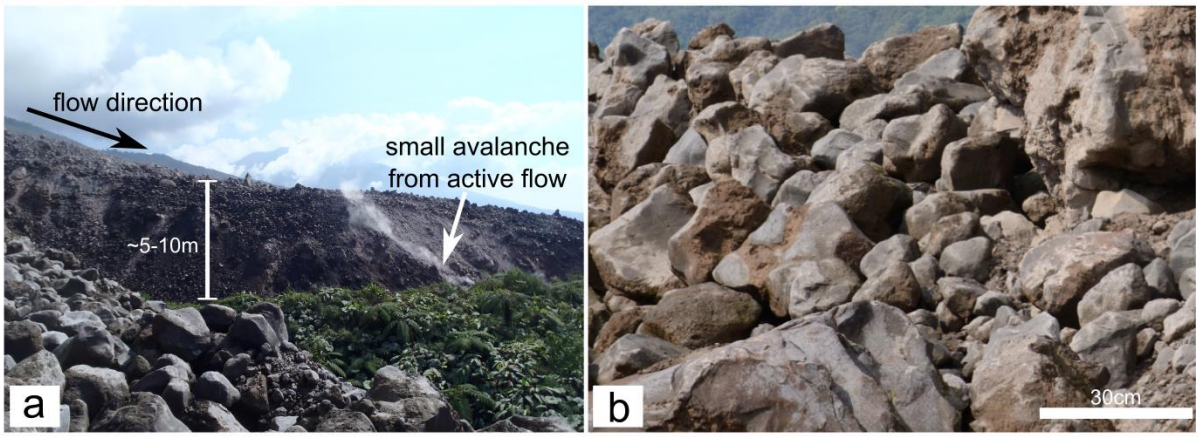

Figure 7. Photos of blocky lava flows. (a) Side view of an active long blocky lava flow. (b) Close up of the top of a blocky lava flow, photos taken ~1 km from vent.

2.2 LONG BLOCKY LAVA FLOWS

Long blocky lava flows are lava flows that reach that base of the cone and extend up to 4 km following local depressions, typically river channels *(Fig. 3)*. Some results are separated between blocky lava flows that reach lengths over 2.5 km and flows and those that do not reach 2.5 km (but still reach the base of the cone). These flows have a low dip angle and form the largest volume extrusive products at Santiaguito *(Table 1)*, with the most pronounced ogives (pressure ridges) and levees *(Fig 7)*. Thicknesses reach 70 m, with widths of up to 500 m. Their flow fronts may be shallow (32° *(Harris et al. 2002)*) to steep (70°) *(Table 1)*. In one location on El Monje a ~20 m cross section of the interior of the flow from La Mitad was exposed. The top ~5 m was notably more vesicular than the bulk of the interior. The same observation was made by Rose (1972) who noted a 10 m vesicular top on exposed cross sections of flows from El Brujo. It is this type of flow that produced the devastating block and ash flows of 1973 *(Rose 1973b; Rose et al. 1976)*. The longest lava flow *(*Rcm*, Fig. 3)* is 4 km long and was extruded continuously between 2000-2002 *(Fig. 18)*.

Several samples were collected from the rubbly tops of the 2011-2012 flows, 1.5 km from vent, and one sample was collected from the main interior of the flow from La Mitad. Results show that porosity ranges from 3 to 78.8% *(Fig. 4)*, with an average porosity of 31% *(Table 1)*. The interior porosity of 24%, although I recognise that vesicularity is likely to be heterogeneous, reflected in the samples from the blocky top *(Fig. 4)*. Pores range in shape and size between samples, including inflated and deflated interconnected pores with varying degrees of flattening and shearing *(Fig 8; 9)*.

In thin section pores reach a maximum diameter of 1 cm in size, however tomography *(Fig. 9)* and connected porosity *(Fig. 4)* shows that these pores form connected networks reaching total lengths of several centimetres and extending beyond the dimensions of our 4 cm samples *(Fig. 9)*. Most pores have ragged walls marked by the protrusion of phenocrysts and microlites. Pores in the samples with the highest porosity have dominantly convex pore surfaces with concave remnants of bubble wall protrusions which indicate pore coalescence *(Fig. 8; 9)*. These pores are the largest pores in blocky lava flows and are usually connected to other large pores *(Fig. 9)*. I refer to these as “inflated, interconnected pores.” Many of these

inflated interconnected pores show preferential long-axis alignment *(Fig. 8; 9)*. At the pore tip the aligned pores either pinch out or have blunt terminations *(Fig. 8)*, whereas non-aligned pores only have blunt terminations *(Fig. 8)*.

In the densest samples the pores have smaller maximum diameters. Some pores have and both concave and convex surfaces and evidence of remnant pore wall protrusions, but have little alignment *(Fig. 8; 9)*. However, in most cases this pore-type is aligned, with dominantly convex pore walls and little evidence of pore wall protrusions. These pores form networks of interconnected tubes *(Fig. 8; 9)*. I refer to these as "deflated, interconnected pores." Both deflated and inflated interconnected pores are dominantly located adjacent to phenocrysts or lithic inclusions *(Fig. 8)*.

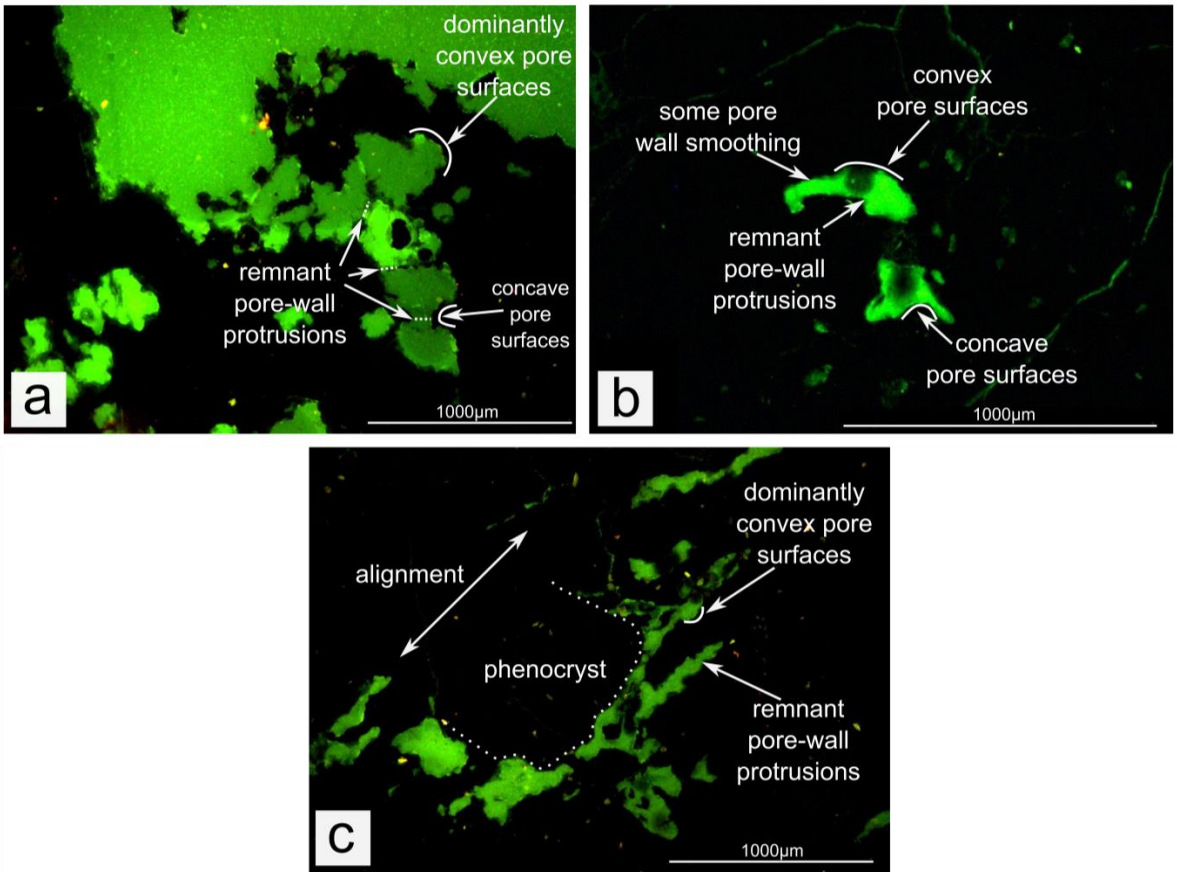

Figure 8. UV photomicrographs of pores in blocky lava flows. Note: Pores are green. (a) Inflated interconnected pores, (b) deflated interconnected pores and (c) deflated interconnected pores with stretching.

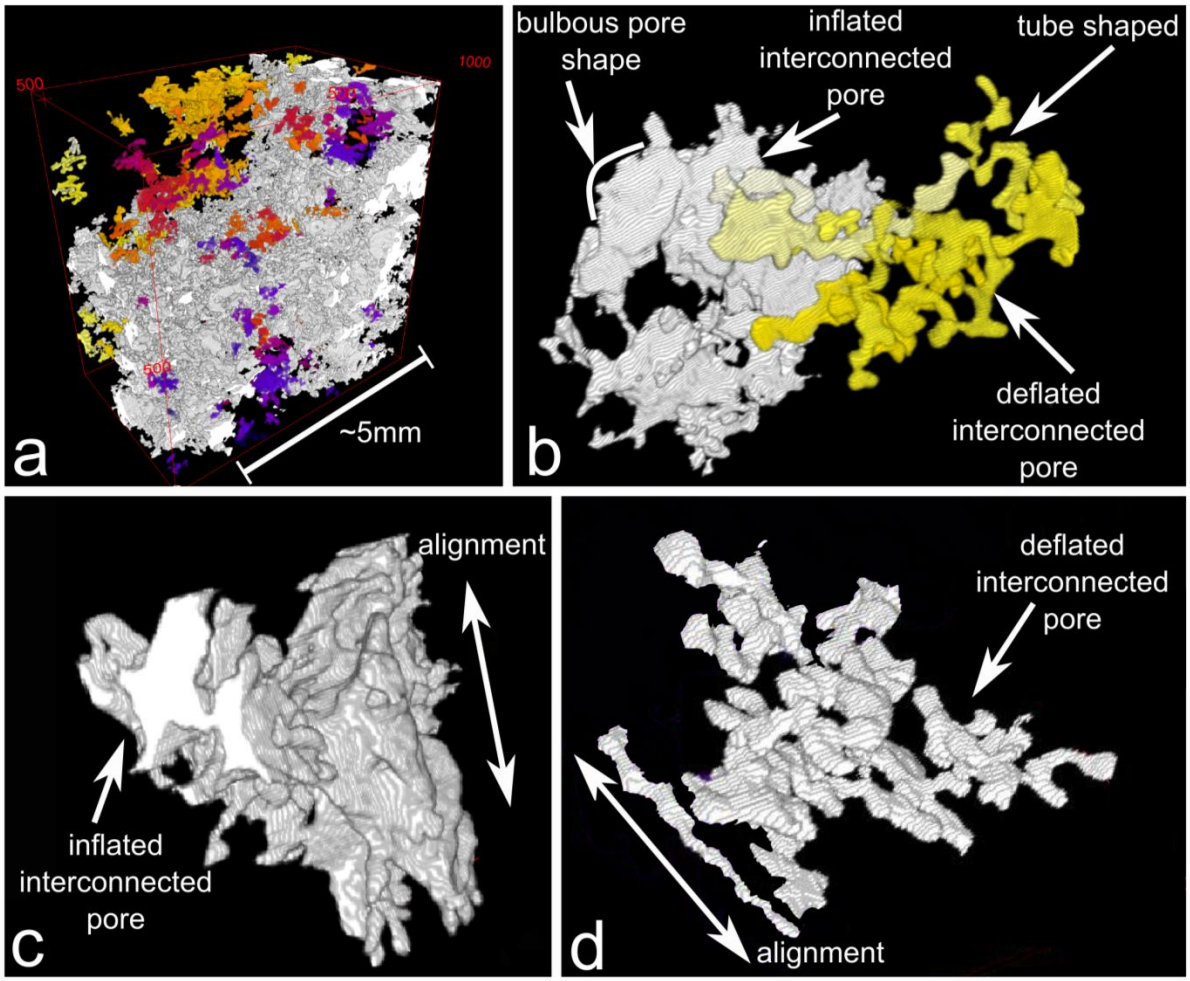

Figure 9. 3D tomography reconstructions of pores in blocky lava flows. (a) Large scale image of pores in a medium porosity sample. Each colour denotes an individual pore. As the sample is predominantly white (i.e. one colour), it shows the porosity is largely connected. Note: only the largest 200 pores were reconstructed. The majority of the sample contains inflated interconnected pores, however the top left hand corner shows a dense section of the sample, and contains dominantly deflated interconnected pores. (b) Singular inflated interconnected pore and deflated interconnected pore. (c) Inflated interconnected pore with stretching (seen at the tips), and possible flattening (overall shape). (d) Deflated interconnected pore with stretching. Note individual pores in (b), (c) and (d) are less than 1mm across. Refer to electronic appendix (f) for a 360° video of (a).

Blocky lava flows >2.5 km are typically andesites ranging from 61.9 to 63.5 wt.% SiO_2, and blocky lava flows >2.5km are andesites to dacite 62-66 wt.% SiO_2 *(Fig. 5; Rose 1972b; Avard and Whittington 2012; Scott et al. 2013)*. The phenocryst crystallinity in the 2011/2012 flow sequence *(Fig. 3)* is 34-35%, and in the pre 1990 flows, 27-33% *(Table 1)*. The microlite crystallinity in our samples was 40-43% *(Fig. 6)*, giving a total crystallinity of 60-78%. Lower microlite crystallinities of 18.9-26.3% were measured by Scott et al. (2012) *(Fig 6)*, indicating a possible range in total crystallinity of 46-61%.

Regular ash eruptions at a frequency of ~2/hr and ongoing vent degassing accompanied long blocky lava flow extrusion during January 2000 when Harris et al. (2002) undertook their field campaign. Lava was observed to extrude from a low active dome (~10m above the vent rim). The same observations were made during this field campaign, which was timed with the tail-end of the 2011-2012 blocky lava flow extrusion. Constant degassing occurred from short-lived shifting fissures at the top and rim of the vent. Johnston et al. (2013) observed episodic bulging (up to 10m) of the lava pad on top of the conduit, which coincided with radial tilt and rapidly deflated upon eruption. Furthermore, regular block and ash flows (<500m) could be seen initiating almost constantly from both the lava flow toe and sides.

2.3 Summit Blocky Lava Flows

Summit flows are low volume flows *(Table 1)* which extend a short distance down the sides of the dome, but never reach the base. These flows repeatedly collapse from shallow dipping flow fronts *(Table 1)* to produce block and ash flows, removing lava from the flow front at a similar rate as it is extruded from the vent. This therefore prevents flow-front advance to the base of the dome.

Summit flows were the only kind of lava flow extruded between 2004-2011, allowing good correlations between summit activity and the lava flows to be observed. Forbes and Johnson (2010) showed that blocks on the summit of the dome moved in a southwest direction consistent with lava flow extrusion. Brill (2011) monitored explosions for a two year period between 2008 and 2010, and found that there was no relationship between the repose period and explosively of the next eruption. Ongoing degassing from the conduit occurred throughout summit flow extrusion. Additionally, Johnson (pers. comm 2014) suggests from visual observations over several field seasons that explosions during periods of summit lava flow extrusion were similar in frequency to, but less explosive than, explosions that occurred during periods of longer blocky lava flow extrusion. However this observation requires further research.

Thicknesses of summit flows are significantly thinner than the longer flows, generally not reaching over ~30 m. Minor levees sometimes develop but ogives have not been observed. A sample from the summit flow on Mitad dome had a porosity of 27.6% (this study), and a

sample from a 2005 summit flow from El Caliente had a porosity of 11% *(Fig. 4; Table 1; Avard and Whittington 2012)*.

Pores within the summit lava flow sample are either convex with concave remnants of pore wall protrusions and minor preferential elongation (i.e. inflated interconnected pores) *(Fig. 8)*, or convex and concave, still with evidence of remnant pore wall protrusions (i.e. deflated interconnected pores) *(Fig. 8)*. Low isolated porosity (<1%) *(Fig. 4)* indicates that most pores are connected. Summit flows have been extruded at times throughout the activity at Santiaguito, and therefore have a compositional range of 62-65 wt.% SiO_2 *(Fig. 5; Table 1; Rose 1972b; Avard and Whittington 2012; Scott et al. 2013)*. The phenocryst crystallinity is 30±5% *(Table 1; Avard and Whittington 2012)*, and the microlite crystallinity was not measured, although microlite crystallinities of 23% were measured by Scott et al. (2012) *(Fig. 6)*, giving a total crystallinity of at least 53%. Again, my measurements of microlite crystallinity on other lavas are systematically ~15% higher than Scott et al. (2012), therefore suggesting a total crystallinity up to 68%.

2.4 Vesicular Lava Flows

These are highly vesicular flows that are restricted to the summit zone of the domes. In contrast to the blocky lava flows, the flow tops are coherent and in-situ *(Fig. 10)*. Vesicular lava flows are 10-20 m thick, low volume *(Table 1)*, and less than 200 m wide. No samples have been compositionally analysed, but given that they were extruded throughout extrusion at Santiaguito, and based on a broad decrease in silica over time, I crudely estimate that they have a broad compositional range of 62-65 wt.% SiO_2 *(Fig. 5; Table 1; Rose 1972b; Avard and Whittington 2012; Scott et al. 2013)*. Sample analyses show that the phenocryst content ranges from 27-33% *(Table 1)* and the microlite crystallinity is 36.7-39.6% *(Fig. 6)*, giving a total maximum crystallinity of 73%. The microlite crystallinity for this facies was not measured by Scott et al. (2012).

Porosity is 23-69% *(Fig. 4)*, with an average porosity of 48% *(Table 1)*. Most pores have ragged walls marked by the protrusion of phenocrysts and microlites. In thin section pores reach a maximum diameter of 1 cm in size, however tomography *(Fig. 12)* and connected porosity data *(Fig. 4)* show that these pores form a connected network reaching total lengths

of several centimetres and extending beyond the dimensions of our 4cm samples. Tomography *(Fig. 12)* and thin sections *(Fig. 11)* show that the pores are inflated and interconnected, with dominantly convex edges and with concave remnant pore wall protrusions. Pores from the top of the flow are not strongly aligned, though thicker horizontal bands of coalesced pores are present *(Fig. 12)*.

There are three examples of vesicular lava flows currently preserved at Santiaguito *(Fig. 3)*. Two were the first products to extrude from separate small vents on El Monje, and laterally transitioned into spines over ~20 m *(Fig. 3)*. The third vesicular flow is preserved in large semi-circle shaped mass on El Brujo, with deep (~6-8 m) gullies that splay out from the focus of the semicircle *(Fig. 10; Appendix Map)*. These gullies extend all the way out to the perimeter *(Fig. 10)*. The bottoms of the gullies were disguised by vegetation so couldn't be analysed. In contrast to the other vesicular lava flows, this flow formed at the end of the timeline of extrusion of a blocky lava flow >2.5 km *(Fig. 18)*. In addition to the four vesicular flows presently preserved at Santiaguito, Anderson et al. (1995) noted that vesicular lava was also observed prior to 1925, and for a short period when activity returned to El Caliente in 1977 *(Fig. 18)*.

One vesicular lava flow was witnessed extruding during this field campaign. A vesicular lava flow occurred after a moderate dome and summit lava flow collapse on November 28th 2012 *(Fig. 18)*. The collapse occurred after a gap in explosive eruptions of several days, triggering constant block and ash flows for two hours and leaving a scarp on the southern side *(Fig. 10c)*. There were no further eruptions witnessed for at least a week post collapse. Although no samples exist, observations from a distance that the flow front was rounded and steep *(Table 1)* and the flow top was not as rubbly as the tops of blocky lava flows, suggest that this is a vesicular lava flow *(Fig. 10)*.

Based on a flow length of 300 m, width of 200 m *(Fig. 3)*, and average thickness of 10 m *(Fig. 10c)*, the extrusion rate for this flow was crudely calculated using an ellipsoid to be 2.4 m^3 s^{-} *(Table 1)*. Note that the both and contribution of lava flowing into the active long blocky lava flow (Rcp) at the time is unknown *(Fig. 3)*. The collapse did not appear to effect the long lava flow as the summit zone was still intact and the flow front was observed progressing 6 days later. Photos of El Caliente a year later show that the collapse scarp is completely infilled

with a new blocky lava flow that extends down to the base of El Caliente *(Fig. 10d)*. There is no residual evidence of the vesicular lava flow.

Reanalysis of photos of the fresh lava flow following the El Caliente 1929 explosion and dome collapse showed that this lava flow also lacked a blocky carapace and had a steep rounded flow front. Therefore I also classify this flow as a vesicular lava flow.

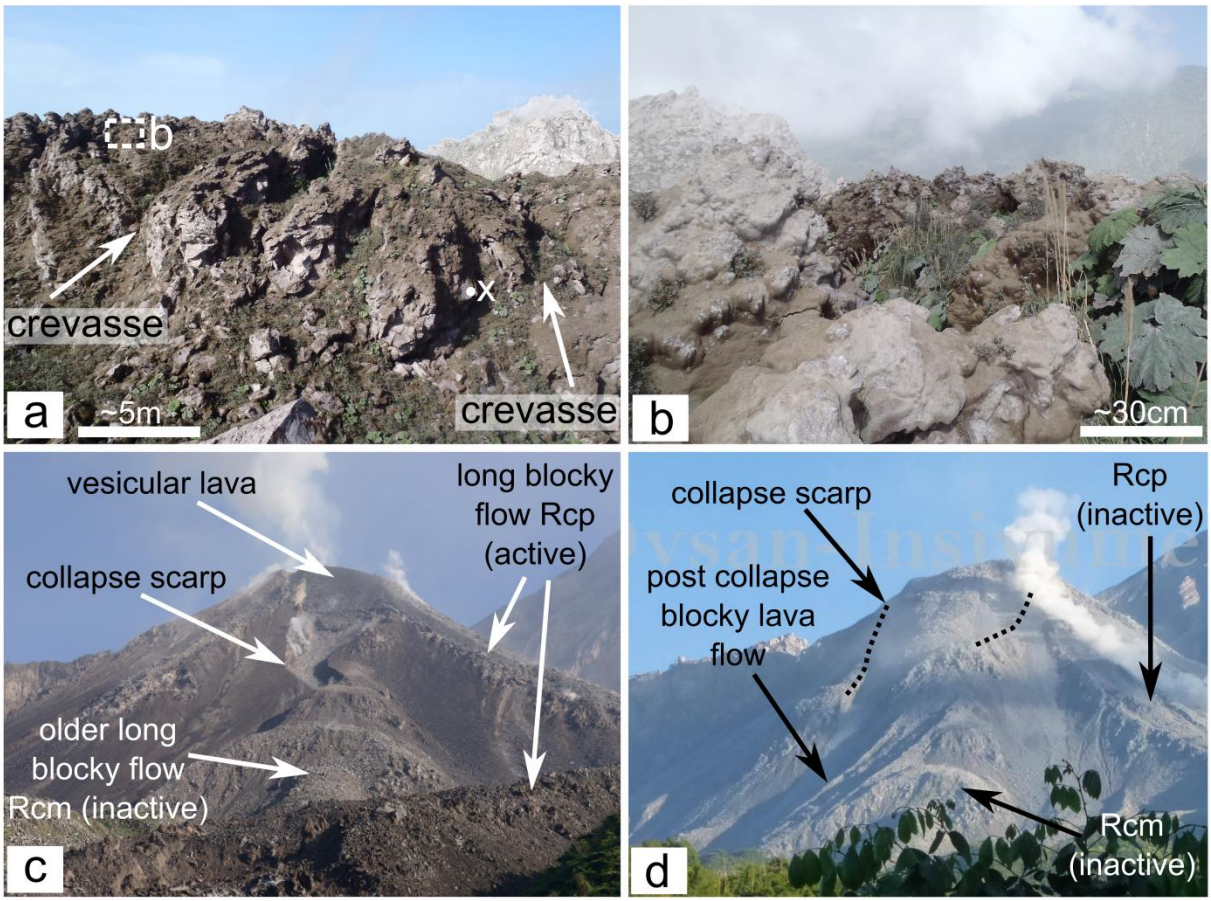

Figure 10. Photos of vesicular lava flows (a-c) and transition of a vesicular lava flow into a blocky lava flow (d). (a) Side view of a vesicular lava flow on El Brujo showing location of crevasses. X marks location of sample shown in Figure 11b. For a detailed map of the crevasses, see Fig. 3. (b) Close-up of the top surface. This is the location of the sample Figure 11a. (c) View north towards El Caliente where a vesicular lava flow is infilling the 28th November 2012 collapse scarp created 6 days prior. (d) View North towards El Caliente approximately one year after the collapse showing that the collapse scarp is infilled and a new blocky lava flow has developed. Photo taken on the 9/01/2014 by INSIVUMEH.

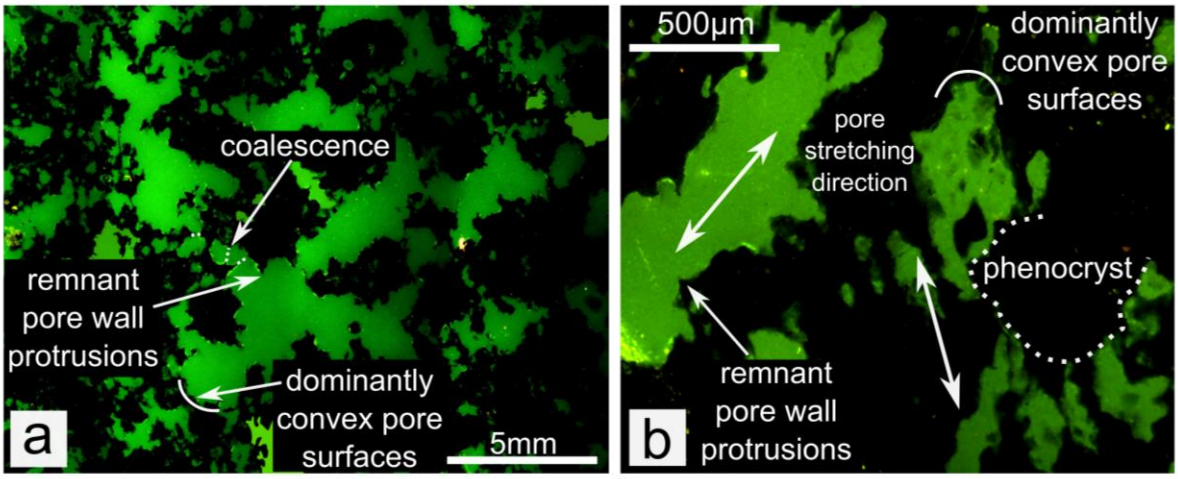

Figure 11. UV photomicrographs of pores in vesicular lava flows. Note: pores are green. (a) Inflated interconnected pores, and (b) inflated interconnected pores with stretching. Sample locations shown in Fig. 10 and stretching direction in (b) is vertical.

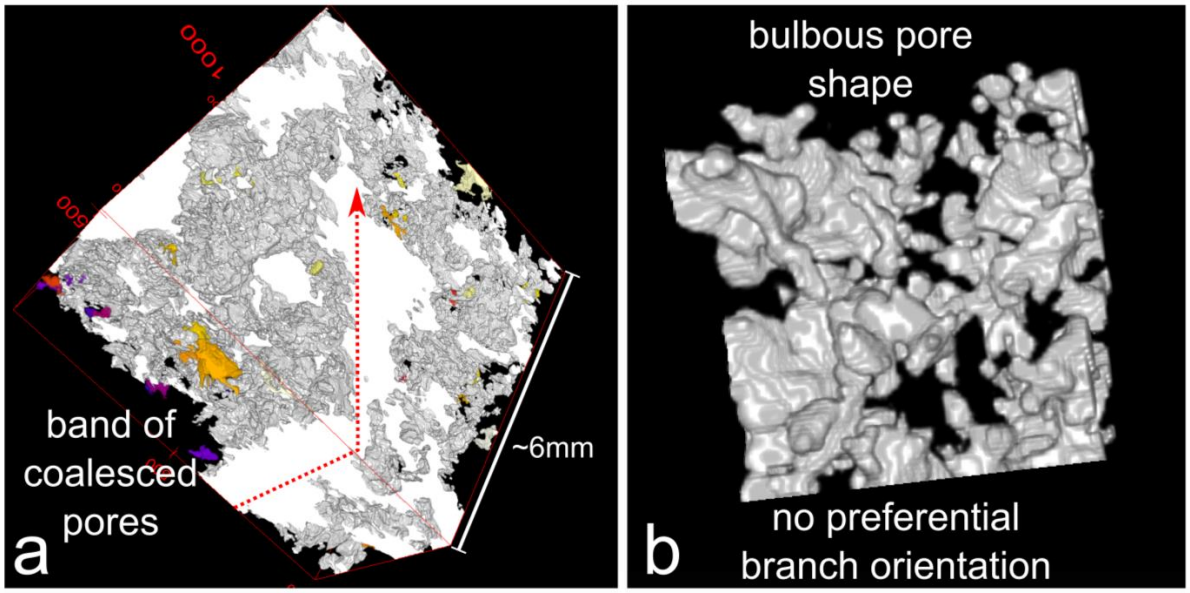

Figure 12. 3D tomography reconstructions of pores in vesicular lava flows. Each colour denotes an individual pore. As the sample is predominantly white (i.e. one colour), the porosity is largely connected. Note: only the largest 200 pores were reconstructed. (a) Large scale image showing a band of coalesced pores. (b) Small sample showing the inflated interconnected pores. Total image size less than 1mm across. Refer to electronic appendix (d) and (e) for 360° videos.

2.5 SPINES

Spines are dense, coherent masses of lava that extrude sub-vertically above the vent *(Table 1)*. They are low volume *(Table 1)* and are restricted to the summit of the domes *(Fig. 3)*. They are usually linear in shape, 10-200 m long, 3-50 m wide and 5-70 m tall *(Fig. 13)*. Observations of spine extrusion at Santiaguito report that sections of spines regularly collapse forming block and ash flows that reach the base of the dome, or are repeatedly grown and blown out of the vent by an explosive eruption *(Williams 1932; Rose 1973a)*. The spines are commonly characterised by zones of dense material (>3 m wide) which are often cracked, separated by regularly spaced subvertical scoriaceous or brecciated zones (<1 m, termed "shear zones").

The outside surface of the spines may either be smooth *(Fig. 13b)*, or have a thin brecciated or vesicular rind *(Fig. 13d)*. Some spines appear to have extruded near-vertically *(Fig. 13a; Table 1)*, whereas a few spines seem to have initially extruded vertically but then drooped and folded to be pushed horizontally along the surface as a coherent mass. The difference between these spines and lava flows is that they are much denser and have shear zones on the outer edges. Similar features have been described at Soufriere Hills *(Watts et al. 2002)*.

Spines at Santiaguito are primarily dacite, with 64-66 wt.% SiO_2 *(Fig. 5; Rose 1972b; Avard and Whittington 2012; Scott et al. 2013)*. The phenocryst crystallinity is 27-33% *(Table 1)*, and the microlite crystallinity is 41.4-45.2% *(Fig. 6)*, giving a total crystallinity of 78.2%. As with the lava flows lower microlite crystallinities of 21.4-26.8% *(Fig. 6)* were measured by Scott et al. (2012) *(Fig. 6)*, indicating a possible range in total crystallinity of at 49-78%. Crystals are often aligned in the direction of extrusion.

The dense zones within the spines have low porosity (4-22.8%) *(Fig. 4)*, and the pores are similar in shape and size between samples. Most pores have ragged walls marked by the protrusion of phenocrysts and microlites. In thin section the pores reach a maximum of 5mm in diameter, however tomography *(Fig. 15)* and connected porosity data *(Fig. 4)* show that the pores form interconnected networks within the 10 mm sample size. Three distinct pore types can be identified; deflated interconnected pores, inflated interconnected pores and cavitation interconnected pores *(Fig. 14)*. The most common pore type is deflated

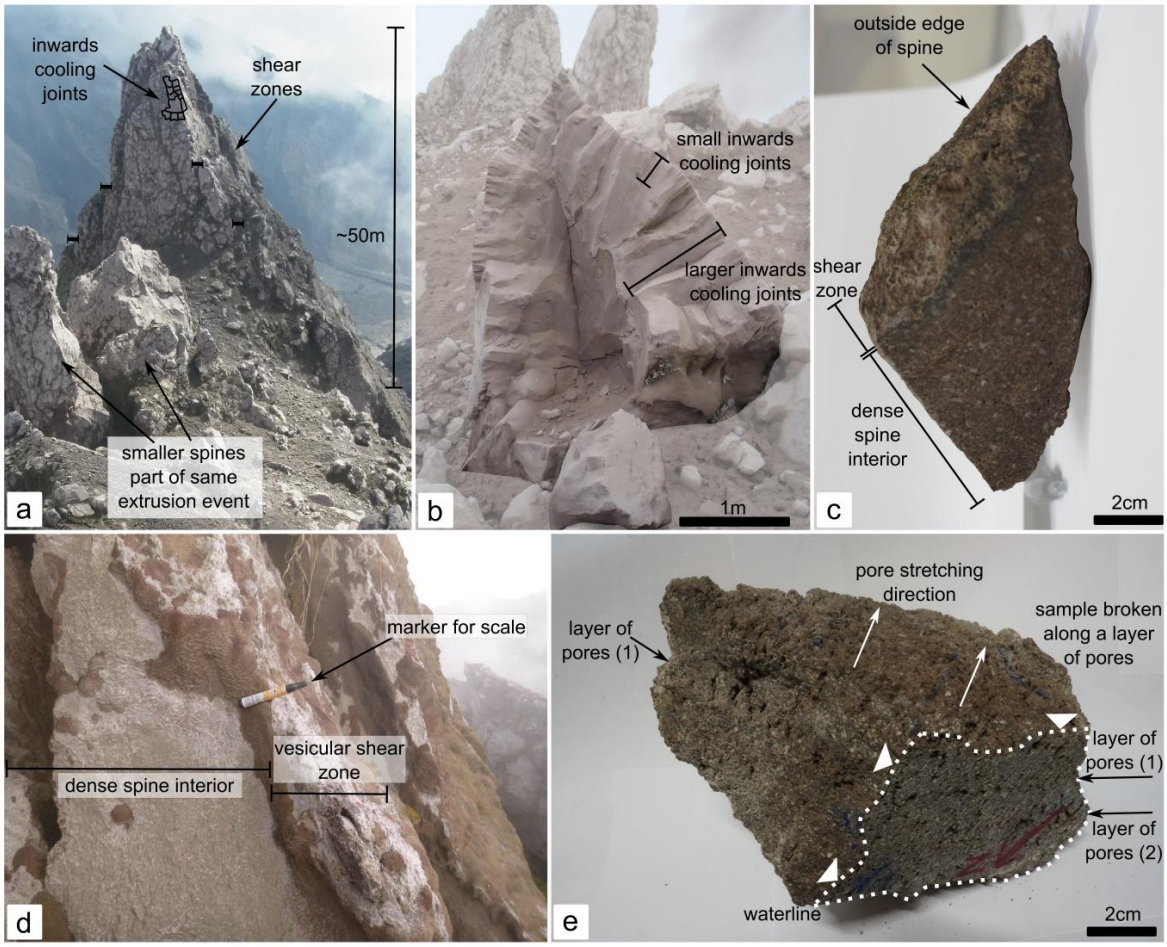

Figure 13. Photos of spines. (a) A large ridge forming spine and the position of shear zones within the spine, the shear zones were approximately 1 m width each and are separated laterally in the centre. The smaller spines in the foreground were also extruded at the same time as the large spine, together forming the distinct ridge on La Mitad. (b) Cross section of a small spine showing the inwards progression of cooling joints, both large sets and small sets. The outside appearance of these cooling joints can be seen in (a). (c) Hand sample showing a small cataclasite-type shear zone typical of the outside surface of a spine. (d) Outcrop of the edge of a spine, where the vesicular shear zone is exposed. (e) Sample of a vesicular shear zone, showing pore elongation and the bands of pores.

interconnected pores. These have both convex and concave pore surfaces, evidence of remnant bubble wall protrusion, and the largest examples always border phenocrysts *(Fig. 14 & 15).* Tomography shows that these pores form skeletal-like networks of interconnected pores that are aligned vertically *(Fig. 15)*. In contrast to the lava flows, the pore networks predominantly align in thin, tightly spaced vertical planes, with lesser lateral connectivity *(Fig. 15)*. Occasional convex surfaces, bulbous pores, and pore wall remnants characteristic of inflated interconnected pores are observed within the porous network, though are very

much subsidiary *(Fig. 14)*. Cavitation interconnected pores form along flow bands and in thin section show en-echelon bands with remnants of previously inflated or deflated interconnected pores *(Fig. 14)*. In thin section these pore chains reach a maximum of 2 mm in width, but the length of the chain often extends beyond the length of the 40 mm thin sections. The pore walls are extremely jagged and often border phenocrysts. Phenocrysts sometimes form islands in the middle of the bands. These localised bands are texturally similar to the shear zones described next.

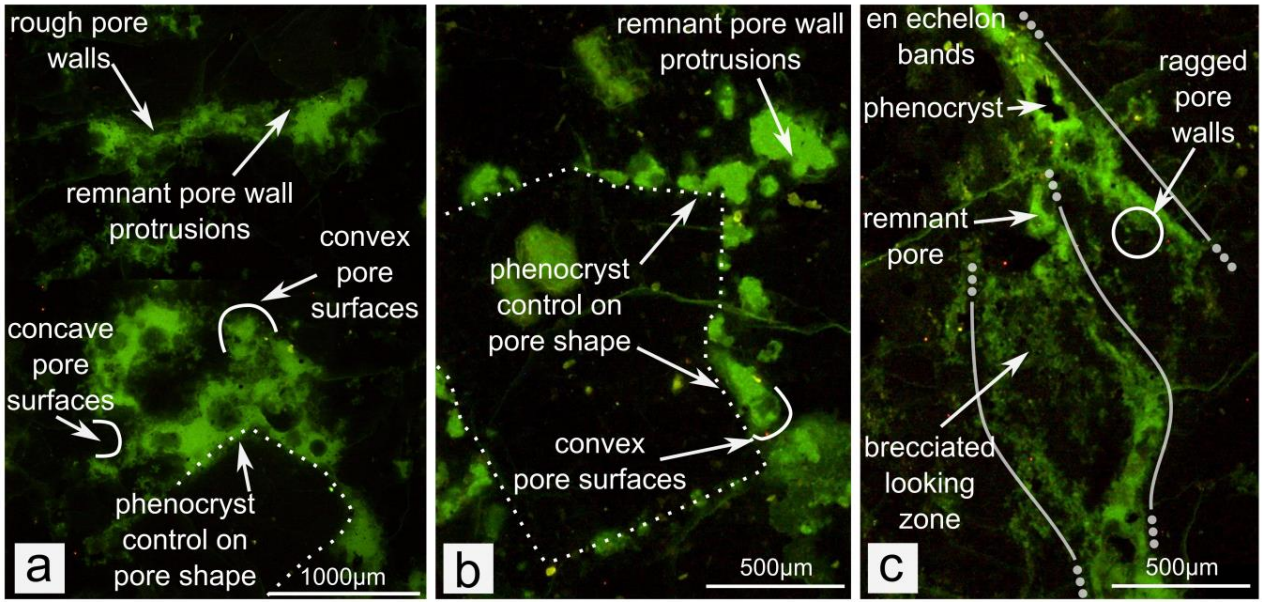

Figure 14. UV photomicrographs of pore in spines. Note: Pores are green. (a) Deflated interconnected pores, (b) inflated interconnected pores, and (c) flow band with cavitation interconnected pores.

Shear zones within the spines have a higher porosity (11.6-78.8%) *(Fig. 4)*, and are texturally variable. Highly vesicular zones are the most prominent type of shear zone. These shear zones are more vesicular (25-79% porosity *(Fig. 4)*) than the dense spine interior, and within the shear zones there are distinct sub-vertical sheets of larger pores *(Fig. 13e)*. The pores are elongated sub-vertically, up to 20° from vertical *(Fig. 13e)*. In thin section the pores reach a maximum of 10 mm in diameter, however tomography *(Fig. 17)* and connected porosity data *(Fig. 4)* show that the pores form interconnected networks within the 4 cm sample size. Tomography and thin section show the samples have an en-echelon pattern of inflated interconnected sigmoidal shaped pores *(Figs. 16; 17)*. I refer to these pores as "cavitation pores." Cavitation pores have convex and concave pore surfaces, evidence of remnant

bubble wall protrusion, and the largest examples always border phenocrysts *(Fig. 16)*. The pores may be large and widely spaced or thin and closely spaced *(Fig. 16)*. Stress tensors indicate up-down shear *(Fig. 17)*.

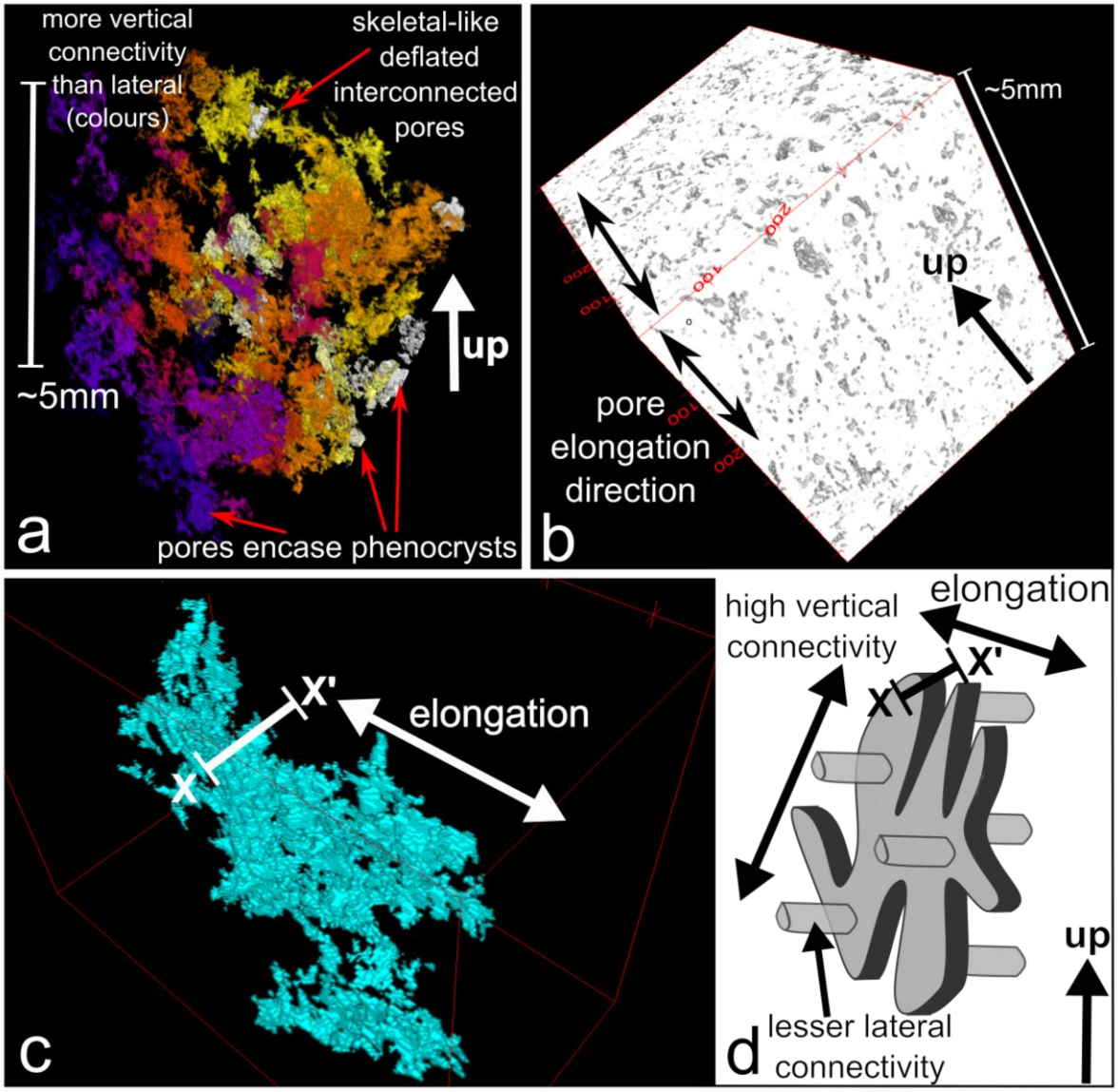

Figure 15. 3D tomography reconstructions of pores in spines. Each colour denotes an individual pore. As the sample is predominantly white (i.e. one colour), the porosity is largely connected. Note: only the largest 50 pores were reconstructed. The pores are all coloured, except for (b) where the pores are hollow. (a) Large scale image of pores. The colours (connected pores) show that pores have more vertical connectivity than horizontal. (b) Inverse image of (a) where the vertical pore alignment can be seen. (c) Singular pore. Note that even though these pores are deflated, they are plane-shaped rather than the tube-shaped deflated pores seen in the lava flows. (d) Simplified interpretation of the pores in spines. Refer to electronic appendix (a) (b) and (c) for 360° videos.

The densest shear zones (11-25% porosity) *(Fig. 4)* are thin (<2 cm) zones, where the porosity increases slightly and the crystal size decreases along the edge of the spine *(Fig. 14c)*. These shear zones appear partially brecciated, and are probably analogous to the cataclasite zones described at Mt St Helens *(Pallister et al. 2012)*. In one location, a third type of shear zone is marked by a coarse breccia. The breccia is non-welded, poorly sorted, clast supported, and contains dense angular clasts 1–30 mm in size.

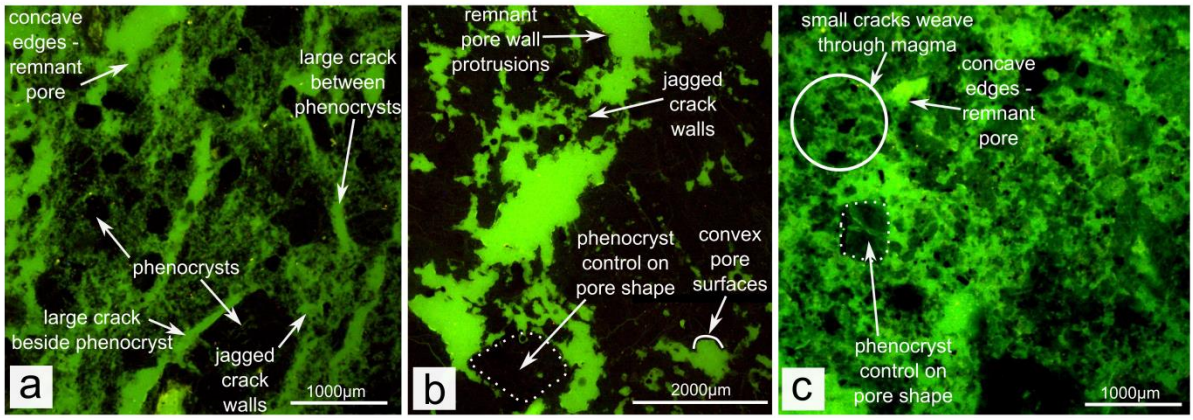

Figure 16. UV photomicrographs of shear Zones in Spines. *Note: pores are green.* (a) Vesicular shear zone with thin, closely spaced en echelon cavities and dominantly jagged pore walls. (b) Vesicular shear zone with thick en echelon cavities, and dominantly crisp pore walls with evidence of deflated or inflated pore walls. (c) Brecciated, cataclasite type shear zones. Note that compared to the vesicular shear zones, there is no clear pore elongation direction at this scale.

The biggest spines form the prominent ridges on La Mitad *(Fig. 14a)* and El Monje domes. These spines tend to have multiple widely spaced shear zones marked by more vesicular rinds at the edge of each dense core *(Fig. 14d)*. Commonly, a gap is observed between the two edges of the shear zones *(Fig. 14a)*. No evidence was observed to suggest these gaps were once filled with rubbly breccia, implying instead that the denser sections of the spines may have moved apart laterally at the weaker shear zones during extrusion. On a larger scale the major shear zones interweave, and when eroded out, there is a “petal-like” pattern of dense spine pieces in aerial view *(Electronic Appendix Map)*. The smallest spines are only 3 m by 5 m and instead of periodically spaced shear zones, these only have shear zones on either side.

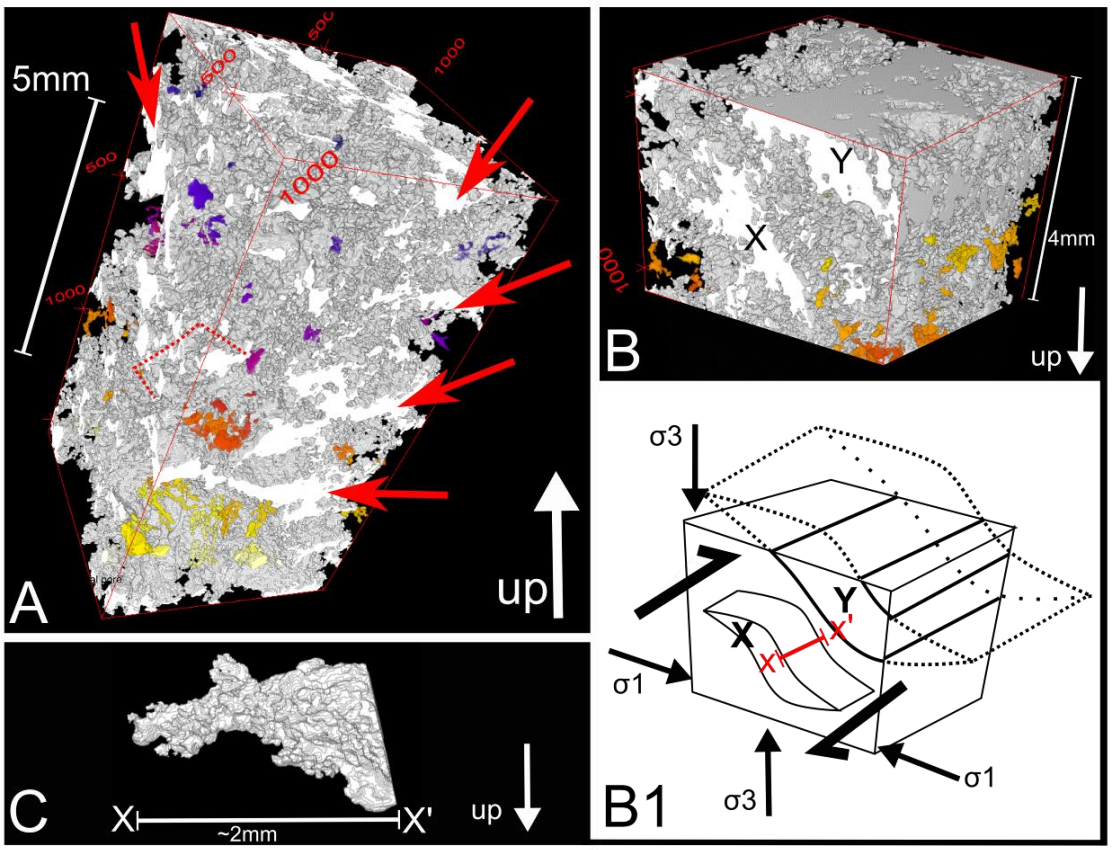

Figure 17. 3D tomography reconstructions of pores in Spine Shear Zones. Each colour denotes an individual pore. As the sample is predominantly white (i.e. one colour), it shows the porosity is largely connected. Note: only the largest 200 pores were reconstructed. (a) Large scale image showing the connected relationship between pores and the distinctive sigmoidal bands. (b) Intermediate scale image showing to sigmoidal bands (X and Y). Stress tensors calculated in 2D from the front face. (b1) Schematic interpretation of (b). (c) Side view of sigmoid X demonstrating how it pinches out into the sample (see (b), (b1)). Refer to electronic appendix (g) for a 360° video.

Cracks associated with brittle failure or cooling also form gaps within spines or spine edges *(Fig. 14a,b)*. These are termed cracks rather than shear zones because there is no evidence of a change in vesicularity, implying that they have formed via tensile fracturing of the cooling lava. Large cobweb like patterns of cracks, spaced 20-50 cm apart, are typically visible on the outer surface of spines *(Fig. 14a)*. These may be empty or filled with consolidated ash. Often when the interior of a spine is exposed, inwards cooling cracks, similar in appearance to small columnar joints are observed extending from the cobweb-like patterns on the outer surface to ~30 cm into the spine *(Fig. 14b)*. Therefore we interpret these cobweb cracks as cooling joints.

A timeline of extrusive activity at Santiaguito is presented in Figure 18. It shows that the extrusive facies are cyclical. A typical eruption cycle begins with extrusion of spines, often from a new vent. As the extrusion rate increases, lava flows of increasing length are emplaced. Towards the end of a cycle the extrusion rate declines again, and the trend is reversed culminating in spine growth. The next phase of activity typically resumes at a new location. Whereas for the earlier domes a single vent appears to have been dominant at any one time, visual observations have documented that at times there have been up to four active vents at Caliente *(e.g. April 1967; Rose 1973b)*. However deciphering vent migration at Caliente is difficult since earlier lavas have both been overprinted by subsequent extrusion, and also destroyed during explosive events *(Williams 1932)*.

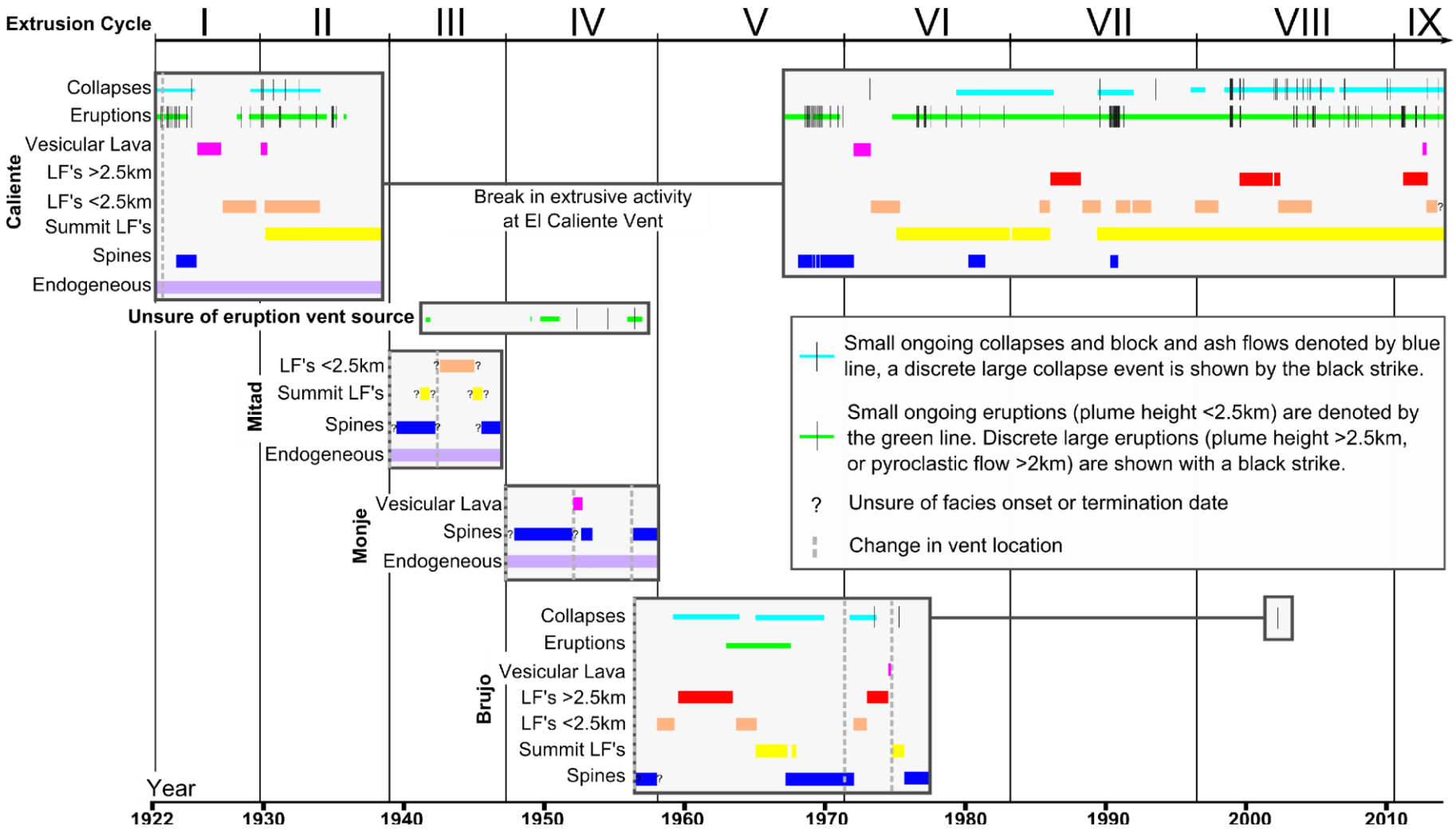

Figure. 18. Timing of activity at Santiaguito. Start and end date of extrusion cycles have been modified from Harris et al. (2003) to tie in with the start or end of vent migration. Note that eruption cycles are based on extrusion cycles based on extrusion rate calculations from Harris et al. (2003) rather than vent migration.

The key results from this study are:

- Spines have low porosity with thin zones of high porosity, whereas lava flows have a higher porosity in general, with a thick layer of even higher porosity beneath the top breccia.
- Pores in the high porosity lavas tops are generally interconnected convex coalesced bubble chains indicative of inflation, whereas pores in the denser lavas and spines contain more convex and concave surfaces controlled by crystals and deflation.
- The crystallinity and microlite contents of the facies are similar.
- The lava at Santiaguito has generally become more mafic and long blocky lava flows have become the dominant style.
- There are cycles in the extrusion style starting with spine growth, followed by lava flows of increasing length and ending again with spine growth. New spine growth often marks a shift in vent location.
- Large collapse events tend to be associated with long lava flow activity, and small collapses tend to be associated with spines.
- There is outcrop scale degassing evidence in the spine facies.

I next try to explain these trends and present an extrusion model for Santiaguito.

3 DISCUSSION

This study has revealed remarkable cycles in lava extrusion style. On lava domes worldwide, magma may extrude as a range of lava types, from flows to spines, depending on its viscosity, extrusion rate or the presence shear zones *(Corte et al. 2002; Watts et al. 2002; Pallister et al. 2012)*. Spines are generally more viscous *(Fink and Griffiths 1998)* than flows (10^7–10^{10} Pa s) *(Manley 1996; MacKay et al. 1998; Nakada et al. 1999; Harris et al. 2002; Navarro-Ochoa et al. 2002; Harris et al. 2004)*. Extrusion rates vary between spines and flows (e.g. spine extrusion rate of <1.7 m^3 s^- and a flow extrusion rate of 0.58-4.43 m^3 s^- at Unzen *(Nakada et al. 1999)*; and a spine extrusion rate of <5 m^3 s^- and flow extrusion rate of 5-9 m^3 s^- at Soufriere Hills *(Watts et al. 2002))* and shear zones develop in both spines and flows *(Holland et al. 2011; Pallister et al. 2012)*. However spines are associated with stick slip mechanisms and the development of discrete fault planes *(Pallister et al. 2012)* in contrast to wide auto breccias *(Harris et al. 2002)*. Feedback is inevitable between viscosity, extrusion rate and shear zone development and transitions between different flow types can occur as these controls variously interact.

Viscosity of lava domes is primarily controlled by the magma composition, crystallinity, temperature, water content and exsolved pores *(Giordano et al. 2008; Mueller et al. 2009; Mader et al. 2013)*. In this next section I explore the relative influence on the above factors on viscosity at Santiaguito.

The composition of the magma at Santiaguito has a broad control on the viscosity and eruption style of the lava. For example, spines only extruded when the magma was dacite, and lava flows over2.5 km length only occurred when more andesitic magma began to erupt *(Fig. 5; Harris et al. 2003)*. These differences are reflected in the change in the cyclic sequence of lava styles. In the early stages of dome growth spines extruded at low effusion rates and lava flows less than 2.5 km extruded at high effusion rates *(Fig. 18-cycles II, III)*. As the silica content decreased the length of lava flows extruded at high extrusion rates increased to over 2.5 km *(Fig. 18-cycles V-IX)*, and eventually spine extrusion was replaced by smaller summit lava flows at low extrusion rates *(Fig. 18-cycles VIII-IX)*. However, these cycles of lava style also demonstrate that rheological differences evolve within periods of constant magmatic composition *(Figs. 5; 18)*.

Degassing induced crystallisation is a model that is used to explain viscosity changes and lava style changes in other dome forming eruptions, e.g. Unzen, Mt St Helens and Soufriere Hills *(Nakada and Motomura 1999; Watts et al. 2002; Pallister et al. 2008)*. During many dome eruptions the extrusion rate is low enough that there is sufficient time in the conduit for microlite crystallisation. The relative rates of magma ascent during fast and slow extrusion periods are therefore reflected in the amount of microlite crystallisation prior to extrusion *(Nakada and Motomura 1999; Watts et al. 2002; Pallister et al. 2008)*. Microlite crystallisation is triggered by gas exsolution and this increases the viscosity of the magma in several ways: i) by enriching the melt in silica, ii) decreasing the water content of the melt, and iii) increasing particle-particle interaction. Consequently spines frequently have high microlite contents and more fluid lava types have lower microlite contents *(Nakada and Motomura 1999; Blundy and Cashman 2001; Watts et al. 2012)*.

Table 2. Comparison of the microlite content of Santiaguito to other domes, where the growth of microlites was considered to be an influence on eruption style and morphology.

	Phenocryst	**Microlites**	**Glass**	**Source**
Soufriere Hills lava	50%	20-30%	<30% (5-30%)	(Watts et al. 2002)
Soufriere Hills spines	50%	~60%	5-15%	(Watts et al. 2002)
Mt St Helens 2004-2006 spines	46% (±3)	14-42%	<10-30%	(Pallister et al. 2008)
Merapi spines and flows	~30%	40-50%	<30%	(Hammer et al. 2000)
Unzen lava	23-28%	30%	42-47%	(Nakada and Motomura 1999)
Unzen spines	23-28%	50%	22-27%	(Nakada and Motomura 1999)
Santiaguito spines and lava flows	~30%	~40%	~30%	*This study*

However, at Santiaguito there are only small changes in both the total crystallinity and the microlite crystallinity. The differences in microlite content between the lava types reported by both the sample set analysed by Scott et al. (2012) and in this study are <8% *(Fig. 6; Table 1)*, significantly less than the >20% differences in microlite crystallinity between lava flows and spines at Soufriere Hills and Unzen *(Table 2) (Nakada and Motomura 1999; Watts et al. 2002)*. In addition, other spines have low melt proportions of 5-30% (reflected by % glass in

samples), whereas the Santiaguito samples consistently have around 30% melt *(Table 2)*. Scott et al. (2012) hypothesised that this is because there is a "final quench" depth in the conduit where microlites stop nucleating and growing. The results from this study also agree with this hypothesis and suggest that neither changes in crystallinity or microlite growth are the primary causes of the viscosity difference between lava types at Santiaguito.

Instead, I present a combined outgassing and cooling model to explain the different extrusion styles at Santiaguito, dictated by extrusion rate and extrusion volume. The viscosity of the lava flows has been calculated through various studies to be approximately 10^9-10^{10} Pa s *(Table 3*: *Rose 1973a; Harris et al. 2002; Harris et al. 2004; Holland et al. 2011; Avard and Whittington 2012)*, and the spine viscosity must be inherently higher *(Fink and Griffiths 1998)*. Here I estimate the required amount of cooling or degree of degassing prior to eruption necessary to generate this viscosity difference.

Table 3. Viscosity of lava flows at Santiaguito.

Reference	Viscosity	Unit	Method
Harris et al. (2004)	$10^{9.6}$–$10^{10.8}$ Pa s	For the 1999-2002 lava flow	Bulk lava integrated value based on morphological properties of both the flow core and crust, using Jeffreys (1925).
Holland et al. (2011)	10^{11}–10^{14} Pa s	2009-2009 top of the conduit.	Joint textural and composition based value. The Giordano et al. (2008) model was used for melt viscosity and the effect of crystals added using Caricchi et al. (2007).
Harris et al. (2002)	0.4×10^{10} – 2.6×10^{10} Pa s	For the 1999-2002 lava flow	Bulk lava integrated value based on morphological properties of both the flow core and crust, following Cigolini et al. (1984).
Avard and Whittington (2012)	3.0×10^{10} – 7.2×10^{10} Pa s	2002 lava flow	Parallel Plate Viscometer
Rose (1973b)	5×10^{8}–9×10^{10} Pa s	1959-1961 lava flow	Bulk lava integrated value based on morphological properties and slope, following Nichols (1939).

The extrusion temperature of the lava flows at Santiaguito is considered to be 850–950 °C *(Table 4)*, but the extrusion temperature of the spines is unknown. Dacite spines worldwide have cooler extrusion temperatures of 730-780 °C *(Table 5)*. This is because in slow rising magma a thermal boundary layer develops at the conduit margins due to the cooling effect of the bordering country rock. At low extrusion rates (i.e. when spines were erupted at

Santiaguito) conduit marginal magma will spend more time in this thermal boundary layer, lowering the temperature locally by up to 200 °C *(Newman et al. 1988; Tuffen and Dingwell 2004; Collier and Neuberg 2006; Holland et al. 2011)*. Cooling will have more effect towards the top of the conduit as the thermal gradient increases. Crystallisation driven heating may occur in the conduit, balancing out the cooling. However, given the small differences in microlite crystallinity, and the hypothesis that there is a depth at which microlites stop crystallising in the conduit prior to extrusion *(Scott et al. 2012)*, I regard the effect of this heating as minor *(Blundy et al. 2006; Holland et al. 2011)*.

Table 4. Extrusion temperature at Santiaguito.

Reference	Temperature	Extrusive Unit and Method
Scott et al. (2012).	~900 °C	Matches amphibole rim widths and best represents geochemistry conditions at Santiaguito over its history.
Sahetapy-Engel (2004)	850–950 °C	Maximum temperatures measured at the surface of the El Caliente vent in 2002.
Scaillet et al. (1998)	833 °C (800-850 °C)	Fe-Ti oxide geothermometry on the Santa Maria pumice. Used method from Ghiorso and Sack (1991).
Harris et al. (2002)	800-850 °C	Eruption core temperatures from (Scaillet et al. 1998) are consistent with the measured flow font core temperatures of 573–683°Cof the 1999-2002 flow - calculated by a core cooling model.

Table 5. Extrusion temperature of spines at other domes.

Volcano	Unit and Method	Temperature	Reference
Mt St Helens (dacite)	Thermal Infrared Imaging of broken spine sections	500–730 °C	Schneider and Vallance (2008)
Unzen (dacite)	Various crystal phase relation relationships	780-880 °C Spines were on the lower limit of this range	(Nakada and Motomura 1999; Cordonnier et al. 2009)

Using glass compositions from Avard and Whittington (2012) and Scott et al. (2013) I calculated the melt viscosity using the method of Giordano et al. (2008) to demonstrate the effect that temperature has on melt viscosity. A 100 °C decrease in temperature from temperatures typical of lava flows to the temperatures of spines would cause an increase in viscosity by 2.1-2.2 orders of magnitude *(Fig. 19)*.

The amount of dissolved water in the melt during extrusion is unknown at Santiaguito due to a lack of sufficiently quenched glass or samples unaffected by secondary hydration. However approximate constraints on water contents can be estimated using examples from other domes and water solubility between 0 and 10 Mpa. The water solubility of rhyolite melt, such as at Santiaguito *(Avard and Whittington 2012; Scott et al. 2013)* is 0.02 wt.% at ambient pressure and 1.89 wt.% at 1km depth *(Papale et al. 2006; Holland et al. 2011)*. Water contents within lava domes worldwide vary between 0.1-1.2 wt.% *(Kusakabe et al. 1999; Gerlack et al. 2008)*. Measured water contents at Santiaguito vary between 0.03 and 0.19 wt.% *(Anderson et al. 1995)*. However, these do not necessarily reflect the water contents at the time of extrusion and are likely in approximate equilibrium with atmospheric conditions. Therefore, as an end member example we show that a drop in water content from 1 to 0 wt %, can increase the viscosity by 2.3 - 3.2 orders of magnitude *(Fig. 19)***.** Considering measured water contents, solubility constraints and examples from other domes worldwide I consider a likely scenario for Santiaguito to be 0.01- 0.5 wt % water variation, and this variation results in changes in viscosity of about 1 order of magnitude.

The dry apparent lava viscosity at Santiaguito measured by Avard and Whittington 2012 is $2.2 \times 10^{9} – 9.1 \times 10^{11}$ Pa s at 890-950 °C, and therefore accounting for the potential increases in viscosity due to cooling and degassing outlined above, spines viscosities at Santiaguito could reach ~ 10^{12}. A spine viscosity of 5×10^{12} is approximately consistent with estimates from experiments *(Avard and Whittington 2012).*

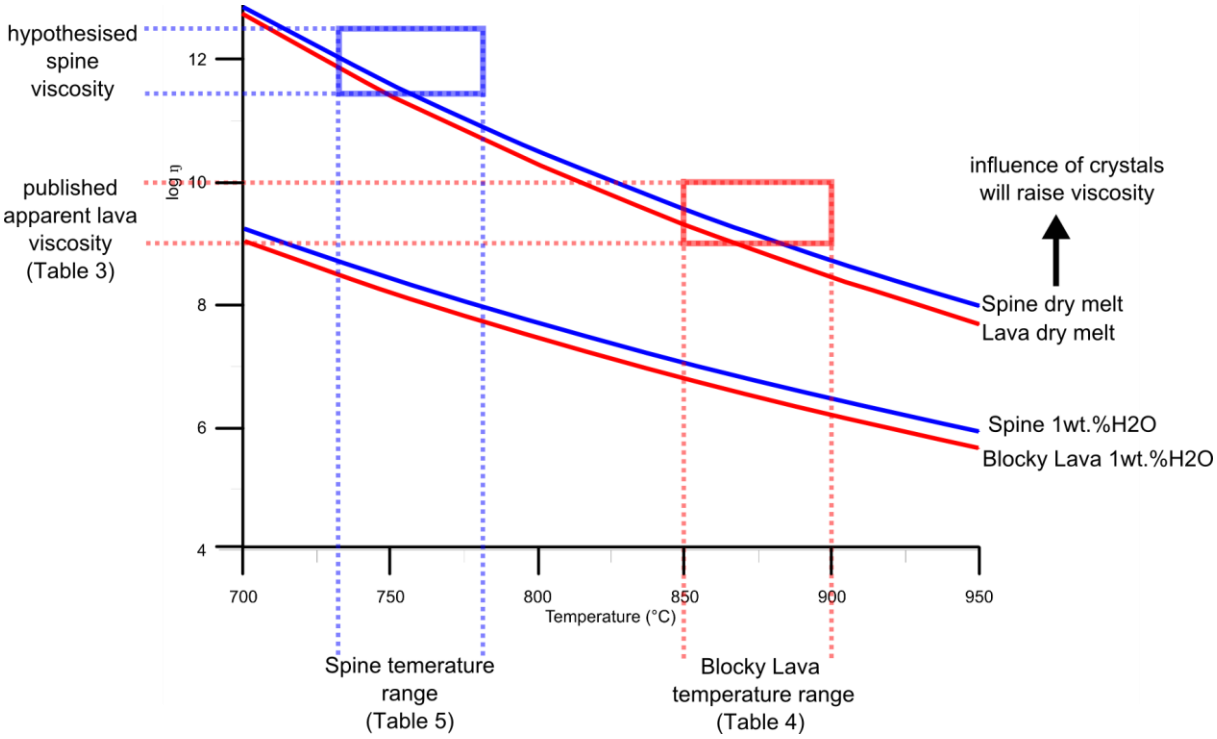

Figure 20. Melt viscosity calculated by Giordano (2008) and approximated apparent viscosities for spines and calculated apparent viscosities of spines.

The distinct variation in lava types at Santiaguito were all observed to occur within one dacitic extrusion cycle, without variation in melt composition or large changes in crystal content. Therefore these variations likely reflect temperature changes of approximately 50 °C and water content changes of between 0.1 and 0.5 wt.% water, reflecting typical variations in extrusion viscosity between $5x10^{10}$ and 10^{12} Pa s. Hotter andesitic lava may extrude at lower viscosities 10^{8-9} Pa s, which likely explains the lack of spines during periods of andesitic lava extrusion In the next section I discuss evidence for degassing and outgassing and temperature in the extruded facies at Santiaguito.

3.1 Degassing, outgassing and cooling in the conduit and during extrusion

The bubble contents and shapes record a history of degassing and outgassing in the lava types prior to, and after extrusion. I consider both historical observations and textural constraints to develop conceptual models of the relative timing of degassing, outgassing and cooling in the conduit and flow, to explain the variations in lava type.

Here I consider degassing as the shallow process of H_2O exsolving from the melt – typically forming bubbles (pores). Outgassing is the process of the exsolved volatiles escaping from the magma/lava, and requires a permeable pathway. A prerequisite for high viscosity effusive extrusion, i.e. lava dome formation, is the partial development of open system degassing. In an open system, gas is able to escape from the magma, reducing gas overpressure and decreasing the chance of explosive eruptions *(Cashman et al. 2000; Gonnermann and Manga 2007; Holland et al. 2011).*

Degassing in the conduit is controlled by the volatile overpressure and relevant solubility and equilibrium conditions permitting bubble nucleation and growth *(Cashman and Sparks 2013).* Outgassing of the bubbles is controlled by the openness of the magmatic system. Both degassing and outgassing are affected by the magma residence time in the shallow conduit. Residence time in the conduit is particularly important for magmas with high viscosities as a viscous magma takes longer to degass and to viscously open and close permeable pathways.

In high viscosity magma such as dacite, bubbles are considered more "trapped" than mobile, as the viscous forces dominate over the buoyant forces acting on the bubbles, promoting a coupled rise of melt and bubbles *(Sparks 2003)*. Where magma is not rising, stagnation may occur where a permeable magma foam *(Eichelberger et al. 1986; Jaupart and Allègre 1991; Rust and Cashman 2011)*, or cracked magma *(Gonnermann and Manga 2003; Tuffen et al. 2003; Collier and Neuberg 2006; Holland et al. 2011; Lavallée et al. 2013)* allows outgassing out into the surrounding country rock and the development of a partially or periodically open system *(Cashman and Sparks 2013)*. Evidence of continual outgassing and a periodically open system can both be observed at Santiaguito *(Stoiber and Rose 1969; Johnson 2004; Bluth and Rose 2004; Holland et al. 2011; Scharff et al. 2012; Ball et al. 2013).*

The extrusive products have whole rock water contents of 0.03-0.19 wt.%H_2O *(Anderson et al. 1995)*, which is consistent with the calculated ~0.1 wt.% H_2O saturation of rhyolite melts at ambient pressure *(Zhang et al. 2007)*. Although Santiaguito rocks are all dacites-andesites, the glass composition is rhyolitic *(Avard and Whittington 2012; Scott et al. 2012)*. The low dissolved water content therefore indicates that the melt reached H_2O equilibrium with the environment *(Anderson et al. 1995)*. In the magma chamber the approximate dissolved magmatic water content is 5-7 wt.% H_2O *(Scott et al. 2012)*, suggesting that at least 5 wt.%

H_2O has been exsolved from the melt prior to emplacement. Bubble textures can provide clues to this exsolution history of the magma.

Pore shapes, sizes and their relationship with crystal boundaries reflect the process of magma degassing and outgassing. Lava eruptions dominate the eruptive history of Santiaguito *(Fig. 18)*. The relatively open magmatic system and the slow rise of lava allows outgassing via interconnected pores, which are seen in all lava types. The high crystallinities of the Santiaguito lavas (~70% *(Table 1)*) mean pore shapes are controlled by crystals, producing irregularly shaped pores reflecting the inward protrusion of crystals into the pores. However, as the crystallinity does not vary by more than 5% *(Fig. 6)* in the samples in this study, the observed differences in pore shapes are nonetheless dominantly due to inflation, deflation, flattening or shearing.

Inflated interconnected pores have dominantly convex pore surfaces but also show concave remnant bubble wall protrusions from coalesced pores. Inflated interconnected pores frequently show no preferred network orientation *(Figs. 8; 9; 11; 12; 14)*. Deflated interconnected pores also have convex and concave pore surfaces, however remnant bubble wall protrusions are smoothed as decreasing gas pressure due to outgassing allows surface tension driven deformation *(Figs. 8; 9; 14; 15)*. In addition, inflated and deflated interconnected pores may have undergone a degree of flattening and stretching, indicating preferential compaction or shear *(Rust et al. 2003; Wright et al. 2006)*. Stretching of deflated pores results in a network of tube-shaped pores with a preferential alignment in lava flows *(Fig. 9)*, or skeletal shaped pore networks that are aligned along vertical planes in spines *(Fig. 15)*. Deflated pores are dominant in lower porosity spine and lava flow samples *(Figs. 9; 15)*. Flattening and stretching produces sheet like pores that form flow bands in the lavas *(Fig. 9)*. A distinct form of these flow bands with en-echelon sigmoidal pores within the inflated flow bands forms along spine margins *(Fig. 17)*. These are characteristic of cavitation where brittle failure of magma results in tension gashes that rotate into sigmoidal shapes and are influenced by phenocryst and remnant pore location *(Figs. 16; 17)*. Cavitation of dacite spines and lava flows has been recorded at Unzen, Yakedake and Daisen by Smith et al. (2001).

In the following section I propose a model for how the extrusion rate controls the amount of degassing and outgassing prior to extrusion, and how this is recorded in the pore structures of the different lava-types.

3.2 VESICULAR LAVA FLOWS

At Santiaguito vesicular lava flows lack a blocky carapace and are relatively small volume with a steep flow front *(Fig. 10)*. They have high porosity with dominantly inflated interconnected pores *(Figs. 11; 12; 21)*. The extrusion rate is unknown but I hypothesise that they are extruded at high extrusion rates or have a shorter conduit travel distance (e.g. due to opening of a new vent or partial collapse of an existing dome) and therefore a shorter travel time in the conduit prior to eruption *(Figs. 20; 21)*. This is inferred from pore textures, morphology and timing, and is consistent with research by Anderson and Fink (1990). Regardless of whether the extrusion rate is higher or the conduit length is shorter, these flows have spent the shortest time in the conduit prior to eruption and therefore extrude relatively hot *(Fig. 20-path i)*. The only vesicular lava flow whose emplacement was directly observed was emplaced following the November 28th 2012 partial lava and dome collapse *(Fig. 18)*. This was a short flow with what could be a scoriaceous top *(Fig. 10)*. Although no sample of this was able to be safely collected, morphologically this flow would classify as a vesicular lava.

Prior to and after the November 28th collapse there were no eruptions and lower levels of observable outgassing *(Fig. 10)*. These observations support the idea that higher extrusion rates and/or less degassed magma were present at the time the 2012 vesicular flow was emplaced. Absence of gas explosions can be linked to higher extrusion rates because there is less time for marginal cooling necessary for brittle failure along the conduit margins to initiate gas explosions *(Fig. 21; Holland et al. 2011)*.

Upon extrusion of the vesicular lavas, degassing continues at a rate faster than outgassing in order to preserve inflated interconnected pores when quenched *(Figs. 20-path I; 21)*. Shear upon movement aids the formation of thick (~5 mm) bands of inflated interconnected pores *(Figs. 11; 21)*. Compared to the long blocky lava flows *(Section 3.3)* shear heating is not as significant because of the short travel distances. However if the flow is long-lived (i.e.

extrusion continues) the initially vesicular lava flows may develop into blocky lava flows as further, degassing, outgassing, pore inflation and deflation occurs down flow *(Section 3.3) (Figs. 10; 21)*.

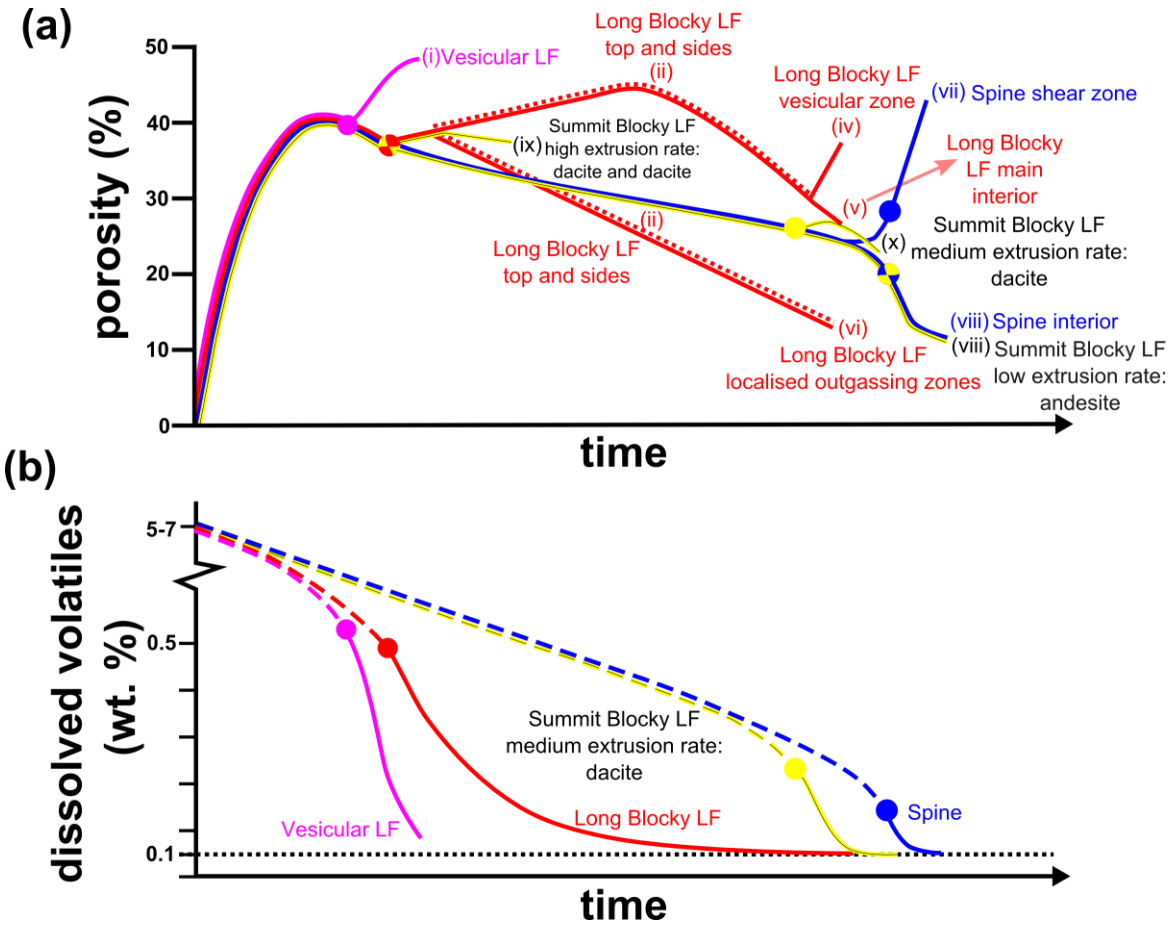

Figure 21. Conceptual models of pore growth and deflation based on porosity and pore textures. Origin represents the onset of volatile exsolution within the chamber or conduit. Circles shows at what stage/time the lava is erupted from the conduit for each lava type. The end of each line is the glass transition. (a) Evolution of pore growth and deflation in the different lava types, expressed through porosity. Increase in porosity represents degassing>outgassing, and a decrease in porosity represents outgassing > degassing. The exception to this rule is path (viii), where the pores are formed through cavitation. Purple line = vesicular lava flows, red line = long blocky lava flows, blue line = spines, yellow lines = the three different blocky summit flows. Red dashed line (ii) represents the blocky top and sides of the lava flows. (b) Estimated volatiles in the melt based on (a). Note: In this diagram, for the blocky summit flows, only the medium extrusion rate, dacite summit type is shown.

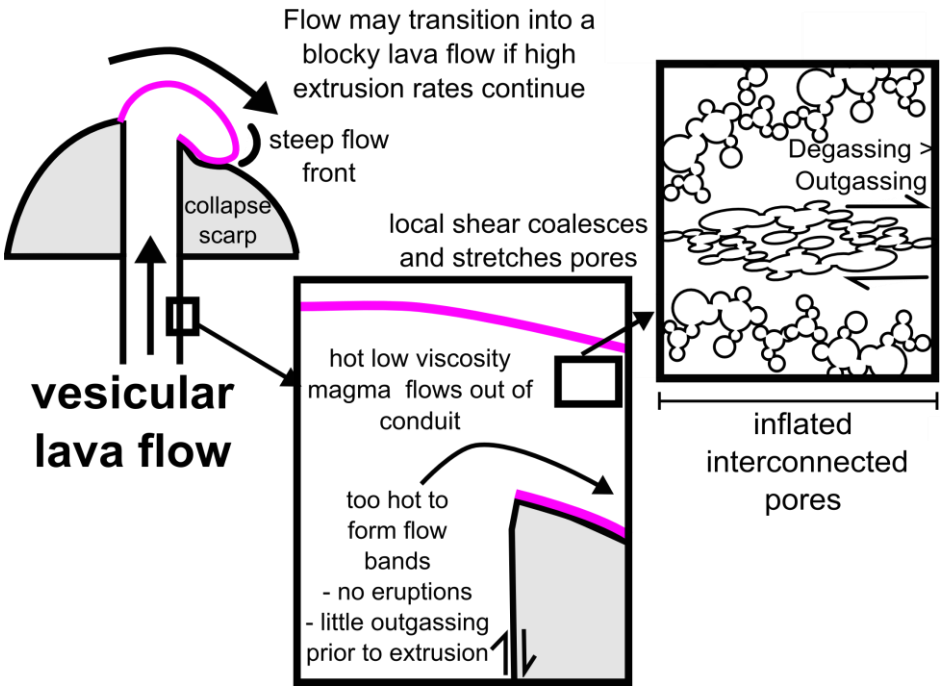

Figure 22. Schematic model of degassing and outgassing processes influencing the extrusion and pore textures of vesicular lava flows.

3.3 LONG BLOCKY LAVA FLOWS

A complex history of growth and deformation is recorded in the bubble textures preserved in the long blocky lava flows. Long blocky lava flows are also extruded at high extrusion rates (0.5-2.1 $m^3 s^-$)*(Harris et al. 2003)*, and they contain dominantly inflated pores *(Figs. 8; 9; 22)*. As with vesicular lava flows there is not enough time for complete degassing and outgassing prior to extrusion, but there is evidence that some outgassing occurs *(Fig. 20)*. Eruptions and fumerolic activity occur simultaneous with long blocky lava flow extrusion *(Figs. 1; 18; Rose 1973a; Johnson 2004; Bluth and Rose 2004; Brill 2011; Holland et al. 2011)*, and the explosions are bigger than during periods of summit flow extrusion *(Johnston, pers. comms. 2014)*.

Despite some outgassing, there must be some residual water content dissolved in the melt because after extrusion gas can be seen escaping from the lava flows, for at least a year after emplacement. In addition, there is further evidence for pressurized pores all the way to the flow fronts which can collapse to produce large mobile block and ash flows, e.g. from El Brujo and El Caliente in 1973 *(Fig. 18; Rose 1973b; Rose et al. 1976)*. Even though both lava flows (from Brujo and Caliente) had reached >2 km from vent when the block and ash flows

occurred, there were still enough pressurized volatiles to trigger block and ash flows flows that reached over 5 km from source. Additionally, loose material from both regular small and infrequent large long lava flow collapses accumulates in surrounding zone and drainage network. During the annual rainy season the loose material is remobilised as lahars that impact the fluvial system for 60 km to the pacific coast. The lahars are especially catastrophic when long lava flows, which provide lots of loose collapse material, enter the main drainage networks such as the Rio Tambor and Rio Nima I and II *(Fig. 3; Harris et al. 2006)*.

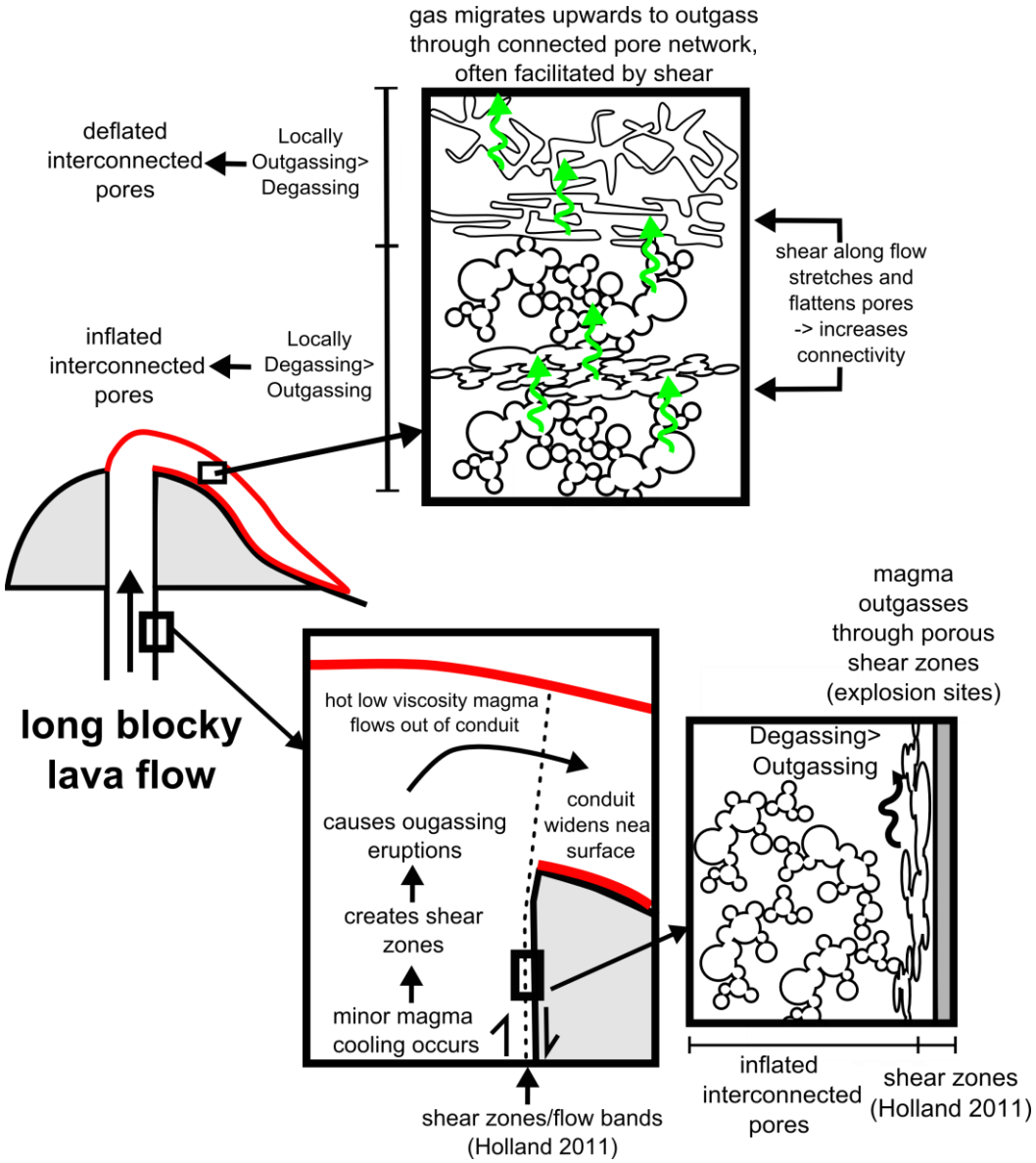

Figure 23. Schematic model of degassing and outgassing processes influencing the extrusion and pore textures of long blocky lava flows.

The high volume and long-lived nature of the long blocky lava flows means they can construct an insulated carapace to retain heat and facilitate shear heating in the flow centre, contributing to the long flow distances *(Harris et al. 2002; Avard and Whittington 2012)*. As a result, there is time for further pore inflation, pore migration, localised shear flattening, stretching and deflation post extrusion. These processes are reflected in the range of porosities and pore types found in the flows *(Figs. 4; 8; 9)*.

Initially, degassing occurs at a rate higher than outgassing forming inflated interconnected pores *(Fig. 22)*. These are dominantly preserved in the high porosity clasts and are found throughout the flow *(Fig. 20-path iv,v)*. Evidence of this initially porous flow is locally removed by subsequent deflation and shear along flow *(Fig. 22)*. Shear during flow stretches the pores, forming inflated interconnected pores with stretching *(Figs. 20-path iv,v; 22)*. Flattening may also occur from compaction. In localised areas, outgassing occurs at a rate higher than degassing, and pores shrink to become deflated interconnected pores *(Fig. 20-path vi)*. Deflated pores are generally stretched to form tube shaped networks, indicating outgassing is associated with local shear in the flow *(Fig. 22)*. Shear can facilitate outgassing and deflation by increasing the connectivity between pores, as was shown experimentally at strain rates representative of long blocky lava flows on Santiaguito samples by Avard and Whittington (2012). Pore deflation via outgassing increases with time during flow; this is reflected by decreases in the interior flow porosity down flow *(Fig. 20-paths iv,v)*. For example the Avard and Whittington (2012) samples collected 4 km from vent had a porosity of 3%, at least 9% lower than the lowest porosity sample collected in this study (max distance of 1 km from vent). However, as the samples are from different flows, this hypothesis requires further sampling and investigation.

Gas percolates through the permeable network towards the surface during flow creating layers of highly vesicular lava immediately below the blocky top *(Figs. 20-path iv; 22).* This process reduces porosity and deflates pores in the lava below *(Fig 22-path v)*. Pore migration might be aided by compaction *(Ashwell 2013)*. At any time during flow, segments of magma may be quenched at the flow front or edges, preserving a history of pore inflation, deflation and shear from different parts of the flow *(Fig. 20–path ii)*.

3.4 SPINES

A history of pore deflation and outgassing is recorded in the dense spine interiors with intermittent vesicular planar shear zones with large en-echelon sigmoidal pores *(Figs. 14; 15; 16; 17; 23)*. This evidence of outgassing leads to the inference that spines are extruded at low extrusion rates, and therefore are cooled and more degassed prior to extrusion *(Fig. 20)*.

At lower extrusion rates there is significantly more time for degassing and outgassing prior to extrusion *(Fig. 20)*. As outgassing occurs at a rate higher than degassing, initially inflated interconnected pores deflate to form thin networks of deflated interconnected pores, characteristic of the dense spine interior *(Figs. 14; 15; 23; 20)***.** Observations of outgassing and eruptions were scarce during spine extrusion, but mild steam eruptions did occur during the extrusion of spines at El Caliente *(Williams 1932; Rose 1973a)*. In addition, fumarolic activity has been ongoing throughout activity at Santiaguito *(Stoiber and Rose 1969; Stoiber and Rose 1970; Rose 1972b; Bluth and Rose 2004; Ball et al. 2013)*.

Upon extrusion the spines are already degassed *(Fig. 20)*. This degassing, in combination with cooling, increases the viscosity to a point where they are extruded as a semi-solid plug (10^{12} Pa s) rather than a flow ($10^{9\text{-}11}$Pa s) *(Figs. 19; 23)*.

Observations suggest that spine collapse has never triggered a block and ash flow large enough to be historically significant *(Fig. 18)*. This perhaps supports a lack of internal pore overpressure due to outgassing, cooler temperatures and small volumes. Quenching occurs soon after extrusion *(Fig. 20)*, as the spines are low volume and collapse regularly exposing fresh surfaces to cool. For these reasons there are no mechanisms for developing a carapace for heat conservation or time for shear heating to play a role.

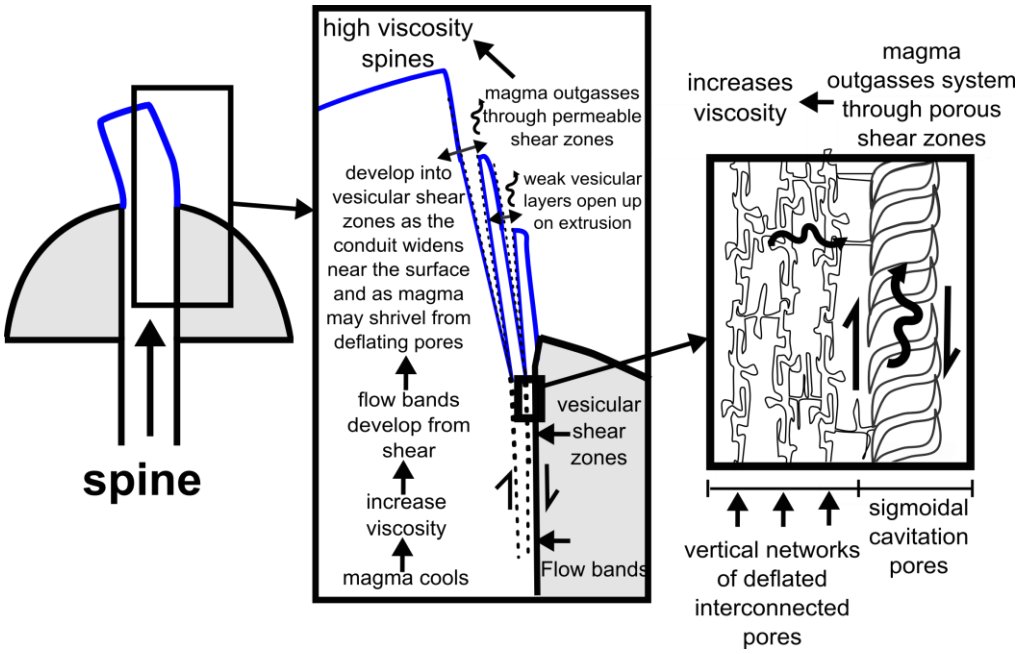

Figure 24. Schematic model of degassing and outgassing processes influencing the extrusion and pore textures of spines.

The vesicular layers in the spines contain inflated interconnected pores with en-echelon tension gashes *(Fig. 22),* and have similar properties to those described in the spine on top of Unzen in Smith et al. (2001). I interpret the vesicular layers at Santiaguito as a combination of; tensional brittle-ductile transition response to the decrease in confining stress at the top of the conduit/upon extrusion; and a focal point for strike-slip shear that occurs during the extrusion of the spines *(Figs. 20-path vii; 23)*. This interpretation is based on the oblique up-down alignment of cavitation-type pores within the vesicular zones (strike-slip) and the vertical higher porosity layers that form in the vesicular zones (tensional).

The failure criterion for magma is given by the relationship *(e.g. Goto 1999; Gonnermann and Manga 2003; Tuffen et al. 2003; Holland et al. 2011)*:

$$\gamma\eta > \tau_s \quad (1)$$

Where γ is the strain rate (s^{-}), η is the melt viscosity (Pa s) and τ_s is the shear strength of the melt (Pa).

Therefore if the viscosity increases, the tendency for the magma to brittlely fail increases. Decreasing compressional forces promote magma to fail in tension forming tension gash style cavities which are further sheared by continuing flow *(Fig. 23)*. Initially cavitation based flow bands will develop near the edge of the spine where shear is greatest and temperatures are closest to the glass transition temperature *(Figs. 20-path vii; 23)*. It is likely that these are a near-surface feature, as that is where the cooling is most pronounced. As the flow bands develop further (and are possibly held open by gas pore pressure) they connect to the surface, where they expand in width even further as the confining pressure decreases where the top of conduit widens *(Figs. 13; 23) (i.e. in the Bluth and Rose (2004) and Holland et al. (2011) models)*. In addition, outgassing from deflating pores means a net volume reduction in the spines, creating space for gas accumulation in these shear zones. It is likely that these vesicular shear bands form permeable pathways that facilitate outgassing, weak zones facilitating fault rupture *(Figs. 20; 23; Holland et al. 2011)*, and porous zones susceptible to fragmentation at low differential pressures *(Spieler et al. 2004)*.

3.5 SUMMIT BLOCKY LAVA FLOWS

Summit blocky lava flows are low volume flows, but have extruded at the full range of observed extrusion rates. I have subdivided the summit blocky lava flows into three classes, each with different outgassing histories and therefore viscosities. Unfortunately I only have a sample from one of the three types, but timing, morphological descriptions and observations constrain their formation.

Type 1. High extrusion rate, andesite and dacite. These summit flows occur simultaneously to long blocky lava flow extrusion *(Fig. 18-cycles II,VII, VIII, IX)*, and therefore have the same rheological properties and degassing/outgassing history at the long blocky lava flows *(Figs. 20-path ix; 22)*. However, their low volume means the flows both outgass and cool quicker, increasing their viscosity and consequently crossing the brittle-ductile transition sooner. Hence, they fail brittlely while still on the steep proximal flanks, thereby causing the flows to collapse from the flow front at a rate which prohibits them from reaching the base of the dome *(Fig. 20-path ix).*

Type 2. Medium extrusion rate, dacite. These summit flows extrude chronologically between long blocky lava flows and spines in the old vent dacite extrusion sequence

(section 3.8)*(Fig. 18-cycles III,V,VI).* A sample from a summit flow on La Mitad had a medium porosity of 24% and inflated and deflated pores with stretching. These flows are interpreted as representing an intermediate stage between the spine and long blocky lava flow end members. As they are extruded at a medium extrusion rate, they have undergone more cooling, degassing and outgassing than the long blocky lava flows *(Fig. 20-path x)*, but not yet enough to increase the viscosity to a point where shear zones develop and spines extrude. Therefore the conduit processes are similar to those of the long blocky lava flows *(Fig. 22)*.

Type 3. Low extrusion rate, andesite. Summit flows are the only kind of lava observed to have extruded during low effusion rates in andesitic magma *(Fig. 18-cycles VII-IX)*. No samples were acquired of this flow type, but Avard and Whittington (2012) reported a low porosity of 11%. This porosity indicates that they are more degassed and outgassed and therefore extruded at similar extrusion rates to spines, and as a result may be cooler than the other andesitic lava flow types *(Fig. 20-path viii; Harris et al. 2003)*. In terms of conduit-level degassing, outgassing and extrusion rate, these are equivalent to the lava spines, but the lower viscosity andesitic magma means they are emplaced as lava flows. The ascending magma and subsequent lava degass efficiently due both to brecciation and shear zone development.

3.6 Model

The new classification of lava flow types and their sequencing within the eruption timeline identify three distinct types of ycle: New vent cycle, old vent dacite cycle and old vent andesite cycle. The cycle style is dependent on the initial composition, and the degassing and outgassing history of the magma. The eruptive sequence within each cycle is then controlled by the effusion rate.

3.7 New Vent Cycle

This cycle is initially characterised by endogenous growth of moderately viscous undegassed dacitic magma *(Fig. 24)*. Cycles I, III and IV were new vent cycles *(Fig. 18)*. The young endogenous dome is inherently less permeable than older established domes. Vesicular magma inflates inside the dome during an early high extrusion rate phase *(Fig. 24)*. Local

leaks from the dominantly endogenously growing dome extrude vesicular lavas and small spines. This is shown in Cycles I, III and IV and their extrusion is associated with fumeroles, fissuring and explosions *(Figs. 18; 24-path A)*. Vesicular lavas and small spines are demonstrative of a transitional stage between endogenous growth and exogenous main spine growth *(Fig. 23-paths A-B)*. Vesicular breakout lavas are representative of the undegassed magma that feeds endogenous dome growth. Subsequent localised outgassing here outweighing degassing, and localised low extrusion rates in the still-dominantly endogenous dome, increase viscosity and cause extrusion of small spines *(Fig. 23)*. A preserved example for this could be unit Rma on El Monje, where two low volume vesicular lava flows possibly representative of small-scale breakouts from the undegassed endogenous dome transitioned into low volume spines in Cycle *IV (Figs. 3, 18-cycle IV vent 2)*.

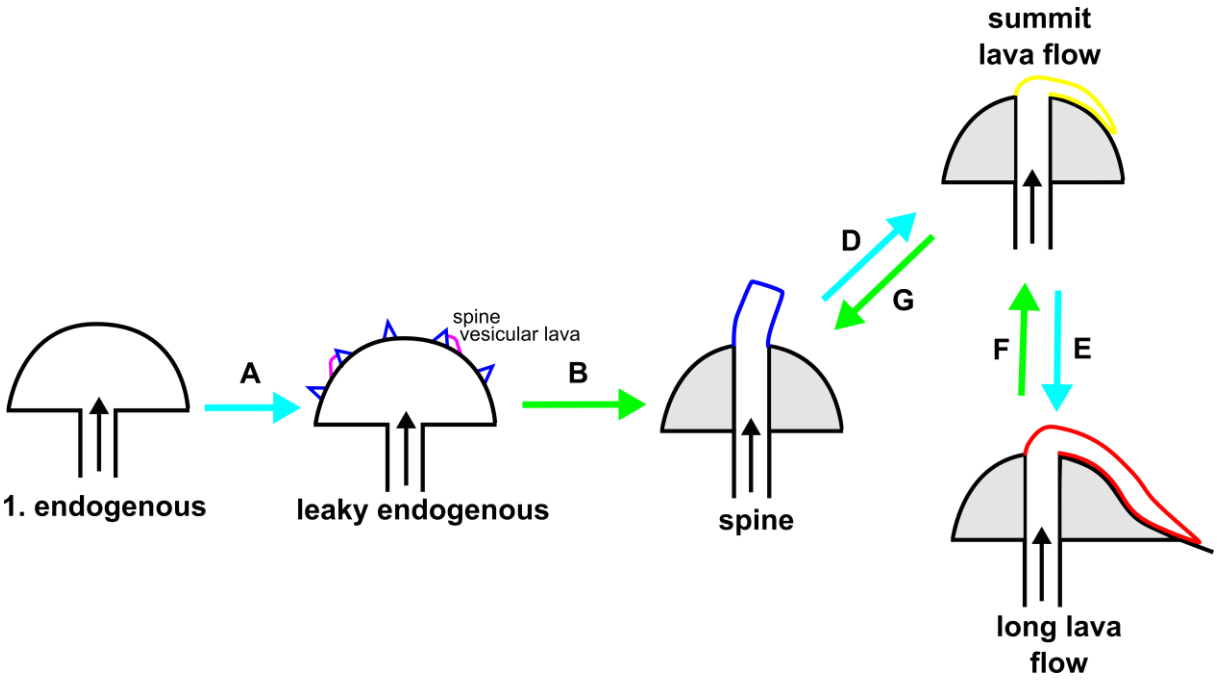

Figure 25. New vent cycle. Blue arrows denote an increase in extrusion rate, green arrows a decrease in extrusion rate.

Following development of a main extrusive vent (i.e. transition to exogenous growth) at a previously "leaky" endogenous dome, spines then dominate extrusion and the extrusion rate at the new vent is slow *(Fig. 24-path B)*. This occurs in Cycles I, III and IV *(Fig. 18)*. Here rising magma degasses and rapid outgassing increases viscosity and causes pores to deflate and porous shear zones with en-echelon cavities to develop *(Fig. 23)*. These porous zones further

facilitate fumerolic outgassing and explosions *(Spieler et al. 2004).* If effusion rates decrease at this stage, such as in Cycles I and IV *(Fig. 18)*, spine extrusion will be the final extrusive product.

If effusion rates increase, the eruptive style can transition into blocky lava flows of increasing length, such as in Cycle III *(Fig. 18; 24-path D-E).* If a blocky lava flow occurs, localised shear zones develop in the conduit and in the flow itself. However the higher effusion rate and therefore shorter conduit residence time allows only limited outgassing of the initially vesicular magma prior to extrusion *(Holland et al. 2011). C*ontinued degassing upon extrusion results in a flow banded lava with alternating inflated and deflated layers of interconnected pores *(Fig. 22)*. The increased porosity of the inflated shear bands favours the shear bands as sites for gas explosions *(Fig. 22; Spieler et al. 2004; Holland et al. 2011)*. Blocky lava flows are synchronous with gas explosions *(Fig. 18; Bluth and Rose 2004; Johnson et al. 2008; Holland et al. 2011)* and vary in length with effusion rate and duration *(Fig. 24-paths E-F).* During Cycle III on La Mitad, the period of lava flow extrusion initiated from a new vent on the same dome, probably because it was easier to form a new vent than to further extrude the previous spine *(Watts et al. 2002).* The extrusion cycle then ends with decreasing extrusion rates feeding lava flows of decreasing length *(Fig. 18, 24-path F)*, and finally reverting to viscous cooler degassed spines *(Fig. 24-path G)* as extrusion rates decreased further.

At any stage local increases in extrusion rate can cause lava to over-steepen and trigger collapses from both flow toes and the summit zone, resulting in block and ash flows. However there were no reports of major events that changed the extrusion style *(Fig. 18)*.

3.8 Old Vent Dacite Cycle

The old vent dacite cycle is initially characterised by extrusion of viscous degassed dacitic magma leftover from the previous eruption cycle *(Figs. 23; 25)*. Cycles II, V and VI were old vent dacite cycles *(Fig. 18)*. The magma is degassed because it has been stagnating in the conduit with pre-established permeable pathways. The old vent is blocked by the cool dense viscous lava previously extruded at the end of the last cycle, and therefore the new extrusion cycle initiates at a new vent adjacent to the old vent *(Fig. 25)*. Although the onset

of extrusion Cycle V at El Brujo occurred at a new dome, it has been classified as an old vent dacite cycle because no endogenous growth accompanied dome extrusion *(Harris et al. 2003)* and the spines at the start of the cycle may be associated with previous spine growth at El Monje (observations are scarce) *(Fig. 18)*.

As the extrusion rate increases, less degassed, hotter, less viscous magma is extruded transitioning into blocky lava flows of increasing length, such as in Cycles V and VI *(Figs. 18; 25-path A-B)*. When the extrusion rate then decreases at the end of the extrusion cycle, outgassing again outweighs degassing, and spines are once more extruded (Cycles V and VI) *(Figs. 18; 25-path C-D)*. Cycle II however ended with summit blocky lava flow extrusion.

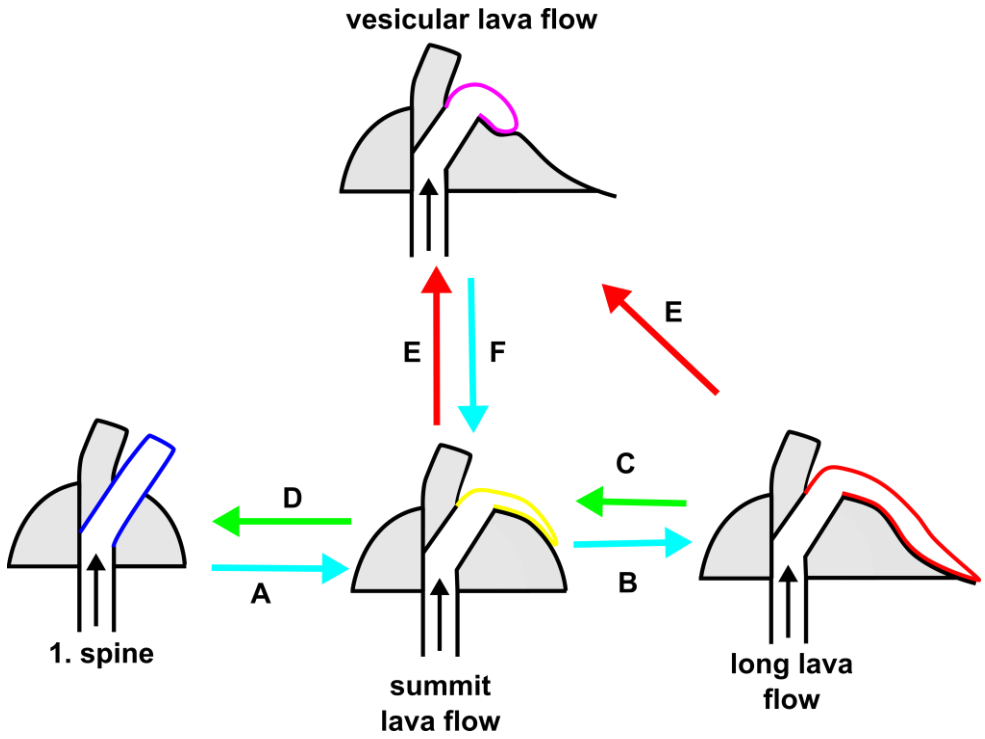

Figure 26. Old vent dacite cycle. Blue arrows denote an increase in extrusion rate, green arrows a decrease in extrusion rate and red arrows a collapse.

Similarly to the new vent cycle, at any stage local increases in extrusion rate can cause larger explosions or trigger collapses, from either flow toes or the summit zone. Cycle II shows that following the catastrophic explosion and collapse of El Caliente in 1929, removal of overburden decompresses the lava inducing catastrophic outgassing and additional degassing and the extrusion of vesicular lava *(Figs. 18; 21; 25-path E)*. However; with

continued extrusion these vesicular lava flows will transition into blocky lava flows, as occurred after the 1929 collapse *(Figs. 18; 25-path F&B).* The vesicular lava flow *(Fig. 3)* preserved on El Brujo occurred after the extrusion of a long blocky lava flow, and fills a crater; this flow probably also formed following a collapse or explosion in response to decompression and was preserved because the vent then migrated *(Fig. 18)*.

3.9 Old Vent Andesite cycle:

The old vent andesite cycle is characterised by initially low viscosity, partially to well-degassed andesitic magma erupting from an established summit vent *(Fig. 26)*. Cycles VII, VIII and IX are old vent andesite cycles *(Fig. 18)*. In these cycles, summit flows are initially extruded *(Fig. 18)*. The first summit lavas to erupt may be more vesicular, but evidence for this is subsequently destroyed down flow due to continued outgassing *(Fig. 26-path A)*. In contrast to the dacite cycles, the andesite cycles did not extrude spines because the starting viscosity was lower *(Harris et al. 2003)*. As the effusion rate increased, *(Fig. 26-path B)* progressively less time was available for degassing and cooling in the conduit, and lava flows increased in length *(Figs. 18; 20)*. The very longest lava flows to extrude (Rma, Rcl *(Fig. 3)*) were both extruded during andesite cycles; therefore, their long length may also be a consequence of the lower viscosity in addition to the high extrusion rates.

Effusion rates also vary spatially, and shorter lava flows and summit flows are extruded simultaneously to the longer flows *(See Cycles VI, VIII and XI: Fig. 18)*. Cycle VII has been classified as an andesitic cycle despite spine extrusion in 1989 because the spine extrusion was short-lived, and the start and end of the extrusion cycle was characterised by summit lava flows *(Fig. 18)*. This is consistent because in terms of time *(Fig. 18)* and composition *(Fig. 5)* this cycle is a transitional member between the dacite and andesite cycles.

Similarly to the other cycles, at any stage collapses from the summit zone can cause a transition back to vesicular lava *(Fig. 26- path D),* e.g. as seen after the November 28th 2012 collapse, and the extrusion rate post-collapse then determines the next lava type to extrude *(Fig. 26 A&B)*.

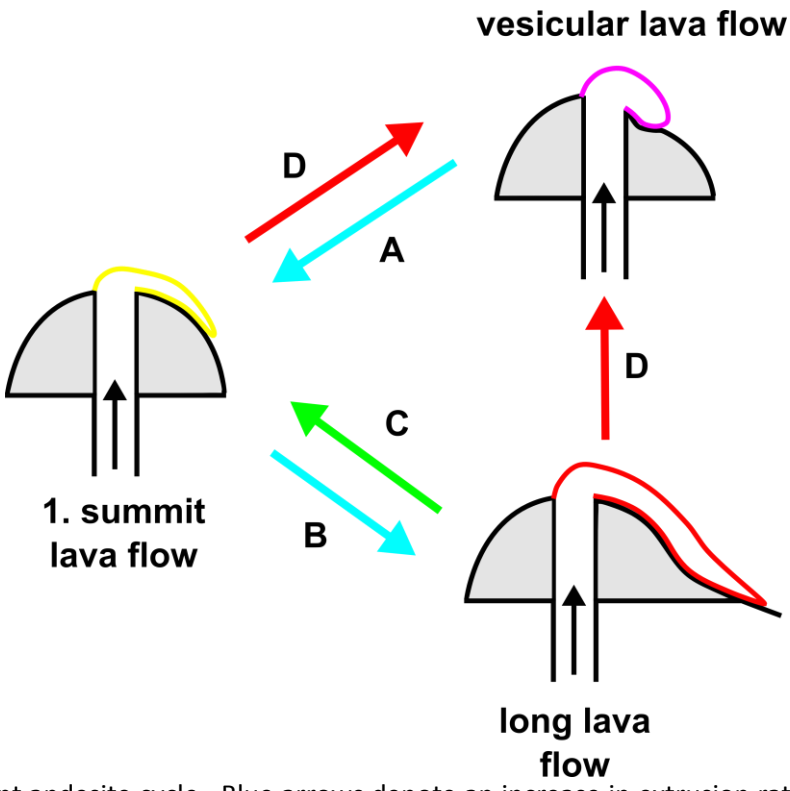

Figure 27. Old vent andesite cycle. Blue arrows denote an increase in extrusion rate, green arrows a decrease in extrusion rate and red arrows a collapse.

4 CONCLUSION AND IMPLICATIONS

Here I combine new mapping, textural data and viscosity modelling with existing geochemical data, eruption observations and experiments to develop a model of lava flow extrusion style at Santiaguito. The model demonstrates the importance of effusion rate, degassing and outgassing, and hence viscosity, in controlling the eruption style and associated lava types. My conclusions can be summarised as follows.

1. There are four main lava types at Santiaguito; vesicular lava flows, long blocky lava flows, Summit blocky lava flows, and Spines. These types reveal a progression from porous long lava flows with inflated pores to spines with deflated pores and well developed porous shear bands. There is no significant change in crystal content. All lava types were found on each of the domes, apart from La Mitad where no vesicular lava flow was preserved or El Monje where no long lava flow extrusion occurred.

2. Distinct eruption cycles are identified, which are primarily controlled by the initial composition, effusion rate, and the degassing/outgassing history of the magma. The degassing and outgassing history of the magma is preserved in pore textures in lava samples, and reflects both in-conduit and post-extrusion processes. Effusion rate exerts a major control on in-conduit degassing and outgassing, and hence is a key factor controlling eruption style at Santiaguito.

3. The sequence of lava types varies in each distinctive eruption cycle, and is dominantly explained by temporal changes in effusion rate and instantaneous dome summit collapses.

4. Effusion rate and duration defines the amount of time available for cooling, degassing and outgassing prior to and during extrusion, driving changes in pore textures, and ultimately viscosity.

5. Dome or lava-flow collapses can occur at any stage, triggered by lava flow front oversteepening or increases in extrusion rate. Major collapses typically cause a shift in eruption style to vesicular lava flows.

6. There is an association of hazardous block and ash flows with the collapse of long hot lava flows during periods of high extrusion rate. The largest recorded events travelled more than 5km from the lava flow fronts, representing a significant hazard. Additionally, since long blocky lava flows extend into the headwaters of major drainages, abundant unconsolidated material from frequent smaller flow-front collapses results in a significant annual lahar hazard downstream

This understanding of how outgassing and degassing influence the styles and sequences of lava flows has important implications for hazard recognition at lava domes worldwide.

5 FUTURE WORK

- Further sampling of the various summit lava flow types to constrain their pore types and formation
- Research into cavitation processes in highly crystalline, highly viscous magma.
- Formation and permeability of the shear zones
- Permeability of shear zones to calculate their contribution to degassing in spines
- More comprehensive extrusion rate calculations using GIS technology and/or 3D modelling.

6 REFERENCE LIST

Anderson SW, Fink JH (1990) The development and distribution of surface textures at the Mt St. Helens dome. In: Fink JH (ed) Lava Flows and Domes: Emplacement Mechanisms and Hazard Implications. IAVCEI Proceedings in Volcanology, 2. Springer-Verlag, Berlin., pp 25–46

Anderson SW, Fink JH, Rose WI (1995) Mount St. Helens and Santiaguito lava domes: The effect of short-term eruption rate on surface texture and degassing processes. Journal of Volcanology and Geothermal Research 69:105–116.

Andres R, Rose WI (1995) Description of thermal anomalies on two active Guatemalan volcanoes using Landsat Thematic Mapper imagery. Photogrammetric Engineering and Remote Sensing 61:775–782.

Ashwell PA (2013) Eruption styles, structures and controls at rhyolitic lava domes. 1–220. University of Canterbury.

Avard G, Whittington AG (2012) Rheology of arc dacite lavas: experimental determination at low strain rates. Bulletin of Volcanology 74:1039–1056.

Ball JL, Calder ES, Hubbard BE, Bernstein ML (2013) An assessment of hydrothermal alteration in the Santiaguito lava dome complex, Guatemala: implications for dome collapse hazards. Bulletin of Volcanology 75:676.

Bennati L, Finizola A, Walker JA, et al. (2011) Fluid circulation in a complex volcano-tectonic setting, inferred from self-potential and soil CO2 flux surveys: The Santa María–Cerro Quemado–Zunil volcanoes and Xela caldera (Northwestern Guatemala). Journal of Volcanology and Geothermal Research 199:216–229.

Blundy J, Cashman K (2001) Ascent-driven crystallisation of dacite magmas at Mount St Helens, 1980–1986. Contributions to Mineralogy and Petrology 140:631–650.

Blundy J, Cashman K, Humphreys M (2006) Magma heating by decompression-driven crystallization beneath andesite volcanoes. Nature 37:261–271.

Bluth GJS, Rose WI (2004) Observations of eruptive activity at Santiaguito volcano, Guatemala. Journal of Volcanology and Geothermal Research 136:297–302.

Brill KA (2011) Characterization of harmonic tremor at Santiaguito Volcano and its implications for eruption mechanisms. Dissertation, Michigan Technological University.

Bull KF, Buurman H (2013) An overview of the 2009 eruption of Redoubt Volcano, Alaska. Journal of Volcanology and Geothermal Research 259:2–15.

Caricchi L, Burlini L, Ulmer P, et al. (2007) Non-Newtonian rheology of crystal-bearing magmas and implications for magma ascent dynamics. Earth and Planetary Science Letters 264:402–419.

Cashman K (1992) Groundmass crystallization of Mount St. Helens dacite, 1980-1986: a tool for interpreting shallow magmatic processes. Contributions to Mineralogy and Petrology 109:431–449.

Cashman KV, Sparks RSJ (2013) How volcanoes work: A 25 year perspective. Geological Society of America Bulletin 125:664–690.

Cashman KV, Sturtevant B, Papale P, Navon O (2000) Magmatic Fragmentation. In: Sigurdsson H, Houghton B, Rymer H, et al. (eds) Encyclopedia of Volcanoes. Academic Press, Waltham, Massachusetts, pp 421–430

Cigolini C, Borgia A, Casertano L (1984) Intra-crater activity, A'a-Block lava, viscosity and flow dynamics: Arenal Volcano, Costa Rica. Journal of Volcanology and Geothermal Research 20:155–176.

Cole PD, Calder ES, Druitt TH, et al. (1998) Pyroclastic flows generated by gravitational instability of the 1996-97 Lava Dome of Soufriere Hills Volcano, Montserrat. Geophysical Research Letters 25:3425–3428.

Collier L, Neuberg J (2006) Incorporating seismic observations into 2D conduit flow modeling. Journal of Volcanology and Geothermal Research 152:331–346.

Conway FM, Diehl JF, Rose WI, et al. (2013) Age and magma flux of Santa Maria Volcano, Guatemala: Correlation of paleomagnetic waveforms with the 28,000 to 25,000 yr B.P. Mono Lake excursion. The Journal of Geology 102:11–24.

Cordonnier B, Hess K-U, Lavallee Y, Dingwell DB (2009) Rheological properties of dome lavas: Case study of Unzen volcano. Earth and Planetary Science Letters 279:263–272.

Corte A, Galindo I, Gavilanes JC, et al. (2002) Overview of the 1997-2000 activity of Volcán de Colima, México. Journal of Volcanology and Geothermal Research 117:1–19.

Duffield W, Heiken G, Foley D, McEwen A (1993) Oblique synoptic images, produced from digital data, display strong evidence of a "new" caldera in southwestern Guatemala. Journal of Volcanology and Geothermal Research 55:217–224.

Ebmeier SK, Biggs J, Mather TA, et al. (2012) Measuring large topographic change with InSAR: Lava thicknesses, extrusion rate and subsidence rate at Santiaguito volcano, Guatemala. Earth and Planetary Science Letters 335-336:216–225.

Eichelberger JC, Carrigan CR, Westrich HR, Price RH (1986) Non-explosive silicic volcanism. Nature 323:598–602.

Escobar-Wolf R, Matias Gomez RO, Rose WI (2010) Geologic map of Santiaguito volcano, Guatemala. Geological Society of America Digital Map Chart Series 8:

Fink JH, Griffiths RW (1998) Morphology, eruption rates, and rheology of lava domes: Insights from laboratory models. Journal of Geophysical Research 103:527–545.

Fink JH, Malin MC, Anderson SW (1990) Intrusive and extrusive growth of the Mount St Helens lava dome. Nature 348:435–437.

Forbes CC (2010) Surficial behavior of lava extruded by Santiaguito Dome, Guatemala, during January 2007 and January 2009. Dissertation, New Mexico Institute of Mining and Technology.

Gerlack T, Mcgee K, Doukas M (2008) Emission rates of CO2, SO2, and H2S, scrubbing, and preeruption excess volatiles at Mount St. Helens, 2004-2005. US Geological Survey Professional Paper 1750:108–120.

Ghiorso MS, Sack RO (1991) Mineralogy and Fe-Ti oxide geothermometry: thermodynamic formulation and the estimation of intensive variables in silicic magmas. Contributions to Mineralogy and Petrology 108:485–510.

Giordano D, Russell JK, Dingwell DB (2008) Viscosity of magmatic liquids: A model. Earth and Planetary Science Letters 271:123–134.

Gonnermann H, Manga M (2003) Explosive volcanism may not be an inevitable consequence of magma fragmentation. Nature 37–41.

Gonnermann HM, Manga M (2007) The Fluid Mechanics Inside a Volcano. Annual Review of Fluid Mechanics 39:321–356.

Goto A (1999) A new model for volcanic earthquake at Unzen Volcano: Melt rupture model. Geophysical Research Letters 30:117–130.

Hale AJ, Wadge G (2008) The transition from endogenous to exogenous growth of lava domes with the development of shear bands. Journal of Volcanology and Geothermal Research 171:237–257.

Hammer JE, Cashman KV, Voight B (2000) Magmatic processes revealed by textural and compositional trends in Merapi dome lavas. Journal of Volcanology and Geothermal Research 100:165–192.

Hammer JE, Rutherford MJ (2002) An experimental study of the kinetics of decompression-induced crystallization in silicic melt. Journal of Geophysical Research 107:1–24.

Harris AJ., Flynn LP, Matias O, et al. (2004) The evolution of an active silicic lava flow field: an ETM+ perspective. Journal of Volcanology and Geothermal Research 135:147–168.

Harris AJL, Flynn LP, Matias O, Rose WI (2002) The thermal stealth flows of Santiaguito dome, Guatemala: Implications for the cooling and emplacement of dacitic block-lava flows. GSA Bulletin 114:533–546.

Harris AJL, Rose WI, Flynn LP (2003) Temporal trends in lava dome extrusion at Santiaguito 1922-2000. Bulletin of Volcanology 65:77–89.

Harris AJL, Vallance JW, Rose WI, et al. (2006) Downstrean aggradation owing to lava dome extrusion and rainfall runoff at Volcán Santiaguito, Guatemala. Geological Society of America Special Paper 412:86–104.

Holland ASP, Watson IM, Phillips JC, et al. (2011) Degassing processes during lava dome growth: Insights from Santiaguito lava dome, Guatemala. Journal of Volcanology and Geothermal Research 202:153–166.

INSIVUMEH (2013) Daily Volcano Bulletin Santa Maria. Instituto Nacional de Sismología, Vulcanología, Meteorología e Hidrología. Government of the Republic of Guatemala.

Jaupart C, Allègre CJ (1991) Gas content, eruption rate and instabilities of eruption regime in silicic volcanoes. Earth and Planetary Science Letters 102:413–429.

Jeffreys H (1925) The flow of water in an inclined channel of rectangular section. Philosophical Magazine Series 6 49:793–807.

Johnson JB (2004) Explosion dynamics of pyroclastic eruptions at Santiaguito Volcano. Geophysical Research Letters 31:1–5.

Johnson JB (2014) Personal Communication.

Johnson JB, Andrews BJ, Lyons JJ (2013) The surface manifestations of cyclic tilt at Volcán Santiaguito (Guatemala). IAVCEI 2013 Scientific Assembly - July 20 - 24, Kagoshima, Japan. p 492

Johnson JB, Lees JM, Gerst A, et al. (2008) Long-period earthquakes and co-eruptive dome inflation seen with particle image velocimetry. Nature 456:377–81.

Kusakabe M, Sato H, Nakada S, Kitamura T (1999) Water contents and hydrogen isotopic ratios of rocks and minerals from the 1991 eruption of Unzen volcano, Japan. Journal of Volcanology and Geothermal Research 89:231–242.

Lavallée Y, Benson PM, Heap MJ, et al. (2013) Reconstructing magma failure and the degassing network of dome-building eruptions. Geology 41:515–518.

Lavallée Y, Hess K-U, Cordonnier B, Bruce Dingwell D (2007) Non-Newtonian rheological law for highly crystalline dome lavas. Geology 35:843.

MacKay ME, Rowland SK, Mouginis-Mark PJ, Garbeil H (1998) Thick lava flows of Karisimbi Volcano, Rwanda: insights from SIR-C interferometric topography. Bulletin of Volcanology 60:239–251.

Mader HM, Llewellin EW, Mueller SP (2013) The rheology of two-phase magmas: A review and analysis. Journal of Volcanology and Geothermal Research 257:135–158.

Manley CR (1996) Physical volcanology of a voluminous rhyolite lava flow: The Badlands lava, Owyhee Plateau, Southwestern Idaho. Journal of Volcanology and Geothermal Research 71:129–153.

Mueller S, Llewellin EW, Mader HM (2009) The rheology of suspensions of solid particles. Proceedings of the Royal Society A: Mathematical, Physical and Engineering Sciences 466:1201–1228.

Nakada S, Motomura Y (1999) Petrology of the 1991-1995 eruption at Unzen: effusion pulsation and groundmass crystallization. Journal of Volcanology and Geothermal Research 89:173–196.

Nakada S, Shimizu H, Ohta K (1999) Overview of the 1990-1995 eruption at Unzen Volcano. Journal of Volcanology and Geothermal Research 89:1–22.

Navarro-Ochoa C, Gavilanes-Ruiz JC, Cortes-Cortes A (2002) Movement and emplacement of lava flows at Volcan de Colima, Mexico: November 1998 - February 1999. Journal of Volcanology and Geothermal Research 117:155–167.

Newman S, Epstein S, Stolper E (1988) Water, carbon dioxide, and hydrogen isotopes in glasses from the ca. 1340 A.D. eruption of the Mono Craters, California: Constraints on degassing phenomena and initial volatile content. Journal of Volcanology and Geothermal Research 35:75–96.

Nichols R (1939) Viscosity of lava. The Journal of Geology 47:290–302.

Pallister BJS, Thornber CR, Cashman K V, et al. (2008) Petrology of the 2004 – 2006 Mount St . Helens Lava Dome — Implications for Magmatic Plumbing and Eruption Triggering. A Volcano Rekindled: The Renewed Eruption of Mount St. Helens, 2004–2006. U.S. Geological Survey Professional Paper 1750, pp 647–702

Pallister JS, Cashman K V., Hagstrum JT, et al. (2012) Faulting within the Mount St. Helens conduit and implications for volcanic earthquakes. Geological Society of America Bulletin 125:359–376.

Papale P, Moretti R, Barbato D (2006) The compositional dependence of the saturation surface of H2O+CO2 fluids in silicate melts. Chemical Geology 229:78–95.

Rose WI (1973a) Pattern and Mechanism of Volcanic Activity at the Santiaguito Volcanic Dome, Guatemala. Bulletin of Volcanology 37:73–94.

Rose WI (1973b) Nuée ardente from Santiaguito Volcano April 1973. Bulletin Volcanologique 37:365–371.

Rose WI (1972a) Notes on the 1902 eruption of Santa María volcano, Guatemala. Bulletin Volcanologique 36:29–45.

Rose WI (1987a) Volcanic activity at Santiaguito Volcano 1976-1984. In: Fink JH (ed) The Emplacement of Silicic Domes and Lava Flows. Geological Society of America Special Paper 212. The Geolgical Society of America, pp 17–27

Rose WI (1987b) Santa María, Guatemala: bimodal soda-rich calc-alkalic stratovolcano. Journal of Volcanology and Geothermal Research 33:109–129.

Rose WI (1972b) Santiaguito Volcanic Dome, Guatemala. Geological Society of America Bulletin 83:1413–1434.

Rose WI, Grant NK, Hahn GA, et al. (1977) The Evolution of Santa María Volcano. The Journal of Geology 85:63–87.

Rose WI, Pearson T, Bonis S (1976) Nuée ardente eruption from the foot of a dacite lava flow, Santiaguito Volcano, Guatemala. Bulletin Volcanologique 40:23–38.

Rose WI, Stoiber RE, Bonis SB (1970) Volcanic activity at Santiaguito Volcano, Guatemala June 1968 – August 1969. Bulletin Volcanologique 34:295–307.

Rust AC, Cashman K V. (2011) Permeability controls on expansion and size distributions of pyroclasts. Journal of Geophysical Research.

Rust AC, Manga M, Cashman K V (2003) Determining flow type, shear rate and shear stress in magmas from bubble shapes and orientations. Journal of Volcanology and Geothermal Research 122:

Sahagian DL, Proussevitch AA (1998) 3D particle size distributions from 2D observations: stereology for natural applications. Journal of Volcanology and Geothermal Research 84:173–196.

Sahetapy-Engel ST, Harris AJL (2008) Thermal structure and heat loss at the summit crater of an active lava dome. Bulletin of Volcanology 71:15–28.

Sahetapy-Engel ST, Harris AJL, Marchetti E (2008) Thermal, seismic and infrasound observations of persistent explosive activity and conduit dynamics at Santiaguito lava dome, Guatemala. Journal of Volcanology and Geothermal Research 173:1–14.

Sahetapy-Engel STM (2004) Surface temperature and spectral measurements at Santiaguito lava dome, Guatemala. Geophysical Research Letters 31:L19610.

Sanderson RW, Johnson JB, Lees JM (2010) Ultra-long period seismic signals and cyclic deflation coincident with eruptions at Santiaguito volcano, Guatemala. Journal of Volcanology and Geothermal Research 198:35–44.

Sapper K (1926) Die Vulkanische Tatigkeit in Mittelamerika im 20 Jahrhundert. Zeitschrift fuer Vulkanologie 9:156–203.

Scaillet B, Clemente B, Evans B, Pichavant M (1998) Redox control of sulfur degassing in silicic magmas. Journal of Geophysical Research 103:937–949.

Scharff L, Ziemen F, Hort M, et al. (2012) A detailed view into the eruption clouds of Santiaguito volcano, Guatemala, using Doppler radar. Journal of Geophysical Research 117:1–21.

Schneider D, Vallance J (2008) Use of thermal infrared imaging for monitoring renewed dome growth at Mount St. Helens, 2004. A Volcano Rekindled: The Renewed Eruption of Mount St. Helens, 2004–2006. U.S. Geological Survey Professional Paper 1750, pp 347–359

Scott JAJ, Mather TA, Pyle DM, et al. (2012) The magmatic plumbing system beneath Santiaguito Volcanco, Guatemala. Journal of Volcanology and Geothermal Research 237-238:54–68.

Scott JAJ, Pyle DM, Mather TA, Rose WI (2013) Geochemistry and evolution of the Santiaguito volcanic dome complex, Guatemala. Journal of Volcanology and Geothermal Research 252:92–107.

Shea T, Houghton BF, Gurioli L, et al. (2010) Textural studies of vesicles in volcanic rocks: An integrated methodology. Journal of Volcanology and Geothermal Research 190:271–289.

Simkin T, Sibert L, Kimberly P (1994) Volcanoes of the World.University of California Press, Oakland.

Singer BS, Smith KE, Jicha BR, et al. (2011) Tracking open-system differentiation during growth of Santa Maria Volcano, Guatemala. Journal of Petrology 52:2335–2363.

Smith JV, Miyake Y, Oikawa T (2001) Interpretation of porosity in dacite lava domes as ductile–brittle failure textures. Journal of Volcanology and Geothermal Research 112:25–35.

Smithsonian Institution (1980) Santa Maria. Scientific Event Alert Network (SEAN) Bulletin

Sparks R (2003) Dynamics of magma degassing. Geological Society, London, Special Publications 213:5–22.

Spieler O, Kennedy B, Kueppers U, et al. (2004) The fragmentation threshold of pyroclastic rocks. Earth and Planetary Science Letters 226:139–148.

Stoiber RE, Rose WI (1969) Recent volcanic and fumarolic activity at Santiaguito volcano, Guatemala. Bulletin Volcanologique 33:475–502.

Stoiber RE, Rose WI (1970) The geochemistry of Central American volcanic gas condensates. Geological Society of America Bulletin 81:2891–2912.

Tuffen H, Dingwell D (2004) Fault textures in volcanic conduits: evidence for seismic trigger mechanisms during silicic eruptions. Bulletin of Volcanology 67:370–387.

Tuffen H, Dingwell D, Pinkerton H (2003) Repeated fracture and healing of silicic magma generate flow banding and earthquakes? Geology 31:1089–1092.

Watts AB, Peirce C, Grevemeyer I, et al. (2012) Rapid rates of growth and collapse of Monowai submarine volcano in the Kermadec Arc. Nature Geoscience 5:1–6.

Watts RB, Herd RA, Sparks RSJ, Young SR (2002) Growth patterns and emplacement of the andesitic lava dome at Soufriere Hills Volcano, Montserrat. Geological Society, London, Memoirs 21:115–152.

Williams H (1932) Santa Maria, Guatemala. The History and Character of Volcanic Domes. University of California Press, Berkeley, California, pp 63–66

Williams SN, Self S (1983) The October 1902 Plinian eruption of Santa Maria Volcano, Guatemala. Journal of Volcanology and Geothermal Research 16:33–56.

Wright HMN, Roberts JJ, Cashman K V. (2006) Permeability of anisotropic tube pumice: Model calculations and measurements. Geophysical Research Letters 33:L17316.

Yamamoto T, Takarada S, Suto S (1993) Pyroclastic flows from the 1991 eruption of Unzen Volcano, Japan. Bulletin of Volcanology 55:166–175.

Zhang Y, Xu Z, Zhu M, Wang H (2007) Silicate melt properties and volcanic eruptions. Reviews of Geophysics 45:RG4004.

APPENDIX A: METHODS

6.1 MAPPING AND FIELD DESCRIPTIONS

Three days were spent on the summits of Brujo, Monje and Mitad, and mapping was outlined on print outs of high-resolution aerial orthophotos taken in 2006 by the Instituto Geographico Nacional (IGN) of Guatemala. The Volcanic Geology of Santiaguito map by Escobar Wolf et al. (2010) was used as a base reference. The mapping strategy was: 1. Identify new deposit, 2. Take a photo, 3. Note GPS location, 4. Draw a field sketch of the deposit, 5. Write a general description of the deposit, with characteristics such as structure, size, crystal content, vesicularity, vesicle size and shape, and how these may or may not change over the deposit. 6. Take a strike and dip of deposit boundaries or interesting changes in vesicularity or structure, 7. Take a trend and plunge of any lineations, 8. Measure deposit and features, if applicable, 9. Take a sample, 10. Draw outline of feature on map, 11. Note down thoughts of what I think this deposit may be and how it may have been extruded.

These observations were then transferred digitally onto the aerial photo to create the finished map back at UC.

6.2 SAMPLE COLLECTION

When samples were collected, a photo was taken, and using a compass a waterline and north arrow were drawn on the sample before being placed in a labelled sample bag. The following information was recorded in my field notebook:

The photo number, GPS Waypoint co-ordinates, a strike and dip of the deposit (if applicable, i.e. of a spine rather than a blocky lava flow), a general description of the deposit, and the place in the deposit the sample was taken from (e.g. proximity to vesicular “shear zone” in a spine). A field sketch was also done if the photo wasn’t clear, or if the deposit needed explaining. If I had done a large scale sketch of the area I also labelled the location of the sample on the sketch.

These were converted to a spreadsheet once back at the University of Canterbury.

6.3 SAMPLE ENUMERATION

Rock samples were labelled according to the GPS Waypoint numbers where they were collected, and the number of samples obtained from each location. Therefore, where only one rock sample was obtained from a field location the designated sample number is the same as the field location number (e.g. one sample from WP 021 was given the number ‘SG-021’). Where there more than one rock sample was collected from the same location an individual sample letter follows the GPS Waypoint number (e.g. the two samples from Waypoint 039 were enumerated 039A and 039B). The exception to this rule is the 2011-2012 lava flow samples which were labelled according to the flow (e.g. Waypoint 072 – 2011

Lava Flow) Thin section, pycnometer, tomography and SEM samples were labelled the same number.

6.4 Sample Analysis

Sample analysis was focused on determining crystallinity (phenocryst and microlite), porosity, bubble shape and size, crystal alignment, and evidence of shear zones on the edges of spines. Mineral type and percentages were not undertaken because they are well defined in the literature.

6.5 Crystallinity and Micro-texture Analysis

6.5.1 Thin Section Preparation

Non-covered thin sections were made using standard petrographic techniques for selected samples at the University of Canterbury. The samples were soaked in UV glue prior to the final grinding down process so that bubbles were illuminated under UV light. Photos were taken of the rocks prior to cutting, and after cutting. At least 3 thin sections were made from each sample, at right angles so to accurately document the orientation of any fabrics. If any interesting textures were noted (i.e. change in grainsize or bubble textures) additional thin sections were made. Sketches of the samples were done, noting where on the sample each thin section was made from. The thin sections were then labelled with the sample number and thin section direction i.e. SG 039 – A (Santiaguito, Waypoint 039, Thin Section Orientation A), and an arrow representing either north or another appropriate reference such as extrusion direction or direction of the outer edge. These were noted on the sketch and on a spreadsheet.

6.5.2 Phenocryst Percentage Calculations

Care and accuracy was taken in the calculation the phenocyst percentages, as they have a large influence on the viscosity of the magma. They were calculated as a percentage of dense rock (bubble free), so the data is comparable between samples. Phenocryst percentages were calculated by taking pictomicrographs of the thin sections in both cross-polarised and plain polarised light at 2x magnification, to represent ~1/3 of the thin section. Through repeated phenocryst calculations of different sizes, this area was calculated to be statistically relevant of the crystallinity of the thin sections as a whole. If the contrast between the bubbles and crystals and groundmass wasn't high, two photos of the thin section at 3x magnification were taken and analysed.

The images were then processed in Image J photo processing software, by thresholding out features of interest, using colour and brightness, and overlaying the CPL/PPL images. These images were then imported into Inkscape vector drawing software and the images were sectioned and coloured in appropriately. If necessary the bubbles or crystals were drawn in

manually. An individual layer for phenocrysts, groundmass and bubbles were made. The complete layers were then imported back into ImageJ, where they were analysed for the area fraction occupied by phenocrysts and bubbles (Figure).

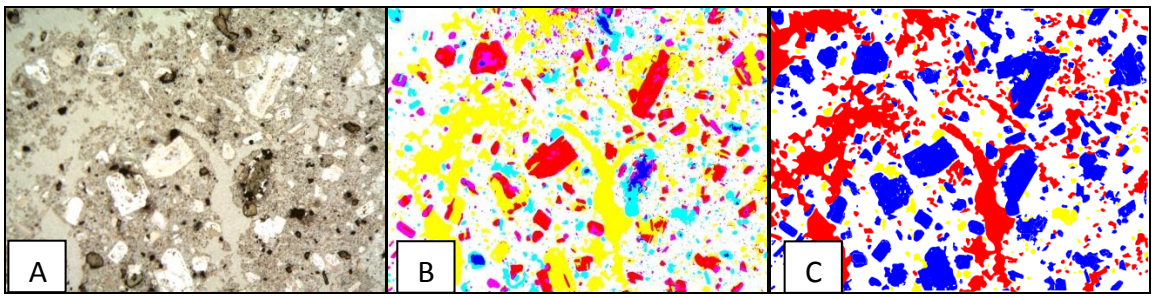

Figure A1. Illustration of phenocryst fraction calculation method. (a) Raw pictomicrograph. (b) Composite image after initial processing in ImageJ. (c) Completed image to calculate phenocryst percentages from. Red = Bubbles, Yellow = opaques, White = groundmass, Blue = Plagioclase, Pyroxene and Amphibole phenocrysts.

6.5.3 Microlite Percentage Calculations

Microlite percentages and size were measured using photos of the rocks acquired on the SEM. The SEM was used because it was extremely difficult to measure an accurate percentage using pictomicrographs on the optical microscope. 6-8 photos were taken of the groundmass per sample. These images were taken randomly along a transect (where the groundmass could be found) at X1200 - X1500 magnification. The samples selected were used because they are the most glassy and unaltered. Sample preparation and SEM settings are stated below.

The photos were imported into ImageJ where the contrast was increased, and the outlines were traced manually in Inkscape (Figure). The percentage of microlites was calculated from the processed images in ImageJ. An average of the 6-8 samples was calculated and used as the final result.

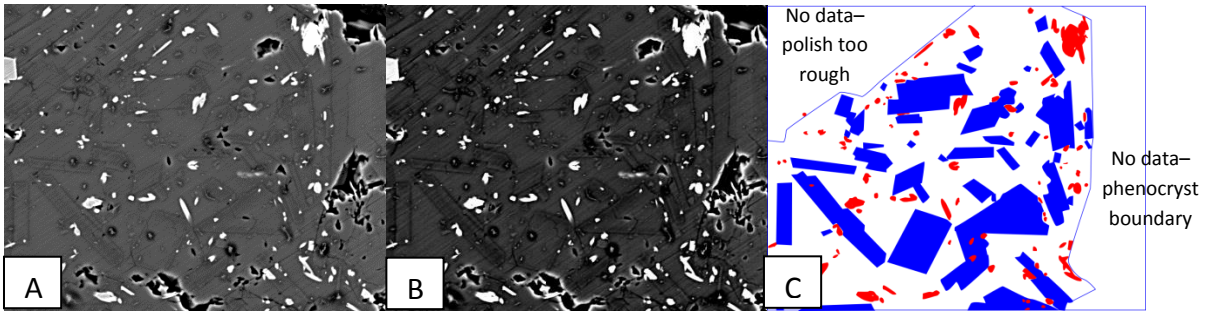

Figure A2: Example of a processed SEM image. (A) Raw Image. (B) Image after the contrast was enhanced in Image J. The white blobs are atomically heavy pyroxenes and iron oxides which cannot be differentiated under the SEM. The tabular minerals which are visible by their darkened edges are plagioclase feldspars. The dark blobs with white halos are either atomically light post-emplacement alteration or vesicles (holes in the sample) and were not counted as part of the calculation. If the edge of a phenocryst was in the sample, or a section of the sample was obscured for some reason, that area was also not calculated. (C) Sample after microlites were traced in Inkscape. Blue = plagioclase feldspar, and red = iron oxides and pyroxenes. In this example two areas were excluded - there was a phenocryst on the right side of the photo and the top left corner was difficult to trace because the polish was rough in that corner.

6.5.4 Scanning Electron Microscope (SEM)

Sample preparation:

1. Cut samples into 3-4mm slices
2. Slices were then cut down to fit a 2.5cm brass stub
3. One side of the slice was ground on a carborundum lap and polished with a standard diamond polish.
4. The sample was then suspended in ethanol (to dissolve the diamond paste) while ultrasoniced for 20 seconds to remove fibres that collected in the cracks and vesicles during polishing. The sample was then oven dried at 60 degrees for 1-2 hours and then cooled to room temperature.
5. The sample was then stuck to a stub with 5 minute araldite so that the araldite just squished out from the edges when pressure was applied. The glue was cured by drying in the oven for 1 - 2 hours at 60 degrees.
6. A carbon dag (100% fine carbon suspended in water) was applied over the non-conductive glue, around the perimeter of the sample. Sample dried at 60 degrees for 1 - 2 hours.
7. The final step was to carbon coat the sample using an Emitech 975S coater. This was done twice on two angles. One at + 30°, one at -30° to make sure that the vesicles and cracks were coated.

Table A1: Settings used on the SEM

Sample	Voltage	Current	Probe Size	Probe Current
2011 BLF	12 KV	95 µA	Medium	12
2012 BLF	15 KV	95 µA	Medium	12
021 VLF	15KV	98 µA	Medium	12
054 Spine	15KV	97 µA	Medium	12
137 Spine	15KV	101 µA	Medium	12
149 VLF	15KV	101 µA	Medium	12

6.6 VESICULARITY

Vesicle content was determined using pycnometry, tomography and thin sections. The pycnometry values were the final values used in this research as they were deemed to be the most accurate. This is because: (1) Tomography values were lower by up to 10% than pycnometry values - the tomography measurements are lower resolution and more susceptible to noise. (2) The sample size chosen for pycnometry was also larger – 2.5cm diameter x 1-4cm depth cores compared with 1cm cubes used for tomography. (3) The pyncometry value is a 3D value compared with a 2D slice represented in a thin section, which is susceptible to "the cut effect" whereby vesicles are either under-represented or over represented depending on bubble elongation direction and the plane where the thin section is cut (Sahagian and Proussevitch 1998).

6.6.1 PYCNOMETRY

Pycnometry was undertaken at Massey University using a Helium Ultrapycnometer 1000. The pycnometer sample cells into which prepared whole rock samples were placed for analysis were cylindrical, and ideally prepared rock samples should also be cylindrical and closely match sample cell dimensions to maximise analytical accuracy. However, the necessary resources required to cut cylindrical samples at diameters matching pycnometer sample sizes are not currently available at the University of Canterbury. Instead the closest size available was used (diameter = 2.5cm). The length of the sample was usually determined by either the bulk sample size or where the sample broke during the coring process, but where possible the maximum length was used (up to 4cm), to increase the accuracy. The sample blocks were dried overnight at 80degrees, and the dimensions measured using callipers - three length measurements and three of the width were measured to the nearest 0.5mm and averaged to calculate the sample block volume. Each sample block was weighed

to the nearest 0.01mm, to enable calculation of bulk density ($\rho_{geometric}$) of the whole sample block.

Skeletal density ($\rho_{skeletal}$), i.e. $\rho_{geometric}$ excluding connected pores, but including isolated pores, was determined from the pycnometer. The pycnometer was calibrated according the manufacturer's instructions, an error margin set at 0.005% and the weight of each sample block entered prior to analysis. The pycnometer ran 5 runs on each sample block to determine to volume of gas displaced by the sample block, and the end value used was an average of the 5 runs.

I did not measure the dense-rock equivalent density (ρ_{DRE}) necessary for porosity calculations. Instead ρ_{DRE} values were taken from Avard and Whittington (2012). Because their values were acquired from a range of extrusion products over time, their ρ_{DRE} values were considered representative of the rock suite. I used their spine sample Rbc value as a proxy for all the summit dome rock samples, and the most recent value of 2630kg m^{-3} from Lava flow Rcm5 was used for as the DRE-density for the 2011-2012 lava flows (Table A). The specifics of the ρ_{DRE} collection are: ρ_{DRE} was determined using a pycnometer at Washington University (St. Louis, MO, USA) on crushed rock powders. DRE density was calculated as the average of five measurements on more than 0.1kg of rock powder, with a precision of ±4 kg m^{-3} (Table A).

Connected, isolated and total porosity was then calculated by:

1. The connected porosity ($\Phi_{connected}$) was calculated by:

$$\Phi_{connected} = 1 - \frac{\rho_{geometric}}{\rho_{skeletal}}$$

2. The volume of isolated pores was then calculated by:

$$vol\ of\ isolated\ pores = \rho_{skeletal} - \frac{Weight\ of\ core}{\rho_{DRE}}$$

3. The isolated porosity ($\Phi_{isolated}$) is calculated by:

$$\Phi_{isolated} = \frac{Volume\ of\ isolated\ pores}{Volume\ of\ core} \times 100$$

4. The total porosity (Φ_{total}) is then:

$$\Phi_{total} = \Phi_{isolated} + \Phi_{connected}$$

	Sample collected from	DRE Density kg m^{-3} (± 4)
Rcm1 - 2001-2002 Lava Flow >2.5km	Flow toe	2627
Rcm5 – 2004 Lava Flow >2.5km	Active flow front	2630
Rbc-2 - 1966? Spine Sample	Body of spine	2616

Table A2: Rock unit, age, facies type, and DRE-Density measurements from Avard and Whittington (2012) used in this study.

6.7 COMPOSITION

The composition of the rocks were not analysed in this study because there was a sufficient range of compositional data – both of bulk rock and matrix composition previously published.

6.7.1 BULK ROCK DATA

To create compositional figure, the bulk rock geochemistry was taken from Rose (1972); Avard and Whittington (2012) and Scott et al. (2013). The facies that the geochemistry came from were analysed by GPS locations (provided by Avard and Whittington (2012) and Scott et al. (2012)), or where there was no GPS location but the unit that it was taken from was described or labelled was used. Only the geochemistry of extrusive units such as lava flows or spines were used – results from explosive bombs or pyroclastic flows were excluded.

The create the date timeline the samples were plotted for year extruded vs SiO_2. If the unit was extruded between a series of years, i.e. 1999-2001, then the middle year was used as an average. The results are shown below. It showed that between 1922 – 1945 the wt% SiO_2 ranged drastically, but after 1945 the SiO2 slowly declined. The year was then entered into the equation and the year was used in the composition figure. I recognise that there is considerable variation and therefore the date vs SiO_2 should be used with caution.

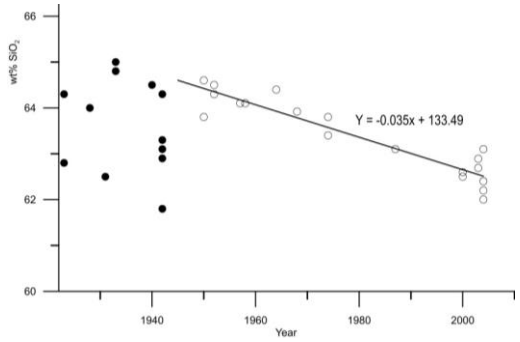

Figure A3. Year lava extruded vs wt % SiO_2.

6.8 PORE SHAPE

6.8.1 TOMOGRAPHY IMAGE ACQUISITION

X-ray micro-computed tomography was undertaken at the Australian Synchrotron during two separate sessions on the Imaging and Medical Beamline (IMBL). Each sample was placed on a stage which rotated 180° with images taken at 0.1° intervals. Samples 054 and 021 were placed on the stage alone, but 072 and 034 were stacked in a plastic tube and separated by foam. Multiple scans were made by raising the stage. A small overlap of the scans was carried out in order to stitch multiple scans from a single sample together. The specifications of each scan are shown in the table below:

Sample	**Energy**	**Window**	**Pixel Size**	**Scans**	**2D images reconstructed**
Spine (054)	45keV	~15.9mm high, ~35.1mm wide	13.73 µm	1	1158
Blocky lava flow (072) and Spine Shear Zone (034)	30keV	~13.2mm high, ~15.6mm wide	6.10 µm	2-3	2158

Conversion to a stack of greyscale images was performed remotely using X-TRACT reconstruction software.

6.8.2 TOMOGRAPHIC 3D IMAGE RECONSTRUCTION AND ANALYSIS

Image reconstruction and analysis was undertaken in ImageJ. The greyscale stacks were loaded into ImageJ and a rectangular prism was cropped from each. This measured up to 1000px by 1000px (square in 2D slices) by 2158px (i.e. number of slices, depending on the sample) so that the reconstruction was constrained within the sample.

To convert the greyscale images into a binary format for 3D reconstruction:

- Images were converted to 8bit.
- If necessary, BleachCorrector plugin was used to match histograms between slices to correct anomalously bright slices in the stacks. This was performed on sample 021 but was not necessary on the other samples.
- Noise was reduced with the ImageJ noise diffusion filter.
- Brightness/contrast functions were used to better distinguish bubbles from the crystals/glass.
- Pores were thresholded and the entire stack was converted to binary

For the images of coloured isolated pores combined with the grey connected pore network:

- Volumes were determined for all pores within the stack using the Particle Analyser plugin. The stack was then analysed twice more. The first time with the volume limit set to just below the maximum pore size to produce a new stack with just the largest pore/connected pore network. The second time the stack was analysed with the minimum pore volume at 10 000 px^3 and excluded those with contact with the side of the stack. This produced another new stack of the largest isolated pores.
- These new stacks were combined within ImageJ using the Merge Channel function. The largest pore was assigned the colour grey (as it is the colour which showed the most features of the pores when reconstructed), and the other isolated pores were assigned the colour red. Both stacks were then recreated together in 3D with 3D Viewer. The rainbow nature of the pores is a function of the isolated particle analysis. It was left this way as it makes the different isolated pores easier to distinguish (figure 15a displays this).

For the individual pore images:

When the different pore types were identified, a characteristic pore was selected and individually reconstructed. To do this the 2D images were cropped to encompass these pores, or sections of them if when they were not isolated. The new cropped stack was recreated in 3D and all other bubbles were then manually cropped out in the 3D viewer. In figure 9b, two individual pores were reconstructed from a combined image stack produced in the above method.

APPENDIX B

Way Point	Latitude	Longitude	Way Point	Latitude	Longitude	Way Point	Latitude	Longitude
15	14.74204	-91.5812	51	14.7432	-91.5697	132	14.7435	-91.5751
16	14.74218	-91.5813	52	14.7432	-91.5697	133	14.74332	-91.5755
17	14.74213	-91.5822	53	14.74317	-91.5694	134	14.74332	-91.5755
18	14.74225	-91.5807	54	14.74315	-91.5697	135	14.74358	-91.5757
19	14.74225	-91.5807	55	14.74372	-91.5711	136	14.74358	-91.5757
20	14.74135	-91.5806	56	14.74374	-91.5707	137	14.74375	-91.5756
21	14.74224	-91.5811	57	14.74429	-91.57	138	14.74235	-91.5805
22	14.74283	-91.5818	58	14.74429	-91.57	139	14.74239	-91.5804
23	14.74291	-91.5819	59	14.74428	-91.5698	140	14.74277	-91.5829
24	14.743	-91.5819	60	14.74428	-91.5698	141	14.74285	-91.5828
25	14.74337	-91.5828	61	14.74507	-91.5696	142	14.74331	-91.5828
26	14.7432	-91.5823	62	14.74525	-91.5697	143	14.74331	-91.5828
27	14.74374	-91.5778	63	14.74532	-91.5694	144	14.74356	-91.5831
28	14.74362	-91.5776	64	14.74532	-91.5694	145	14.74331	-91.5825
29	14.74359	-91.5776	65	14.74532	-91.5694	146	14.74341	-91.5825
30	14.74361	-91.5776	66	14.74532	-91.5694	147	14.74341	-91.5825
31	14.74362	-91.5777	67	14.74532	-91.5694	148	14.74336	-91.5825
32	14.74375	-91.5777	68	14.74523	-91.5695	149	14.74263	-91.581
33	14.74393	-91.5776	69	14.74523	-91.5695	150	14.74272	-91.5769
34	14.74393	-91.5772	70	14.74523	-91.5695	151	14.74265	-91.5764
35	14.74322	-91.577	71	14.74523	-91.5695	152	14.74231	-91.5757
36	14.74352	-91.577	072	14.72539	-91.5696	153	14.74265	-91.5759
37	14.74309	-91.5613	118	14.74326	-91.5734	154	14.74237	-91.5757
38	14.74167	-91.5644	119	14.7428	-91.573	155	14.74261	-91.5752
39	14.74329	-91.5698	120	14.74303	-91.573	156	14.74276	-91.5744
40	14.74316	-91.5698	121	14.74349	-91.5729	157	14.74215	-91.5743
41	14.74351	-91.5701	122	14.7435	-91.5729	158	14.74358	-91.5758
42	14.74424	-91.569	123	14.74438	-91.5729	159	14.74333	-91.5757
43	14.74452	-91.569	124	14.74451	-91.5727	160	14.74336	-91.5759
44	14.74314	-91.5697	125	14.74466	-91.5726	161	14.74336	-91.5759
45	14.74313	-91.5697	126	14.74456	-91.5723	162	14.74332	-91.5758
46	14.74318	-91.5697	127	14.74382	-91.5745	163	14.742	-91.5802
47	14.74316	-91.5697	128	14.74389	-91.5745	164	14.74216	-91.5806
48	14.74319	-91.5698	129	14.74389	-91.5745	165	14.74193	-91.5805
49	14.7432	-91.5697	130	14.7433	-91.5747	166	14.74163	-91.5806
50	14.7432	-91.5697	131	14.74317	-91.5746	167	14.74151	-91.5806

Appendix B1: Table of waypoint numbers and GPS co-ordinates. Sample numbers mentioned in the study are labelled after the waypoint they are taken from.

Waypoint	Dome	Facies (Label)	Facies (Type)	S/D of surface	Analyses	If Spine - Has Shear Zone?	Has Spine interior?	If Lava Flow - Top or centre of flow
21	Brujo	Rbe	VLF		TS, P, T, SEM	-	-	Top
024A	Brujo	Rbh-1	Spine		TS, P	Yes	No	-
023A	Brujo	Rbh-1	Spine		TS, P, T	Yes	No	-
023B	Brujo	Rbh-1	Spine		TS, P	Yes	No	-
023C	Brujo	Rbh-1	Spine	114/50SSW	TS	No	Yes	-
22B	Brujo	Rbh-1	Spine		P	Yes	No	-
22	Brujo	Rbh-1	Spine		TS	Yes	No	-
29B	Monje	Rmb-1	Spine	T/P 159/38	TS	Maybe	Maybe	-
30	Monje	Rmb-1	Spine	100/35S	TS	Yes	No	-
030B	Monje	Rmb-1	Spine		TS, P	Yes	Yes	-
31	Monje	Rmb-1	Spine	090/23S	TS, P	Yes	Yes	-
32	Monje	Rmb-1	Spine	102/32		Yes	No	-
34	Monje	Rmb-2	Spine	118/80S	P	Yes	Yes	-
039A	Mitad	Re-1	Spine	049/75SE	TS	No	Yes	-
039B	Mitad	Re-1	Spine	049/75SE	TS, P	No	Yes	-
43A	Mitad	Re-4	BLFSummit		TS, P	-	-	Top
43B	Mitad	Re-4	BLFSummit		TS	-	-	Top
044B	Mitad	Re-1	Spine		TS, P	Yes	Yes	-
48	Mitad	Re-1	Spine	256/88S	TS, P	Yes	No	-
54	Mitad	Re-1	Spine		TS, P, T, SEM	No	Yes	-
2011 Flow	Caliente	Rcp-1	BLF>2.5km	Low dip <10° but may reach ~30° on flanks of the cone	TS, P, SEM	-	-	Top
2011 or 2012 Lava Flow	Caliente	Rcp-1or2	BLF>2.5km		TS, P, T	-	-	Top
2012 Flow	Caliente	Rcp2	BLF>2.5km	Steep flow front looked >70°	TS, P, SEM	-	-	Top
120	Monje	Rma	Spine	280/80W	TS	Yes	No	-
137	Monje	Rmb-3	Spine	052/85S	TS, P, SEM	No	Yes	-
139	Brujo	Rbb-3	Spine	260/80SE	TS, P	Yes	Yes	-
144	Brujo	Rbf-7	Spine	156/85S		Yes	No	-
143	Brujo	Rbh-1	Spine	147/83S	TS	Yes	No	-
140	Brujo	Rbh-2	Spine	062/76S	TS, P	No	-	-
141A	Brujo	Rbh-2	Spine	240/81N	TS, P	Yes	No	-
141B	Brujo	Rbh-2	Spine	flow bands: 027/38ESE	TS, P	Yes	Possibly	-
149	Brujo	Rbe	VLF		TS, P, T, SEM	-	-	Centre
157	Mitad	Rea	BLF<2.5km		TS, P	-	-	Centre
165	Brujo	Rbb-2	Spine	360/56E	TS, P	Maybe	Yes	-
166	Brujo	Rbb-2	Spine	356/69E	TS, P	Yes	Yes	-
168	Brujo	Rbb-2	Spine		TS, P, T	Yes	Yes	-

TS =standard petrographic thin section (with UV glue), P= porosity measurements (ultra-pyconometer 100 at Massey University), and T = tomography (Australian Synchrotron), SEM = scanning electron microscope.
VLF = Vesicular Lava Flow, BLF = Blocky Lava Flow.

Appendix B2: Samples used in this study and analyses undertaken on the samples

Vent	Unit	Facies	Age: Start*	Age: Average	wt%SiO_2	Na_2O	K_2O	$Na_2O + K_2O$	Sample No.	Reference
Caliente	Rcm1	BLF>2.5km	Dec-01 - 2004	2004	62.0	4.61	1.6	6.21	SG-09-01	(Scott et al., 2013)
Caliente	Rcm1	BLF>2.5km	Dec-01 - 2004	2004	62.4	4.69	1.59	6.28	SG-09-03	(Scott et al., 2013)
Caliente	Rcl	BLF>2.5km	Jul-99 – Dec 01	2000	62.6	4.7	1.61	6.31	SG-09-04	(Scott et al., 2013)
Caliente	Rcm1	BLF>2.5km	Dec-01 - 2004	2003	62.89	4.78	1.57	6.35	SA-05-19	(Avard & Whittington, 2012)
Caliente	Rcm1	BLF>2.5km	Dec-01 - 2004	2004	63.1	4.69	1.62	6.31	SG-09-02	(Scott et al., 2013)
Caliente	Rch	BLF>2.5km	Jun-86 - 1989	1987	63.1	4.97	1.67	6.64	SG-09-06	(Scott et al., 2013)
Caliente	Rcm3	BLF<2.5km	Dec-01 - 2004	2004	62.4	4.62	1.62	6.24	SG-09-07	(Scott et al., 2013)
Caliente	Rcm3	BLF<2.5km	Dec-01 - 2004	2004	62.2	4.64	1.58	6.22	SG-09-08	(Scott et al., 2013)
Caliente	Rcl	BLF<2.5km	Jul-99 – Dec 01	2000	62.5	4.68	1.59	6.27	SG-09-05	(Scott et al., 2013)
Brujo	Rba	BLF<2.5km	1958	1958	64.1	5.1	1.59	6.69	800	(Rose, 1972)
Brujo	Rbc-1	BLF<2.5km	1963 - 1966	1954	64.4	5.1	1.64	6.74	550	(Rose, 1972)
Mitad	Rea	BLF<2.5km	1935	1935	61.8	4.8	1.48	6.28	1023	(Rose, 1972)
Mitad	Rea	BLF<2.5km	1935	1935	62.9	4.74	1.64	6.38	SG-09-36	(Scott et al., 2013)
Mitad	Rea	BLF<2.5km	1935	1935	63.1	4.68	1.6	6.28	SG-09-35	(Scott et al., 2013)
Mitad	Rea	BLF<2.5km	1935	1935	63.3	4.79	1.63	6.42	SG-09-38	(Scott et al., 2013)
Mitad	Rea	BLF<2.5km	1935	1935	64.3	4.84	1.66	6.5	SG-09-37	(Scott et al., 2013)
Caliente	Rca	BLF<2.5km	1932 – Dec 34	1933	64.8	5.1	1.66	6.76	1004	(Rose, 1972)
Caliente	Rcb	BLF<2.5km	1932 – Dec 34	1933	65.0	5	1.7	6.7	1104	(Rose, 1972)
Caliente	Rcm5	BLFSummit	Dec-01 - 2004	2003	62.69	4.64	1.53	6.17	SA-05-14	(Avard & Whittington, 2012)
Caliente	Rcc	BLFSummit	Nov-29-Dec 34	1931	62.5	4.7	1.58	6.28	1103	(Rose, 1972)
Caliente	Rc	BLFSummit	Jun-22 – Feb 25	1923	62.8	4.9	1.58	6.48	1105	(Rose, 1972)
Caliente	Rc	BLFSummit	Jul-22 – Mar 25	1923	64.3	4.9	1.7	6.6	1125	(Rose, 1972)
Caliente	Rcd	BLFSummit	Jan-27 – May 29	1928	64.0	5	1.63	6.63	1003	(Rose, 1972)
Monje	Rma	Spine	1952	1952	64.3	5	1.64	6.64	802	(Rose, 1972)
Monje	Rma	Spine	1952	1952	64.5	4.87	1.68	6.55	SG-09-33	(Scott et al., 2013)
Brujo	Rbc-2	Spine	1963 - 1966	1964	69.1	4.38	1.38	5.76	SA-06-14	(Avard & Whittington, 2012)
Monje	Rmb-4	Spine	1956 - 1958	1957	64.1	4.86	1.68	6.54	SG-09-32	(Scott et al., 2013)
Monje	Rm-2	Spine	1947 - 1952	1950	64.6	4.9	1.71	6.61	SG-09-34	(Scott et al., 2013)
Brujo	Rbc	Spine	Jan-73 – Apr 75	1974	63.4	4.97	1.67	6.64	SG-09-30	(Scott et al., 2013)
Brujo	Rbc	Spine	Jan-73 – Apr 75	1974	63.8	4.83	1.67	6.5	SG-09-29	(Scott et al., 2013)
Monje	Rm - ?	Spine	1947 - 1952	1950	63.8	4.8	1.53	6.33	1005	(Rose, 1972)
Brujo	Rb	Spine	1967 - 1970	1968	63.92	4.99	1.68	6.67	1101	(Rose, 1972)
Mitad	Re-?	Spine	1939 - 1944	1941	64.5	5.2	1.67	6.87	2003	(Rose, 1972)

Methods: Avard & Whittington (2012): Bulk rock chemical analyses were performed by fusion with lithium metaborate/tetraborate followed by inductively coupled plasma mass spectrometry, by Activation Laboratories Inc.
Scott et al. (2013): XRF and ICP-MS analysis
Rose (1972): method not included in paper
Key: VLF = Vesicular Lava Flow, BLF = Blocky Lava Flow.

Appendix B3: Bulk rock geochemistry data used in this study and the source of information.

				Groundmass (%)				
Vent	**Unit**	**Facies**	**Sample No**	**Glass**	**Plagioclase**	**Mafics**	**Total microlites**	**Reference**
Mitad	Re	Spine	2001-69	77.1	20	3	23	(Scott et al. 2012)
Mitad	Re	Spine	2002-69	75.1	21.7	3.2	24.9	(Scott et al. 2012)
Mitad	Re	Spine	2006-69	75.1	18.1	6.8	24.9	(Scott et al. 2012)
Monje	Rm	Spine	SG-09-34	78.7	17.9	3.5	21.4	(Scott et al. 2012)
Monje	Rmb	Spine	SG-09-32	73.2	21.5	5.3	26.8	(Scott et al. 2012)
Brujo	Rbc	Spine	SG-09-30	76.2	21	2.8	23.8	(Scott et al. 2012)
Brujo	Rbc	Spine	SG-09-29	78.5	20.1	1.4	21.5	(Scott et al. 2012)
Monje	Rma	Spine	802-66	75.3	20.9	3.8	24.7	(Scott et al. 2012)
Monje	Rma	Spine	SG-09-33	81	16.5	2.6	19.1	(Scott et al. 2012)
Caliente	Rca	BLFSummit	?	76.8	20.4	2.9	23.3	(Scott et al. 2012)
Mitad	Rea	BLF<2.5km	SG-09-37	77.8	20.4	1.8	22.2	(Scott et al. 2012)
Mitad	Rea	BLF<2.5km	SG-09-38	77.3	18.3	4.4	22.7	(Scott et al. 2012)
Mitad	Rea	BLF<2.5km	SG-09-35	73.1	21.5	5.4	26.9	(Scott et al. 2012)
Mitad	Rea	BLF<2.5km	SG-09-36	75	21.8	3.2	25	(Scott et al. 2012)
Caliente	Rcl	BLF<2.5km	SG-09-05	81.8	14	4.3	18.3	(Scott et al. 2012)
Brujo	Rbc	BLF<2.5km	550-67	80.6	17.2	2.2	19.4	(Scott et al. 2012)
Caliente	Rcm3	BLF<2.5km	SG-09-07	75.8	21	3.3	24.3	(Scott et al. 2012)
Caliente	Rcm3	BLF<2.5km	SG-09-08	74.5	22.9	2.6	25.5	(Scott et al. 2012)
Caliente	Rch	BLF>2.5km	SG-09-06	77.5	19.3	3.3	22.6	(Scott et al. 2012)
Caliente	Rcl	BLF>2.5km	SG-09-04	74.5	21.9	3.6	25.5	(Scott et al. 2012)
Caliente	Rcm1	BLF>2.5km	SG-09-01	78.8	17.7	3.5	21.2	(Scott et al. 2012)
Caliente	Rcm1	BLF>2.5km	SG-09-03	79.2	17.9	3.5	21.4	(Scott et al. 2012)

Appendix B4: Microlite percentage data from Scott et al. (2012) used in this study.

Vent	Unit	Sub unit	Facies	Sample No	Groundmass (%)			
					Glass	Plagioclase	Mafics	Total Microlites
Caliente	Rcp1	2011	BLF>2.5km	2011LF_8	58.1	35.3	6.6	41.9
Caliente	Rcp1	2011	BLF>2.5km	2011LF_7	63.7	32	4.3	36.3
Caliente	Rcp1	2011	BLF>2.5km	2011LF_10	62.1	33.5	4.4	37.9
Caliente	Rcp1	2011	BLF>2.5km	2011LF_11	62.5	32.7	4.8	37.5
Caliente	Rcp1	2011	BLF>2.5km	2011LF_5	54.1	40.1	5.8	45.9
							Average	39.9
Caliente	Rcp2	2012	BLF>2.5km	2012LF_1	47.9	47.9	4.2	52.1
Caliente	Rcp2	2012	BLF>2.5km	2012LF_4	55.8	39.1	5.1	44.2
Caliente	Rcp2	2012	BLF>2.5km	2012LF_8	60.8	34.9	4.3	39.2
Caliente	Rcp2	2012	BLF>2.5km	2012LF_2	53.2	40.1	6.7	46.8
Caliente	Rcp2	2012	BLF>2.5km	2012LF_5	54.2	37.8	8	45.8
Caliente	Rcp2	2012	BLF>2.5km	2012LF_6	57.4	38.1	4.5	42.6
Caliente	Rcp2	2012	BLF>2.5km	2012LF_3	64.7	31.6	3.7	35.3
							Average	43.7
Brujo	Rbe		VLF	21_a	62	35.3	2.7	38
Brujo	Rbe		VLF	021_d	67.0	29.9	3.1	33.0
Brujo	Rbe		VLF	21_c	63.5	33.5	2.91	36.5
Brujo	Rbe		VLF	21_e	57.1	38.6	4.3	42.9
Brujo	Rbe		VLF	21_f	66.7	29.0	4.3	33.3
							Average	36.4
Mitad	Re		Spine	054_k	55.0	40.5	4.5	45.0
Mitad	Re		Spine	054_f	56.1	38.9	5.0	43.9
Mitad	Re		Spine	054_e	54.2	40.2	5.5	45.8
Mitad	Re		Spine	054_a	54	43.7	2.3	46
							Average	45.2
Brujo	Rbe		VLF	149_b	59.4	38.1	2.5	40.6
Brujo	Rbe		VLF	149_c	62.3	32.7	5.0	37.7
Brujo	Rbe		VLF	149_d	60.5	36.2	3.3	39.5
Brujo	Rbe		VLF	149_e	60.8	34.4	4.8	39.2
Brujo	Rbe		VLF	149_f	59.2	37.3	3.5	40.8
							Average	39.6
Monje	Rmb		Spine	137d Upper limit	55.1	41.7	3.2	44.9
Monje	Rmb		Spine	137d Lower limit	60.9	35.9	3.2	39.1
Monje	Rmb		Spine	137f Upper limit	50.8	44.8	4.4	49.2
Monje	Rmb		Spine	137f Lower limit	56.4	39.3	4.4	43.6
							Average Upper limit	47.0
							Average Lower limit	41.4

Appendix B5: Raw microlite percentage data measured from SEM images. The average values for each sample were used. In sample 137, the edges of the microlites were blurred because of surrounding glass exsolution, so an upper and lower limit were calculated.

Sample	Length	Width	Volume	Bulk Density	Weight
	mm	mm	mm^3	$kg\ m^{-3}$	g
149	19.7	24	8897	2.12E-03	18.8241
157	18.7	24	8445	2.14E-03	18.0594
021	33.3	24	15080	1.66E-03	25.0005
021	13.3	24	6032	1.74E-03	10.4777
2011 LF	8.5	24	3845	2.30E-03	8.8504
2011/2012 LF	28.7	24	12968	2.17E-03	28.0888
2011/2012 LF	32.7	24	14778	1.83E-03	27.0102
2011/2012LF	20.0	24	9048	1.98E-03	17.9085
2012 LF	29.2	24	13195	1.99E-03	26.3229
2012 LF	33.5	24	15155	2.04E-03	30.921
2012 LF	19.7	24	8897	2.00E-03	17.7569
043A	32.7	24	14778	2.04E-03	30.1878
31	21.0	24	9500	2.44E-03	23.2267
030B - 1	33.0	24	14929	2.52E-03	37.6075
030B - 2	26.0	24	11762	2.73E-03	32.1047
34	32.8	24	14853	2.42E-03	35.9847
54	14.5	24	6560	2.43E-03	15.9623
137	37.3	24	16889	2.51E-03	42.3729
039B	11.3	24	5127	2.55E-03	13.0699
139	23.0	24	10405	2.43E-03	25.2475
140	20.0	24	9048	1.69E-03	15.2548
165	4.5	24	2036	1.96E-03	3.9822
166	28.7	24	12968	2.32E-03	30.0799
168	19.7	24	8897	2.12E-03	18.8585
26	7.0	24	3167	2.20E-03	6.9765
022B	36.0	24	16286	1.93E-03	31.4632
023A	27.3	24	12365	1.98E-03	24.4922
023B	20.7	24	9349	1.94E-03	18.1845
024 - 1	11.5	24	5202	2.26E-03	11.7361
024 - 2	18.7	24	8445	1.97E-03	16.6162
039A	8.0	24	3619	2.64E-03	9.5597
044bB-1	29.5	24	13345	2.30E-03	30.7542
044bB-2	31.7	24	14326	2.18E-03	31.2913
141A	12.0	24	5429	1.60E-03	8.6835
141B	25.0	24	11310	2.34E-03	26.426

Appendix B6: Measurements of cores used to calculate porosity in combination with the pycnometry data.

	Ultrapycnometer Average Results						
	Gas Volume	Skeletal Density	St.D.	Vol. of rock - isolated pores	Vol. of Isolated pores	% of isolated pores	Total porosity
	cc	g cc^{-}	%	m^3	m^3	%	%
149	2.6866	7.0065	0.0134	7.17E-06	7.00E-03	0.08	69.9
157	6.3911	2.8257	0.0216	6.87E-06	2.82E-03	0.03	24.4
021	9.3871	2.6633	0.0243	9.52E-06	2.65E-03	0.02	37.8
021	3.9284	2.6672	0.0051	3.99E-06	2.66E-03	0.04	34.9
2011 LF	3.3713	2.6252	0.014	3.37E-06	2.62E-03	0.07	12.4
2011/2012 LF	9.2834	3.0257	0.0039	1.07E-05	3.02E-03	0.02	28.4
2011/2012 LF	7.5717	3.5672	0.0149	1.03E-05	3.56E-03	0.02	48.8
2011/2012LF	2.0168	8.8795	0.011	6.82E-06	8.87E-03	0.10	77.8
2012 LF	10.0997	2.6063	0.0133	1.00E-05	2.60E-03	0.02	23.5
2012 LF	10.6525	2.9027	0.0348	1.18E-05	2.89E-03	0.02	29.7
2012 LF	6.1445	2.8899	0.0176	6.76E-06	2.88E-03	0.03	31.0
043A	10.7052	2.8199	0.0134	1.15E-05	2.81E-03	0.02	27.6
31	8.7543	2.6532	0.0085	8.84E-06	2.64E-03	0.03	7.9
030B - 1	12.0852	3.1119	0.011	1.44E-05	3.10E-03	0.02	19.1
030B - 2	9.0839	3.5342	0.0117	1.23E-05	3.52E-03	0.03	22.8
34	13.4278	2.6799	0.0169	1.38E-05	2.67E-03	0.02	9.6
54	6.047	2.6397	0.0087	6.10E-06	2.63E-03	0.04	7.9
137	15.9236	2.661	0.0181	1.62E-05	2.64E-03	0.02	5.7
039B	4.9233	2.6547	0.0061	5.00E-06	2.65E-03	0.05	4.0
139	9.5318	2.6488	0.0211	9.65E-06	2.64E-03	0.03	8.4
140	2.8985	5.263	0.0104	5.83E-06	5.26E-03	0.06	68.0
165	1.4055	2.8332	0.0245	1.52E-06	2.83E-03	0.14	31.1
166	11.2733	2.6682	0.0867	1.15E-05	2.66E-03	0.02	13.1
168	7.1066	2.6536	0.0102	7.21E-06	2.65E-03	0.03	20.2
26	0.6859	10.1706	0.0018	2.67E-06	1.02E-02	0.32	78.7
022B	12.0442	2.6123	0.0175	1.20E-05	2.60E-03	0.02	26.1
023A	4.7615	5.1438	0.0124	9.36E-06	5.13E-03	0.04	61.5
023B	6.9076	2.6325	0.0071	6.95E-06	2.63E-03	0.03	26.1
024 - 1	4.4848	2.6168	0.0064	4.49E-06	2.61E-03	0.05	13.8
024 - 2	6.3181	2.6299	0.0227	6.35E-06	2.62E-03	0.03	25.2
039A	1.0611	9.0093	0.0055	3.65E-06	9.01E-03	0.25	70.9
044bB-1	10.5994	2.9015	0.0128	1.18E-05	2.89E-03	0.02	20.6
044bB-2	8.8168	3.549	0.0034	1.20E-05	3.54E-03	0.02	38.5
141A	3.2893	2.6399	0.0091	3.32E-06	2.64E-03	0.05	39.5
141B	9.9964	2.6436	0.0163	1.01E-05	2.63E-03	0.02	11.6

Appendix B7. Ultrapycnometer 1000 values and porosity calculations. Pycnometry undertaken at Massey University.

Sample	Facies	Vent	Label	Phenocryst %	Vesicularity %	Matrix %	Crystallinity %
21	VLF	Brujo	Rbe	26.3	22.2	51.5	33.8
149	VLF	Brujo	Rbe	27	13.9	59.1	31.4
54	Spine	Mitad	Re-1	32	6	62	34.0
030B	Spine	Brujo	Rmb	24.5	10	65.5	27.2
139	Spine	Monje	Rbb	25.9	10.3	63.8	28.9
23	Spine	Brujo	Rbh	27.6	11.	61	31.2
2011LF	BLF>2.5km	Caliente	Rcp1	29	15	56	34.1
2012LF	BLF>2.5km	Caliente	Rcp2	27	23.2	49.8	35.2

Appendix B8: Phenocryst percentage calculations used in this study.

Source	Scott et al. 2012	Scott et al. 2012
Sample #	SG-09-01	1121-67
Unit	RcM1	Rb
Year extruded	2001 - 02	1958 - ??
Lava type	BLF>2.5km	Spine
wt%		
SiO_2	71.30	74.44
TiO_2	0.45	0.35
Al_2O_3	15.27	13.34
FeO	1.91	1.52
MnO	-	-
MgO	0.52	0.38
CaO	2.55	1.39
Na_2O	5.17	4.63
K_2O	2.53	3.28
P_2O_5	0.16	0.19
	Viscosity from Giordano et al. (2008)	
	log η (Pa s)	log η (Pa s)
T(°C)	DRY MELT	DRY MELT
700	12.72643	12.84266
750	11.41067	11.58805
800	10.28114	10.50227
850	9.300914	9.553379
900	8.442229	8.717032
950	7.683797	7.974324
T(°C)	1wt%water	1wt%water
700	9.040479	9.242656
750	8.195714	8.424234
800	7.449822	7.697497
850	6.786405	7.047857
900	6.192499	6.463662
950	5.657724	5.935498

Appendix B10: Melt chemistry and calculated viscosity of average samples selected for a long blocky lava flow and spines. Results used in Fig. 19.

For Appendix B11 (collated timeline of events) see electronic appendix.

APPENDIX C: ELECTRONIC APPENDIX

- Appendix B11
- Detailed facies map of Santiaguito
- (a) movie of pores in spines
- (b) movie of pores in spines (inverse of (a))
- (c) movie of a singular deflated branching pore in a spine
- (d) movie of pores in a vesicular lava flow
- (e) movie of a section of an inflated branching pore from a vesicular lava flow
- (f) movie of pores in long blocky lava flows
- (g) move of pores in vesicular shear zones on the edge of spines